



**HAL**  
open science

# Numerical methods for the resolution of the forward and the inverse problems for Electrical Impedance Tomography

Arriane Crystal Velasco

► **To cite this version:**

Arriane Crystal Velasco. Numerical methods for the resolution of the forward and the inverse problems for Electrical Impedance Tomography. General Mathematics [math.GM]. Université de Picardie Jules Verne, 2020. English. NNT : 2020AMIE0030 . tel-03626231

**HAL Id: tel-03626231**

**<https://theses.hal.science/tel-03626231>**

Submitted on 31 Mar 2022

**HAL** is a multi-disciplinary open access archive for the deposit and dissemination of scientific research documents, whether they are published or not. The documents may come from teaching and research institutions in France or abroad, or from public or private research centers.

L'archive ouverte pluridisciplinaire **HAL**, est destinée au dépôt et à la diffusion de documents scientifiques de niveau recherche, publiés ou non, émanant des établissements d'enseignement et de recherche français ou étrangers, des laboratoires publics ou privés.



# Thèse de Doctorat

*Mention Mathématiques*

présentée à l'École Doctorale en Sciences Technologie et Santé (ED 585)

de l'Université de Picardie Jules Verne

par

**Arriane Crystal Velasco**

pour obtenir le grade de Docteur de l'Université de Picardie Jules Verne

*Numerical methods for the resolution of the forward and the inverse problems for Electrical Impedance Tomography*

Soutenue le 21 octobre 2020, après avis des rapporteurs, devant le jury d'examen :

M. Olivier Goubet	PR, Université de Lille	Président
M. Yves Coudière	PR, Univ. de Bordeaux, INRIA	Rapporteur
M <sup>me</sup> Juliette Leblond	DR, INRIA Sophia-Antipolis	Rapporteure
M. Nabil Bedjaoui	MCF, UPJV, Amiens	Examineur
M <sup>me</sup> Stephanie Lohrengel	MCF HDR, URCA, Reims	Examinatrice
M. Youcef Mammeri	MCF HDR, UPJV, Amiens	Examineur
M <sup>me</sup> Brigitte Lucquin	Collaboratrice bénévole, Sorbonne U.	Invitée
M <sup>me</sup> Marion Darbas	PR, Sorbonne Paris Nord	Directrice
M. Renier Mendoza	Asst. Prof., UP Diliman	Co-directeur





*“With all its sham, drudgery and broken dreams, it is still a beautiful world. Be cheerful. Strive to be happy.”*

Max Ehrmann, *Desiderata*



# *Acknowledgements*

This was the dream of first-year-university-student Arriane. The journey was surely not easy, there were a lot of ups and downs. But I made it out alive, and I have these people, who were there to support and guide me along the way, to be grateful for.

First, I would like to express my thanks to the CHED-PhilFrance Scholarship for funding my three-year doctoral study.

I would like to express my deepest gratitude to my thesis supervisor, Prof. Marion, for her extensive knowledge and unwavering guidance during my research. I am deeply indebted to you, Prof. Marion, for pushing me to my limits, for believing in my work, for your invaluable experience, and for always caring for my well being. You have no idea how you have helped and saved me during the quarantine. The last stages of writing this thesis during this pandemic were extremely difficult to get through but I survived it because of your unrelenting support and patience. I am happy that I made the right decision in choosing you as my adviser. You are the best adviser anyone could ask for.

I would also like to extend my deepest appreciation to my thesis co-adviser and friend, Renier, for his unparalleled knowledge and support on my thesis. You were actually the reason why this opportunity of doing my PhD in France have opened up for me. You have always provided me with encouragement by believing in me and my work. Maybe it is because we were friends before we were adviser-advisee that I find it really comforting that I can easily ask you ~~stupid~~ questions about our research and confide in you about my struggles in PhD life. I also have to thank you for the extra practical tips on how to survive PhD.

I would like to extend my sincere thanks to the reviewers of this thesis, Dr. Yves Coudière and Dr. Juliette Leblond. Thank you Dr. Coudière for sharing your expertise and for the helpful remarks on my research. Thank you Dr. Leblond for taking time in reading and writing a detailed review on my thesis.

I am also grateful to Dr. Olivier Goubet and Dr. Nabil Bedjaoui for accepting the invitation to be a part of my thesis jury. My deepest appreciation to Dr. Stephanie Lohrengel and Dr. Youcef Mammeri for agreeing to be members of both my CST and thesis jury. Special thanks to Dr. Youcef for organizing the SEAMS and CIMPA school in Laos, where I met awesome French lecturers, leading me to pursue my PhD degree here in France. I would also like to express my thanks to Dr. Brigitte Lucquin, also one of the lecturers I met in Laos, for being a part of my thesis jury.

I'm extremely thankful to all the members of LAMFA, especially in Analyse Appliquée (A3) unit for the weekly sharing of knowledge in both mathematics and french language (for me at least). Many thanks to Isabelle and Christelle for being extra helpful with me in my administrative papers.

Living alone in a foreign country where you do not speak the language is extremely difficult. But my three years of stay in France have been bearable and enjoyable because of my fellow doctoral students who have become my friends and somehow a second family here. My deepest appreciation to these awesome people, Clara, Sylvain, Valerie, Ruxi, Alexandre, Guillaume, Miguel,

Clément G., Arthur, Clément L., Alice, Yohan, and Jihad. To Henry, for the constant company while working in BC 012, the only office that matters haha. To Hatice, for our never-ending talks about politics over wine in Place du Don. To Cheryl, my one and only Filipino friend in Amiens, for the chance to converse in our language in the office. You have no idea how freeing it was for me to be able to speak in Filipino here in Amiens haha. To Jérémy, for the patience in answering all my questions about FreeFem and for all the extra help I received from you in these 3 years. To Gauthier, for the constant reminder that we, the doctoral students, are allowed to unwind, destress, and rest in between our research. The memories of the parties, board game nights, and camping trips you organized will always be treasured. To Christopher, the most annoying Leo I've met, for the constant annoyance haha. To Marouan, for the small breaks during workdays where we just talk about every little thing we find annoying and funny, especially the PhD memes. To Seba, for listening to my ramblings about astrology, personality tests, meditation, and other weird stuff. To Anne-Sophie, for being a supportive, loving, and thoughtful friend. I still treasure the memories on my 28th birthday since it was the first time someone made a cake for me, (and it was a cheesecake)! To Mariem, for being that friend who I know I will always count on even though I am not that good in keeping in touch with friends. I really like the fact that you made me feel secure in our friendship even though I don't reply that much to messages. To Afaf, my first and closest friend here in Amiens. We may have struggled in understanding each other, but look! We made it past the cultural and personality differences. I really appreciate the comfort I found in talking with and confiding in you. Know that our memories, especially our travels, will always have a special place in my heart. Hugs!!!

I would also like to thank my Filipino friends here in France; Jared, Jade, and Jules. To Rheadel, for always being there whenever I want to rant about anything. To Thirdie, for always checking on me and supporting me all the way. Thank you both for our e-numan and mukbang sessions, and for our galas! To Daphne, for adopting me whenever I go to Paris to unwind. It was fascinating how we picked up our friendship after years of no communication.

I cannot begin to express my thanks to my friends back home in the Philippines; Tinnie, Ralph, Pio, Aaron, Kai, Ricky, the Clingy friends - Dee, Ate Jas, Kuya Mark, Vicki, Mayang, Lucky, Daryl, and Paolo, BABOYS - Paula, Gwen, Maj, Aiza, Faith, Annie, Rizza, Elise, and Janice, and to hiking friends - Raf, Ryzl, bibi Ryzn, and Donna. To Meryl, for listening to my never-ending rants about everything, for answering my calls at 6 in the morning, and for just being available whenever I need someone to talk to. Thank you for being my person. To Dai and Tammy, for the 4-hour calls just talking about anything and sometimes our frustrations in life. You are probably the person I am most comfortable talking with as evident in the duration of our calls. The pep talks you gave me helped me a lot to deal with my struggles and will always cherish. To Hazel, for being supportive in every decision I make. Thank you for adopting me whenever I am in the Philippines.

Last but not at all the least, I am extremely grateful to my family for their relentless support and infinite love they have given me on this journey. To all of you a big THANK YOU. To Ate Bandit, my sister from another

mother, for being supportive in everything I do and like. To my siblings, Crisel, Charmaine, and Arwein, for their messages of encouragement and love, and for always finding time to do video calls with me. To my niece, Anaya, for the smiles and laughter you bring to me during video calls or when watching your videos. To my mother, for her unwavering love and support for me since day one. She has this endless supply of tips on how to be healthy, how to manage money, and many more practical how-tos haha. You are my source of recipes whenever I have cravings of some random local dish back home. If the time comes that the whole world will turn its back on me, I can always count on your unparalleled love for me. Having that assurance, I know I can always survive whatever life throws at me. To my father, I hope I made you proud up there. You are forever missed and forever loved.

To the universe, thank you for the constant reminder that there is always hope in everything.



# Table of Contents

## Acknowledgements

Table of Contents	i
List of Figures	v
List of Tables	ix
Résumé de la thèse	1
General introduction	7
<b>1 Electrical Impedance Tomography: principles and modeling</b>	<b>11</b>
1.1 Principles of EIT and applications . . . . .	11
1.2 Some notations and assumptions . . . . .	13
1.3 The Quasi-Static Maxwell's Equations . . . . .	14
1.4 Different models for the EIT forward problem . . . . .	15
1.4.1 Continuum or no-gap model . . . . .	15
1.4.2 Gap model . . . . .	16
1.4.3 Shunt model . . . . .	17
1.4.4 Complete Electrode Model . . . . .	17
<b>2 Study of two forward problems for EIT: the continuum model and the CEM</b>	<b>19</b>
2.1 Existence and uniqueness results for forward problems . . . . .	19
2.1.1 The continuum model . . . . .	20
2.1.2 The Complete Electrode Model . . . . .	21
2.2 Discretization using Finite Element Method . . . . .	26
2.2.1 Lagrange Finite-Element Method . . . . .	27
2.2.2 Discretization of the continuum forward problem . . . . .	27
2.2.3 Discretization of the CEM forward problem . . . . .	28
2.3 Numerical validation of the CEM in the homogeneous unit disk case . . . . .	31
2.3.1 Set-up and analytical solution . . . . .	31
2.3.2 Numerical validation . . . . .	32
Case when $\mathbf{z} = \mathbf{0.001}$ . . . . .	32
Case when $\mathbf{z} = \mathbf{0.01}$ . . . . .	33
Case when $\mathbf{z} = \mathbf{0.1}$ . . . . .	34
2.4 Numerical simulations . . . . .	35
2.4.1 The continuum forward problem . . . . .	36
2.4.2 The CEM forward problem . . . . .	38

2.5	Conclusion . . . . .	44
<b>3</b>	<b>Sensitivity analysis of the electric potential in Complete Electrode Model</b>	<b>45</b>
3.1	Introduction and notations . . . . .	45
3.2	Sensitivity analysis of the electric potential with respect to the conductivity . . . . .	46
3.2.1	Discretization of the sensitivity equation with respect to the conductivity . . . . .	50
3.3	Sensitivity analysis of CEM with respect to the contact impedance	51
3.3.1	Discretization of the sensitivity equation with respect to the contact impedance . . . . .	54
3.4	Numerical sensitivity analysis . . . . .	56
3.4.1	Set-up . . . . .	56
	Two-dimensional set-up . . . . .	56
	Three-dimensional set-up . . . . .	56
3.4.2	Numerical sensitivity analysis with respect to the conductivity . . . . .	57
	Numerical results in 2D . . . . .	58
	Numerical results in 3D . . . . .	63
3.4.3	Numerical sensitivity analysis with respect to the contact impedance . . . . .	65
	Numerical results in 2D . . . . .	65
	Numerical results in 3D . . . . .	68
3.5	Conclusion and perspectives . . . . .	70
<b>4</b>	<b>Metaheuristics algorithms for solving the 2D EIT inverse problem</b>	<b>71</b>
4.1	Formulation of the inverse problem . . . . .	71
4.2	Presentation of the metaheuristic algorithms . . . . .	73
4.2.1	Introduction . . . . .	73
4.2.2	FA . . . . .	75
4.2.3	NBA . . . . .	76
4.2.4	GA-MPC . . . . .	78
4.2.5	EBOwithCMAR . . . . .	80
4.2.6	Differential Evolution variants . . . . .	81
	LSHADE-SPACMA . . . . .	83
	LSHADE-cnEpSin . . . . .	84
4.3	Numerical simulations . . . . .	84
4.3.1	Presentation of the test configurations . . . . .	85
4.3.2	Parameter setting for the heuristic methods . . . . .	86
4.3.3	Numerical comparison and discussions . . . . .	87
4.4	Conclusion and perspectives . . . . .	97
<b>5</b>	<b>Study of the Complete Electrode Model for Electroencephalography</b>	<b>99</b>
5.1	Neurological basics . . . . .	99
5.2	The mathematical modeling of EEG . . . . .	100

5.2.1	Head models . . . . .	101
5.2.2	Conductivities of head tissues . . . . .	102
5.2.3	Source models . . . . .	102
5.2.4	The Quasi-Static Maxwell's equation . . . . .	102
5.3	The Complete Electrode Model for EEG forward problem . . . .	103
5.3.1	Modeling the electrodes . . . . .	103
5.3.2	Existence and uniqueness result . . . . .	104
	Subtraction method . . . . .	105
	Variational formulation . . . . .	107
5.4	Conclusion and perspectives . . . . .	112
<b>General conclusion</b>		<b>113</b>
<b>A Metaheuristic algorithms pseudo-codes</b>		<b>115</b>
A.1	Firefly Algorithm pseudo-code. . . . .	115
A.2	Novel Bat Algorithm pseudo-code. . . . .	115
A.3	GA-MPC pseudo-code. . . . .	117
A.4	Simplified LSHADE-SPACMA pseudo-code. . . . .	118
A.5	Simplified LSHADE-cnEpSin pseudo-code. . . . .	118
A.6	Simplified EBOwithCMAR pseudo-code. . . . .	119
<b>Bibliography</b>		<b>121</b>



# List of Figures

1.1	EIT experimental set-up . . . . .	12
1.2	Application of EIT in monitoring lung function [TIL15] . . . . .	13
2.1	Unit disk. Case when $z = 0.001$ . $\sigma = 1$ . Errors $u - u_h$ in $L^2$ norm (left) and $H^1$ norm with respect to the mesh size $h$ in logarithm scale. . . . .	33
2.2	Unit disk. Case when $z = 0.01$ . $\sigma = 1$ . Errors $u - u_h$ in $L^2$ norm (left) and $H^1$ norm with respect to the mesh size $h$ in logarithm scale . . . . .	34
2.3	Unit disk. Case when $z = 0.1$ . $\sigma = 1$ . Errors $u - u_h$ in $L^2$ norm (left) and $H^1$ norm with respect to the mesh size $h$ in logarithm scale . . . . .	35
2.4	Conductivity distribution for the different configurations studied in this thesis. . . . .	37
2.5	Continuum model. Left: Injected current density $f$ for Cases 1a, 1b, 2a, and 2b. Right: Injected current density $f$ for Cases 3a and 3b. . . . .	38
2.6	Potential solutions $u_h$ of the continuum forward model for each considered domain. . . . .	39
2.7	Location of the electrodes . . . . .	40
2.8	Approximated interior potentials $u_h$ of the complete electrode forward model for each considered domain. . . . .	41
2.9	CEM: perturbed interior potential ( $u_p - u$ ) for each considered domain. . . . .	42
2.10	CEM Case 1: Location of electrodes . . . . .	42
2.11	CEM Case 2: Location of electrodes . . . . .	42
2.12	CEM: perturbed interior potential ( $u_p - u$ ) for each considered domain. . . . .	43
2.13	CEM Case 3: Location of electrodes . . . . .	43
2.14	CEM Case 4: Location of electrodes . . . . .	43
3.1	Illustration of the geometries considered: a unit disk, a head model and a thorax. . . . .	57
3.2	Left: layers of the spherical head model. Middle: front view of the 10-10 system for the electrodes positioning. Right: back view of the 10-10 system. . . . .	58

3.3	Unit disk. Sensitivity of the electric potential with respect to the conductivity (top left (I): $\mathbf{x}_0 = (0.4, 0)$ , $r = 0.1$ , top right (II): $\mathbf{x}_0 = (0.7, 0)$ , $r = 0.1$ , bottom left (III): $\mathbf{x}_0 = (0.4, 0)$ , $r = 0.3$ , bottom right (IV): two disjoint perturbations, one is centered at $\mathbf{x}_0 = (0.4, 0)$ with radius $r = 0.1$ and the other is centered at $\mathbf{x}_0 = (-0.4, -0.5)$ with radius $r = 0.2$ ).	59
3.4	Head model. Sensitivity of the electric potential with respect to the conductivity (top left (I): $\mathbf{x}_0 = (0.4, 0)$ , $r = 0.1$ , top right (II): $\mathbf{x}_0 = (0.7, 0)$ , $r = 0.1$ , bottom left (III): $\mathbf{x}_0 = (0.4, 0)$ , $r = 0.3$ , bottom right (IV): two disjoint perturbations, one is centered at $\mathbf{x}_0 = (0.4, 0)$ with radius $r = 0.1$ and the other is centered at $\mathbf{x}_0 = (-0.4, -0.5)$ with radius $r = 0.2$ ), skull: small perturbation in the skull conductivity . . . . .	61
3.5	Thorax. Sensitivity of the electric potential with respect to the conductivity (top left (I): $\mathbf{x}_0 = (2.62, 2.25)$ , $r = 0.05$ , top right (II): $\mathbf{x}_0 = (1.6, 2.25)$ , $r = 0.05$ , bottom left (III): $\mathbf{x}_0 = (2.62, 2.25)$ , $r = 0.1$ , bottom right (IV): two disjoint perturbations, $\mathbf{x}_0 = (2.62, 2.25)$ with radius $r = 0.1$ , and the other is centered at $\mathbf{x}_0 = (1.6, 2.25)$ with radius $r = 0.05$ ). . . . .	62
3.6	Unit ball. Sensitivity of the electric potential with respect to the conductivity in the direction of the indicator function of the support of an inhomogeneity. Top left: centered at $(0.45, 0, 0.45)$ with radius 0.2. Top right: centered at $(0, 0.3, 0.35)$ with radius 0.2. Bottom: centered at $(0, 0.3, 0.35)$ with radius 0.35. . . . .	63
3.7	Spherical head model. Sensitivity of the electric potential with respect to the conductivity in the direction of the indicator function of the support of an inhomogeneity in the brain. Top left: centered at $(0.45, 0, 0.45)$ with radius 0.2. Top right: centered at $(0, 0.3, 0.35)$ with radius 0.2. Bottom: centered at $(0, 0.3, 0.35)$ with radius 0.35. . . . .	64
3.8	Spherical head model. Boundary values of the sensitivity of the electric potential with respect to the conductivity in the direction of the indicator function of the support of a spherical inhomogeneity. . . . .	65
3.9	Unit disk. Sensitivity of the electric potential with respect to the contact impedance in the direction of a perturbation on the 7th electrode (leftmost), 19th electrode (middle) and on both electrodes (rightmost) . . . . .	66
3.10	Head model. Sensitivity of the electric potential with respect to the contact impedance in the direction of a perturbation on the 7th electrode (leftmost), 19th electrode (middle) and on both electrodes (rightmost) . . . . .	67
3.11	Thorax. Sensitivity of the electric potential with respect to the contact impedance in the direction of a perturbation on the 7th electrode (leftmost), 19th electrode (middle) and on both electrodes (rightmost) . . . . .	68

3.12	Unit ball. Values of the sensitivity of the electric potential with respect to the contact impedance in the direction of a perturbation on the 6th electrode (top left), on the 31st (top right) and on both electrodes (bottom). . . . .	69
4.1	Estimation of conductivity values inside the fixed geometries of heart and lungs with the proposed heuristic algorithms for Case 1. The conductivity of the lungs and the heart are respectively, $\sigma_l = 1.0 \text{ mS} \cdot \text{cm}^{-1}$ and $\sigma_h = 6.3 \text{ mS} \cdot \text{cm}^{-1}$ in the original image. The background conductivity is $\sigma_0 = 6.7 \text{ mS} \cdot \text{cm}^{-1}$ . . . . .	94
4.2	Image reconstructions for Case 2. The background conductivity is $\sigma_0 = 1.0 \text{ mS} \cdot \text{cm}^{-1}$ . The conductivity inside the ellipse of the original image is $\sigma_e = 6.7 \text{ mS} \cdot \text{cm}^{-1}$ . . . . .	95
4.3	Image reconstructions for Case 3. The background conductivity is $\sigma_0 = 1.0 \text{ mS} \cdot \text{cm}^{-1}$ . The conductivities are $\sigma_1 = 6.1 \text{ mS} \cdot \text{cm}^{-1}$ (big ellipse) and $\sigma_2 = 6.7 \text{ mS} \cdot \text{cm}^{-1}$ (small ellipse) in the original image. . . . .	96
5.1	A neuron cell (left) and the human brain (right) (source:wikimedia)	100
5.2	EEG in practice (left, source:wikimedia) and EEG epilepsy diagnosis (right, source:mayoclinic.org) . . . . .	100
5.3	Three-layer spherical model and CT scan of head.[DL18] . . . .	101



# List of Tables

2.1	Mesh description of a disk . . . . .	32
2.2	Case when $z = 0.001$ : errors on potential $u$ and $U$ . . . . .	33
2.3	Case when $z = 0.001$ : numerical validation of the FEM solver convergence . . . . .	33
2.4	Case when $z = 0.01$ : errors on potential $u$ and $U$ . . . . .	33
2.5	Case when $z = 0.01$ : numerical validation of the FEM solver convergence . . . . .	34
2.6	Case when $z = 0.1$ : errors on potential $u$ and $U$ . . . . .	34
2.7	Case when $z = 0.1$ : numerical validation of the FEM solver convergence . . . . .	34
2.8	FEM mesh structure . . . . .	36
2.9	CEM Case 1: Values of the voltages at selected electrodes . . . . .	42
2.10	CEM Case 2: Values of the voltages at selected electrodes . . . . .	42
2.11	CEM Case 3: Values of the voltages at selected electrodes . . . . .	43
2.12	CEM Case 4: Values of the voltages at selected electrodes . . . . .	43
3.1	Unit disk. Numerical sensitivity of the voltages with respect to conductivity at selected electrodes. . . . .	59
3.2	Head model. Numerical sensitivity of the voltages with respect to conductivity at selected electrodes. . . . .	60
3.3	Thorax. Numerical sensitivity of the voltages with respect to conductivity at selected electrodes. . . . .	62
3.4	Case 1: Numerical sensitivity of the voltages with respect to contact impedance at selected electrodes. . . . .	67
3.5	Case 2: Numerical sensitivity of the voltages with respect to contact impedance at selected electrodes. . . . .	67
3.6	Case 3: Numerical sensitivity of the voltages with respect to contact impedance at selected electrodes. . . . .	68
4.1	Different cases studied for the numerical tests . . . . .	85
4.2	Selected values for NBA parameters . . . . .	87
4.3	Reconstruction errors in % of the final solution generated by the proposed heuristic algorithms for all cases. . . . .	88
4.4	Comparison of accuracy, repeatability, and average cost of the solutions generated by the proposed heuristic algorithms for all cases. . . . .	89
4.5	Final solutions and reconstruction errors in % of each parameters in the final solution generated by the proposed heuristic algorithms for Case 1. . . . .	90

4.6	Final solutions generated by the proposed heuristic algorithms for Case 2.(Note that $3\pi/8 \approx 1.18$ .) . . . . .	90
4.7	Reconstruction errors in % of each parameters in the final solution generated by the proposed heuristic algorithms for Case 2. . . . .	91
4.8	Final solutions generated by the proposed heuristic algorithms for Case 3. (Note that $3\pi/8 \approx 1.18$ and $5\pi/8 \approx 1.96$ .) . . . . .	92
4.9	Reconstruction errors in % of each parameters in the final solution generated by the proposed heuristic algorithms for Case 3. . . . .	93

# Résumé de la thèse

Les propriétés diélectriques, telles que la conductivité et la permittivité électriques, déterminent le comportement des matériaux ou des tissus. La tomographie par impédance électrique (Electrical Impedance Tomography ou EIT) est une technique d'imagerie non invasive et sans rayonnement qui permet de reconstruire la cartographie de la conductivité d'une région d'observation à partir de mesures de potentiels électriques effectuées à la surface du domaine à inspecter. En pratique, pour l'acquisition des données, on dispose à la surface du domaine des électrodes uniformément réparties. Un courant de faible intensité (typiquement dans une gamme de fréquences comprises entre quelques Hz et quelques MHz) est ensuite injecté aux électrodes. Ceci génère une distribution de potentiel dans le milieu qui est fonction de la conductivité. On mesure les tensions électriques de surface aux électrodes qui n'ont pas été utilisées pour appliquer le courant. Puis on répète le processus avec une autre paire d'électrodes (adjacentes) pour appliquer le courant. Les mesures sont enfin inversées par un algorithme de reconstruction d'images. Les avantages de l'EIT sont son faible coût, son caractère non ionisant, sa simplicité d'utilisation avec un système de mesures portable et sa haute résolution temporelle (jusqu'à 50 images par seconde).

L'EIT est un domaine de recherche en plein essor, qui suscite une attention croissante au sein de la communauté scientifique, de par ses nombreuses et variées applications possibles (en particulier géophysiques, médicales et industrielles). Elle donne lieu à des recherches pluridisciplinaires. La première application de l'EIT date du début du XXème siècle en géophysique [Rey97; Yan14]. Dans ce domaine, elle est plus connue sous le nom de Tomographie de Résistivité Electrique. L'EIT est appliquée dans l'exploration pétrolière, minière (avec la détection de gisements minéraux et de fuites dans les réservoirs de stockage souterrains [Par84; RD96]), et également pour des problématiques environnementales. L'EIT est surtout une technologie d'imagerie médicale émergente. La plupart des modalités, telles que le CT-scan (Computerized Tomography) ou l'imagerie par résonance magnétique (IRM), utilisent des rayonnements ionisants qui exposent les patients à des risques [Do198]. Ceci justifie la recherche de domaines d'application dans lesquels l'EIT va contribuer à améliorer le soin et le suivi des patients. Les premiers travaux datent des années 80. Barber et Brown ont développé le premier système d'EIT médicale commercialisé, appelé le Sheffield Mark 1 [BB84]. Le système pouvait obtenir dix images par seconde, était portable et relativement peu coûteux par comparaison aux scanners et IRM [Yan14]. Depuis, l'EIT a démontré ses capacités à produire des images exploitables et utiles au diagnostic. De plus, l'EIT peut être appliquée au chevet du patient comme technique de surveillance continue. La surveillance régionale de la fonction pulmonaire est l'une des applications les

plus importantes de l'EIT [Hol93; NIM02; TIL15]. L'EIT permet une surveillance respiratoire et cardiovasculaire avancée. La détection de caillots sanguins dans les poumons est présentée dans [Hol93; HSBB87]. De plus, les propriétés diélectriques des tissus biologiques sont un bon indicateur de leurs conditions fonctionnelles et pathologiques. La première image de tissu humain par EIT est obtenue dans [HG78]. Les tumeurs se caractérisent par des propriétés diélectriques ayant un fort contraste par rapport à celles des tissus sains environnants. La détection de tumeurs du sein [CKKKMMM01; HHP08] et cérébrales [Hol92; BLBTGTSD+03] est de ce fait possible en EIT, et en particulier par l'EIT multifréquence (MF-EIT). Cependant, la résolution spatiale de l'EIT n'est pas encore comparable à celle obtenue par le scanner ou l'IRM. C'est un point à améliorer. Enfin, pour les applications industrielles, l'EIT a été largement utilisée pour la surveillance de processus chimiques. On peut citer également le domaine du contrôle non destructif. Par exemple, la corrosion [LYMJH18; KSV96] et les fissures dans les métaux [SV91] peuvent être détectées grâce à l'EIT.

Dans les systèmes d'EIT, les électrodes qui sont attachées à la surface, sont des métaux conducteurs. La qualité et la précision des mesures dépendent de nombreux facteurs tels que la taille, la géométrie et l'emplacement des électrodes, ainsi que le choix du courant injecté. Les configurations des électrodes peuvent notamment affecter les données. Les électrodes ont leur propre comportement électrique. La distribution de potentiel et de courant sur la surface de l'électrode joue un rôle important. Les impédances de contact des électrodes peuvent introduire un biais en raison des chutes de potentiel entre leurs bornes. Ces effets de "shunt" peuvent être réduits par la géométrie des électrodes ou par leur séparation. Plus la surface de contact est grande, plus l'impédance de contact diminue. Dans le domaine médical, l'application d'un gel pour électrodes à la surface de la peau permet d'abaisser et de stabiliser l'impédance de contact entre la peau et l'électrode. Il est nécessaire de bien nettoyer la peau afin de réduire sa couche superficielle qui est mauvaise conductrice. Il est essentiel de tenir compte de tous ces facteurs et phénomènes du contact électrode-peau afin de produire des données plus précises pour l'imagerie.

Mathématiquement, l'EIT est séparée en deux problèmes: le problème direct et le problème inverse. Le problème direct consiste à calculer la distribution du potentiel électrique dans le domaine inspecté et la tension électrique aux électrodes sur sa frontière connaissant la conductivité électrique du milieu et le courant injecté aux électrodes. Ce problème modélise l'acquisition des données en EIT. Il est alors important d'intégrer dans le modèle à la fois la géométrie des électrodes, leur position et leur comportement électrique, ainsi que les courants injectés. Différents modèles existent [Bor03]. Le modèle le plus simple pour l'EIT est le "continuum model" mais il ne prend pas en compte les électrodes. Le "shunt model" représente les électrodes par des points. La densité de courant est supposée constante à la surface de chaque électrode et nulle entre les électrodes. Le modèle d'électrode complet (CEM) considère la géométrie, l'emplacement des électrodes et les effets du contact électrode-peau [CING89; SCI92; PLW16; Hyv04]. C'est le modèle mathématique le plus précis, le plus proche des expérimentations et le plus utilisé aujourd'hui [SCI92; Hyv04;

VVSK99]. De nombreux travaux théoriques et numériques ont été consacrés à l'étude mathématique de ce modèle (par exemple [VVSK99; Hyv04; BKIN07; Ags15; DS16; HM17]).

Le problème inverse de l'EIT consiste à retrouver la distribution de conductivité électrique dans le domaine à partir de la mesure des tensions de surface et de la densité de courant injectée. Nous renvoyons le lecteur à l'article [Bor03] pour un résumé des résultats les plus significatifs d'existence, d'unicité et de stabilité. Le problème inverse de l'EIT est également connu sous le nom de problème de Calderón [Cal80] qui est sévèrement mal posé [Hol00]. Le premier résultat d'existence et l'unicité est obtenu par Kohn et Vogelius [KV84]. La conductivité est déterminée façon unique (identifiabilité) par la connaissance de l'opérateur Dirichlet-to-Neumann (DtN) sur toute la surface de l'objet; ce qui est en général hors d'atteinte dans les applications. L'identifiabilité de la conductivité (régularité  $L^\infty$ ) en 2D est démontrée dans [AP06]. En pratique, seules des informations partielles sur l'opérateur DtN sont disponibles. L'identifiabilité avec des mesures partielles est obtenue par exemple dans [KSU07; IUY10; HPS12].

Proposer des méthodes numériques permettant de reconstruire la conductivité à l'intérieur du domaine à partir des mesures de tension électrique aux électrodes est un réel enjeu. La méthode historique de reconstruction, proposée par Barber and Brown [BB84], exploitait un algorithme de type rétroprojection qui était inspiré de la transformée de Radon utilisée en rayon X. Quelques méthodes directes existent (par exemple [MSI02]). Ce sont les méthodes de reconstruction itératives qui font l'objet des travaux les plus nombreux. En effet, l'approche la plus classique est de formuler le problème inverse comme celui de la minimisation d'une fonctionnelle d'écart aux données, et d'appliquer un algorithme numérique de minimisation. On fait appel en particulier aux méthodes de type Newton avec des techniques de régularisation (par exemple [MY85; CING89; RPP10; ATT19]). La méthode de Newton-Raphson modifiée (mNR) a montré son efficacité [YWT87]. Différents auteurs ont développé et implémenté des méthodes de régularisation appliquées à l'algorithme mNR [YWT87; DS94; BLM02; HWWT91; LR06; RPP10].

Des études récentes ont proposé l'utilisation d'approches métaheuristiques pour résoudre le problème inverse. Les algorithmes métaheuristiques sont capables de converger vers le minimum global pour un choix approprié de paramètres. Ces méthodes sont en partie stochastiques et s'appliquent à toutes sortes de problèmes discrets. La plupart d'entre elles s'inspirent d'analogies avec la physique, la biologie ou encore l'éthologie. Ces méthodes ont l'avantage ni de dépendre de l'initialisation ni de nécessiter le calcul du gradient de la fonctionnelle de coût. Elles présentent aussi des inconvénients dont le réglage de paramètres et le temps de calcul souvent élevé. Dans cette thèse, nous proposons l'application de plusieurs algorithmes métaheuristiques. Les méthodes d'optimisation heuristiques les plus populaires telles que les algorithmes génétiques (Genetic Algorithms ou GA) [FRBSS14b; ML12; BRSRFFSS17; OBP00; RFSD14], l'évolution différentielle [RKKLKK10; LRHXWGY03; BRS-FSRPF+18], l'optimisation de l'essaim de particules [FRBSS14a] et le recuit

simulé [TMT12; MCLAT12] ont été utilisés pour résoudre le problème de reconstruction d'image en EIT. D'autres travaux ont proposé l'application d'approches en deux étapes où la méthode mNR est couplée avec un algorithme génétique [KBK06; KMKKL02] ou avec l'algorithme du recuit simulé [KBL05].

Cette thèse est une contribution à la résolution numérique du problème direct et du problème inverse en EIT. Après avoir dressé un état de l'art et le contexte de ces travaux, nous résumons à présent le contenu du manuscrit et les résultats obtenus.

Le premier chapitre introduit le principe de l'EIT et ses diverses applications, notamment médicales auxquelles nous portons un intérêt particulier. Nous précisons également des notations et hypothèses qui seront utilisées tout au long du document. Nous expliquons comment l'équation elliptique, qui modélise l'EIT, découle de l'approximation quasi-statique des équations de Maxwell. Nous terminons le chapitre par une présentation détaillée des différents modèles qui décrivent le problème direct de l'EIT: "continuum model", "gap model", "shunt model" et "Complete Electrode Model". Nous donnons les avantages du modèle d'électrodes complet (CEM) qui est le plus précis et réaliste de l'EIT puisqu'il prend en compte les électrodes, leur localisation, leur géométrie, et les effets du contact électrode-peau. Il sera le modèle de référence dans tout le document.

Dans le deuxième chapitre, nous explicitons les formulations variationnelles associées au "continuum model" et au CEM. Pour chaque modèle, nous énonçons un résultat d'existence et d'unicité de la solution et en rappelons la démonstration. Puis, nous expliquons la discrétisation du CEM par la méthode des éléments finis. Une validation numérique de la méthode avec une solution analytique dans le cas du disque unité de conductivité homogène est proposée. Enfin, des simulations numériques 2D sont présentées pour différentes configurations (disque de conductivité homogène, disque de conductivité constante par morceaux pour modéliser la coupe d'un modèle de tête, CT scan d'un thorax). Nous étudions notamment l'effet de perturbations dans la conductivité à la fois sur la distribution du potentiel électrique à l'intérieur du domaine et sur les valeurs de la tension électrique aux électrodes (c'est-à-dire sur les mesures EIT). Ces observations indiquent que les mesures contiennent des informations pertinentes sur les perturbations de la conductivité. Ces conclusions ont motivé l'analyse de sensibilité du chapitre suivant.

Le chapitre 3 est dédié à une analyse de sensibilité du CEM par rapport à une faible variation de la conductivité ou de l'impédance de contact des électrodes. Mathématiquement, la sensibilité est décrite par la dérivée directionnelle au sens de Gâteaux du potentiel électrique. Une preuve de la différentiabilité du potentiel électrique par rapport à la conductivité puis à l'impédance de contact des électrodes est donnée, et les dérivées respectives sont explicitées. C'est un nouveau résultat. A la fin du chapitre, nous présentons des simulations numériques 2D et 3D. Cette étude permet de confirmer et de compléter les liens intéressants entre perturbations, défauts du contact électrode-peau et les

mesures EIT observés dans le chapitre précédent. Ils mettent en évidence par exemple que les mesures de surface sont très sensibles à de faibles variations de la conductivité de l'os dans le cas du modèle de tête, et que les impacts de défauts d'électrodes ou du contact électrode-peau sur les mesures sont localisés. Ces résultats font l'objet d'un article en préparation: M. Darbas, J. Heleine, R. Mendoza, and A. C. Velasco, "Sensitivity analysis of the Complete Electrode Model for electrical impedance tomography".

Le chapitre 4 propose d'appliquer plusieurs algorithmes métaheuristiques pour la résolution numérique du problème inverse en EIT. Nous adoptons la démarche plus classique de la minimisation d'une fonctionnelle de type moindres carrés. Nous choisissons les algorithmes suivants: Firefly Algorithm (FA), Novel Bat Algorithm (NBA), Genetic Algorithm with New Multi-Parent Crossover (GA-MPC), Success History-based Adaptive Differential Evolution with Linear Population Size Reduction with Semi-Parameter Adaptation Hybrid avec Covariance Matrix Adaptation Evolutionary Strategy (LSHADE-SPACMA), Ensemble Sinusoidal Differential Covariance Matrix Adaptation (LSHADE-cnEpSin), et Effective Butterfly Optimizer avec Covariance Matrix Adapted Retreat Phase (EBOwithCMAR). Une présentation détaillée de chaque méthode et son pseudo-code est donnée. Des simulations numériques pour différentes configurations 2D permettent de comparer l'efficacité de ces algorithmes. Les algorithmes les plus récents (LSHADE-SPACMA, LSHADE-cnEpSin, et EBOwithCMAR) offrent les meilleurs résultats en terme de précision, de reproductibilité et de répétabilité. Dans le cas d'une géométrie connue (thorax), ils permettent de retrouver avec une excellente précision (erreur  $< 2\%$ ) les valeurs de la conductivité des poumons et du cœur. Lorsque la géométrie des inclusions et la conductivité sont inconnues, les résultats sont bons mais encore perfectibles, notamment sur la reconstruction de la conductivité. Plusieurs pistes de recherche sont envisageables (régularisation de la fonctionnelle, optimisation du choix des différents paramètres, ...). Ces simulations numériques sont nouvelles pour le problème inverse de l'EIT et concluantes. Ces travaux seront publiés en octobre 2020: A. C. Velasco, M. Darbas, R. Mendoza, M. Bacon, and J. C. de Leon, "Comparative Study of Heuristic Algorithms for Electrical Impedance Tomography", *Philippine Journal of Science* 149.3-a (October 2020 Issue).

Dans le chapitre 5, nous étudions le CEM pour modéliser le problème direct en électroencéphalographie (EEG). Les modèles actuels de l'EEG ne prennent pas en compte les électrodes. Le CEM est en cela une piste prometteuse. Une difficulté propre à l'EEG provient du terme source (de l'équation de la conductivité) qui est une somme de gradients de masses de Dirac. L'approche de soustraction est alors utilisée pour traiter la singularité du terme source. Un résultat d'existence et d'unicité est démontré. C'est un résultat nouveau en EEG. L'objectif est de poursuivre ce travail et de comparer numériquement le modèle proposé avec le modèle usuel qui ne tient pas compte des électrodes et de leurs effets.



# General introduction

Electrical properties such as the electrical conductivity and permittivity determine the behaviour of materials under the influence of external electric fields. Electrical Impedance Tomography (EIT) is a non invasive, radiation-free imaging technique which reconstructs the conductivity distribution of an observation region. In practice, currents of prescribed magnitudes (typically in a frequency range from several hundred Hz to several MHz) are injected at electrodes on the boundary of this region. The current passes through the object and the voltages needed for maintaining the currents are recorded. These measurements are the data which are needed and inverted to estimate the conductivity inside the object. This technology has the advantages of portability, low cost and high-time resolution.

With these advantages, EIT is a thriving area of research due to the variety of possible applications (e.g. geophysical, medical, and industrial). The first application of EIT can be traced back to one hundred years ago in geophysics [Yan14]. EIT can be used in fault examination [ZFHZWW09], sensing of mineral deposits and leaks in underground storage tanks [Par84; RD96], and the monitoring of flows of injected fluids into the earth [RDLOC93]. EIT is mostly an emerging medical imaging technology. Most modalities, such as Computerized Tomography (CT) scan and Magnetic Resonance Imaging (MRI) scan, make use of ionizing radiation which can present risks to patients [Dol98]. This concern led to efforts to develop radiation-free tomographic procedures. The first attempt in EIT began by extending X-ray computed tomography and was found defective due to its assumption that the electric currents flow in straight lines [BMS80; Yan14]. Barber and Brown developed the first commercially available prototype for EIT called the Sheffield Mark 1 system [BB84]. The system could obtain ten images per second and was portable and relatively inexpensive compared to CT and MRI scanners [Yan14]. Since the dielectric properties of biological tissues are a good indicator of their functional and pathological conditions, the number of applications of EIT for medical imaging are numerous. The first image of human tissue by EIT is obtained in [HG78]. The continuous observation of pulmonary functions is one of the most important application of EIT [NIM02; TIL15; Hol93]. EIT may allow advanced respiratory and cardiovascular monitoring. Detecting of blood clots in the lungs is presented in [Hol93; HSB87]. Moreover, an increased conductivity may be used to identify the presence of tumors, and especially, the detection of breast [CKKKMMM01; HHP08] and brain tumors [BLBTGTSD+03; Hol92]. Lastly, for industrial applications, EIT has been widely used for monitoring chemical processes. We can also cite non-destructive testing. For instance, air bubbles inside an object [WC99], corrosion [LYMJH18; KSV96], and cracks in metals [SV91] can be detected using EIT.

In EIT systems, electrodes are conducting metals that are attached to the boundary on which the electric current is applied and the resulting boundary potentials are recorded. The quality and the precision of the measurements depend on many factors such as the size, the geometry, and the location of the electrodes, and the injected current distribution. The configuration of the electrodes can affect the data. The voltage loss due to the effective contact impedance, which is the thin resistive layer between the electrode and object, should also be taken into account to accurately measure the boundary voltages. In medical applications, the skin surface is prepared using a liquid, to lower and stabilize the contact impedance between the skin and the electrode. Current shunting effect through the pickup electrodes is a well-known problem in EIT systems. Shunting effects can be efficiently reduced by the geometry of the electrodes, or by their separation. Also, boundary current distribution or current patterns affect the data since they are linearly related given a fixed conductivity distribution [Che90]. It is important to account all these parameters in order to produce more accurate data for the imaging.

Mathematically, EIT is divided into two parts: the forward problem and the inverse problem. The forward problem consists of finding the potential distribution on the domain under examination and on its boundary from the knowledge of the electrical conductivity distribution in the domain and the injected surface current pattern. It corresponds to the data acquisition. Thus, it is important to correctly model both the electrodes on the boundary, their effects, and also the injected currents. For instance, we refer to the review article [Bor03] and the references therein. The simplest forward model for EIT is the continuum model but it does not take into account the electrodes. The gap model accounts the correct configuration of the electrodes and approximates the current density by a nonzero constant at the surface of each electrode and zero in the gaps between the electrodes. The shunt model adapts the electrode configuration in the gap model and added their shunting effects. However, it did not take into account the effective contact impedance of the electrodes. The Complete Electrode Model (CEM) successfully considers the geometry, the location of electrodes mentioned earlier, their shunting effects, and the effective contact impedance [CING89; SCI92; PLW16; Hyv04]. Consequently, CEM is the most accurate and commonly used model for EIT [SCI92; Hyv04; VVSK99]. Many theoretical and numerical works have been devoted to the study of the CEM for EIT (see e.g [Ags15; BKIN07; DS16; Hyv04; HM17; VVSK99]).

The EIT inverse problem consists of retrieving the electrical conductivity distribution from the surface voltages and current density [Bor03]. The EIT inverse problem is also known as Calderón's problem [Cal80] which is a very ill-posed problem [Hol00]. The first result regarding existence and uniqueness of the solution is obtained by Kohn and Vogelius in [KV84]. The conductivity is identifiable if the solution of the EIT inverse problem can be uniquely determined using the entire corresponding voltage-to-current, namely the Dirichlet-to-Neumann (DtN) map. The identifiability for  $L^\infty$  conductivity in 2D from the complete information of the DtN map is proven in [AP06]. But in practical applications, only partial information of the DtN map is available. Thus, in [KSU07; IUY10; HPS12], the identifiability is proven if only partial information

of the DtN map is available. However, it is more practical in real-life applications to get information of the current-to-voltage or Neumann-to-Dirichlet map. Furthermore, for CEM boundary measurements, we define a linear relation between the injected currents and the voltages on the electrodes, i.e. the data is given by a finite-dimensional linear electrode current-to-electrode voltage operator.

Reconstruction algorithms are currently used in EIT to solve the inverse problem. The data, which are computed by solving the forward problem, are used. Due to instability of the inverse problem, different regularization techniques have been developed over the past years to weaken its ill-posedness, resulting in more accurate and stable reconstructions. The reconstruction algorithms used in EIT can be divided into two categories: linear reconstruction algorithms and iterative reconstruction algorithms. Reconstruction algorithms widely used are the backprojection, and the Newton-Raphson methods [BB84; RPP10; YWT87]. Linear reconstruction algorithms use the linearized Poisson's equation with respect to the conductivity. Barber and Brown [BB84] modified the Radon's backprojection theory and applied it to EIT. For instance, a one-step iteration of Newton-Raphson iterative reconstruction algorithm is used in the experiments in [CING89]. In [MY85], an iterative algorithm that uses the finite element method (FEM) to solve the Poisson's equation and the conductivity changes in all the elements is presented in [YWT87]. Yorkey et al. also compared several deterministic algorithms in solving the inverse EIT problem [YWT87]. They have shown that the modified Newton-Raphson (mNR) method can be an effective reconstruction algorithm. The modified Newton-Raphson method follows basically the classical non linear least square approach applied to the minimization of an error function. Many authors have developed and implemented different regularization methods applied to the mNR algorithm [YWT87; RPP10; HWWT91; BLM02; DS94].

Recent studies have proposed the use of heuristic approaches to solve the inverse problem. Heuristic algorithms are capable of converging towards the global minimum, given sufficient computation time and an appropriate choice of parameters. They are also very flexible and therefore, are less restricted to certain forms of constraints [Mar05]. Furthermore, these methods are not dependent on the initial guess and the gradient of the cost functional. In this thesis, we propose the use of several metaheuristic algorithms for the reconstruction of the conductivity distribution. Popular heuristic optimization methods like genetic algorithm (GA) [FRBSS14b; ML12; BRSRFFSS17; OBP00; RFSD14], differential evolution [RKKLKK10; LRHXWGY03; BRSFSRPF+18], particle swarm optimization [FRBSS14a], and simulated annealing (SA) [TMT12; MCLAT12] were used to solve the image reconstruction problem in EIT. Other works have proposed the application of two-step approaches where mNR is hybridized with GA [KBK06; KMKKL02] and SA algorithm [KBL05], both of which have succeeded in recovering the conductivity distribution in a body. In these works, a few mNR iterations were done initially without any mesh grouping and with homogeneous initial conductivity. Reconstructions produced by mNR were then significantly improved by SA and GA.

The manuscript is organized as follows.

The first chapter introduces the principle of EIT and its applications. We present also some of the notations and assumptions that will be used all throughout the document. The elliptic equation modeling EIT is derived using quasi-static Maxwell's equations. We end the chapter by thoroughly discussing the different models which describes the EIT forward problem. In particular, we emphasize the advantages of the Complete Electrode Model (CEM) as an accurate and realistic forward model for EIT.

In the second chapter, the existence and uniqueness results for the forward continuum and complete electrode models for EIT are given. We express their corresponding variational formulations. The discretization is performed by means of the Finite Element Method. A numerical validation in comparison with an analytic solution in the homogeneous unit disk for the CEM forward problem is addressed. Lastly, numerical simulations in 2D are presented and the effect of perturbations in conductivity on the values of both the interior potential and the boundary voltages (i.e. EIT measurements) is discussed.

In Chapter 3, an analysis tool is introduced to investigate the sensitivity of the potential solution of the CEM problem with respect to small variations in the conductivity and in the contact impedance of the electrodes. Mathematically, the sensitivity of the electric potential is described by its Gâteaux differentiability. We prove that the solution to the CEM forward problem is Gâteaux differentiable with respect to the conductivity and to the contact impedance and the respective derivatives are explicitly defined. The chapter ends with 2D and 3D numerical illustrations and some concluding remarks.

Chapter 4 deals with the formulation of the inverse conductivity problem of EIT as a minimization problem. Several metaheuristic algorithms are proposed and discussed in detail. We present a comparative analysis of six heuristic algorithms - Firefly Algorithm (FA), Novel Bat Algorithm (NBA), Genetic Algorithm with New Multi-Parent Crossover (GA-MPC), Success History-based Adaptive Differential Evolution with Linear Population Size Reduction with Semi-Parameter Adaptation Hybrid with Covariance Matrix Adaptation Evolutionary Strategy (LSHADE-SPACMA), Ensemble Sinusoidal Differential Covariance Matrix Adaptation (LSHADE-cnEpSin), and Effective Butterfly Optimizer with Covariance Matrix Adapted Retreat Phase (EBOwithCMAR) - for the EIT image reconstruction problem. Series of numerical tests in 2D were carried out to compare the performance of the selected algorithms.

In Chapter 5, we study the CEM to model the forward problem for Electroencephalography (EEG). The subtraction approach is used to deal with the singularity in the source term, and we have proved an existence and uniqueness result for the continuous problem.

This PhD thesis has been supported by the CHED-PhilFrance scholarship program.

## Chapter 1

# Electrical Impedance Tomography: principles and modeling

In this chapter, the Electrical Impedance Tomography (EIT) and some of its applications are introduced. Using the quasi-static approximation of Maxwell's equations, the partial differential equation describing the electromagnetic waves inside the object of observation is derived. Lastly, different electrode models on the boundary of the body are presented.

### 1.1 Principles of EIT and applications

The behavior of materials under the influence of external electric fields is usually determined by their electrical properties, such as the electrical conductivity  $\sigma$  and the electrical permittivity  $\epsilon$ . Conductivity measures the ease of a material in conducting electricity, while permittivity quantifies the willingness of the charges to separate under an imposed electric field within a material. In particular, muscle and blood will conduct the applied currents better than fat, bone, or lung tissue because free ion content determines tissue and fluid conductivity [Bro03]. In medical applications, knowing the said electrical properties are useful because tissues have different conductivities and permittivities. For example, the lung tissue conductivity is approximately five-fold lower as compared to the conductivity of other soft tissues in a human thorax. Electrical properties also differ between normal and malignant breast tissues [Jos98] and animal models of experimental stroke or seizure showed an increase of impedance of up to 100% and 10% [Hol00]. Electrical Impedance Tomography or EIT is an imaging technique that reconstructs the conductivity distribution in the interior of an object using electric currents. The term electrical impedance is the ratio of the voltage across the body of observation to the current through the body. Mathematically, EIT is an inverse problem that determines the conductivity inside the object of observation given simultaneous measurements of electric currents and voltages on the boundary of the object [Bor03; NIM02].

In an EIT experiment, a set of electric currents is applied to a finite number of electrodes attached on the surface of the object under test and the resulting voltage signals are measured. First, a finite number of surface electrodes are attached around the body through adhesive electrodes, an electrode belt, or a conductive electrode vest around the body. Then across two or more electrodes, a small value of mA of alternating currents at a frequency of 10–100

kHz is applied while the resulting voltage is measured on the remaining electrodes. Now due to safety regulations, the sum of the currents is restricted. But the process of injection of the current density patterns can be controlled. The usual current density pattern is when the current is injected into two adjacent electrodes. Another one is when the current is injected into two diametrically opposite electrodes. Lastly and by far, the «best» current pattern is the cosine/sine pattern [NIM02]. The procedure is then repeated for a finite number and linearly independent current patterns to generate a set of data for the conductivity image reconstruction [Bro03; Hol00; NIM02]. Figure 1.1 shows the experimental set-up of EIT.

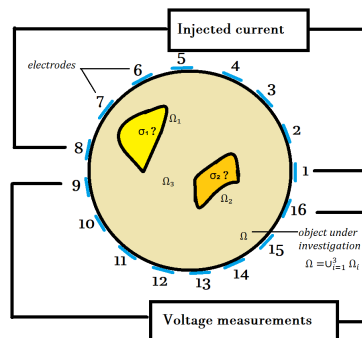


FIGURE 1.1: EIT experimental set-up

EIT is known to be non-invasive, low cost, and portable imaging modality and thus, it has gained massive attention and interest for research. Applications of EIT are usually in the field of medicine, geophysics, and nondestructive testing. Due to intense fluctuations of lung conductivity during a breathe cycle, one of the major area in medical EIT is lung imaging or the monitoring of lung function [Hol93; NIM02]. In [TIL15], EIT, as a radiation-free imaging modality, is used to monitor regional lung function continuously which allows an instant assessment of the effects of therapeutic actions on regional ventilation distribution. Figure 1.2 shows the application of EIT in clinical setting of monitoring lung function. The detection of pulmonary emboli or blood clots in the lungs is studied in [Hol93; HSBB87]. Furthermore, monitoring of lung maturity of neonates is done in [FHHWHDQH02; TWFRA19], and pulmonary edema, a condition caused by excessive fluids in the lungs, is visualized in [ABGA95]. On the other hand, the conductivity of tumour tissues differ greatly as that of the normal tissues which makes EIT a good choice in monitoring common condition for breast cancer. Breast tumour imaging is considered in [CKKKMMM01; HHP08]. Also, brain imaging and brain function monitoring for epileptic activity and stroke is investigated in [BLBTGTSD+03; Hol92].

In some fields, the mathematical model for EIT is called electrical resistivity tomography (ERT) but they both deal with the same mathematical problem. In nondestructive testing, EIT can be used to detect corrosion [LYMJH18; KSV96], air bubbles inside an object [WC99], and cracks or voids in metals [SV91; Bor03]. Lastly in geophysics, fault investigation [ZFHZWW09], the detection of underground mineral deposits [Par84] and leaks in underground storage tanks [RD96],



FIGURE 1.2: Application of EIT in monitoring lung function [TIL15]

and the observation of flows of injected fluids into the earth [RDLOC93], are some examples of EIT applications [Bor03].

The main problem in EIT is the reconstruction of the conductivity distribution, which is an inverse problem. However, solving the EIT problem is usually divided into two parts: the forward problem and the inverse problem. The forward problem is a well-posed problem in which the conductivity distribution is known and the electric potential of the body upon injecting a current density pattern is unknown. Concerning the inverse problem, the voltage on the boundary to maintain the injected current is the data that we need for the reconstruction. If all possible boundary measurements are done, the conductivity in the interior can be uniquely determined. However, we can apply only a finite number of electric signals on the boundary and so the discreteness of the electrodes and their corresponding conductivities must be taken into account. This results to different electrode models for EIT. Also, a finite number of current patterns implies that the corresponding forward problem is solved multiple times using different configurations of the current pattern to generate a good set of data for EIT.

The reconstruction problem is the inverse part of EIT and it has been mathematically formulated by Alberto Calderón [Cal80]. It is an ill-posed and non-linear problem. The ill-posedness of the problem came from the measurement process which causes some information to be lost [Hol00]. The inverse problem consists of finding an approximation of the conductivity distribution given partial and noisy current-to-voltage data.

To further explain the nature of this imaging technique, some notations and assumptions are defined, and the derivation of the forward problem of EIT is given in the next sections.

## 1.2 Some notations and assumptions

In this section, notations, definitions, and assumptions made for the variables and parameters of the problem are stated. All throughout the document, we assume the following.

Let  $\Omega \subset \mathbb{R}^d$ , for  $d = 2, 3$ , a bounded, simply connected set with smooth boundary  $\partial\Omega$ . We denote  $\mathbf{x}$  to be an arbitrary point in  $\Omega$ . The following defines the set of admissible values for the conductivity  $\sigma$ .

**Definition 1.2.1.** [KKS00] Let  $\mathcal{P}_{\text{adm}}$  be the set of admissible values of conductivity  $\sigma$ . A conductivity distribution  $\sigma : \Omega \rightarrow \mathbb{R}^+$  is in  $\mathcal{P}_{\text{adm}}$  if it satisfies the following conditions:

- i. For some  $N \geq 1$ , there exist open disjoint sets  $\Omega_j \subset \Omega$ ,  $j = 1, \dots, N$ , having piecewise smooth boundaries and

$$\bar{\Omega} = \bigcup_{j=1}^N \bar{\Omega}_j.$$

- ii. The restriction of  $\sigma$  to each subsets  $\Omega_j$  allows a continuous extension up to the boundary of the subset, *i.e.*,

$$\sigma|_{\Omega_j} \in C(\bar{\Omega}_j), \quad 1 \leq j \leq N.$$

- iii. For some constants  $\sigma_{\min}$  and  $\sigma_{\max}$ ,

$$0 < \sigma_{\min} \leq \sigma(\mathbf{x}) \leq \sigma_{\max} < +\infty, \quad \mathbf{x} \in \Omega.$$

### 1.3 The Quasi-Static Maxwell's Equations

Maxwell's equations are the fundamental laws of any electromagnetic phenomenon. Given a linear, isotropic, nondispersive body, the electric displacement  $\mathbf{D}$  and magnetic induction  $\mathbf{B}$  follows

$$\mathbf{D} = \epsilon \mathbf{E}, \tag{1.1}$$

$$\mathbf{B} = \mu \mathbf{H}, \tag{1.2}$$

where  $\epsilon$  is the electric permittivity,  $\mu$  the magnetic permeability, and  $\mathbf{E}$  and  $\mathbf{H}$  are the electric and magnetic fields, respectively. Moreover, we can assume the value of magnetic permeability in the free space, that is,  $\mu = \mu_0$ . Then Maxwell's equations read as follows:

$$\nabla \cdot (\epsilon \mathbf{E}) = \rho, \tag{1.3}$$

$$\nabla \cdot \mathbf{B} = 0, \tag{1.4}$$

$$\nabla \times \mathbf{E} = -\partial_t(\mathbf{B}), \tag{1.5}$$

$$\nabla \times \mathbf{B} = \mathbf{J} + \mu_0 \partial_t(\epsilon \mathbf{E}), \tag{1.6}$$

where  $\rho$  is the charge density and the current density  $\mathbf{J}$  relates with  $\mathbf{E}$  and conductivity distribution  $\sigma$  by Ohm's Law

$$\mathbf{J} = \sigma \mathbf{E}. \tag{1.7}$$

Since EIT systems operates at low frequencies applied to objects of small length, the time derivatives in (1.5) and (1.6) can be neglected [Bor03; NIM02]. With this, the electric field is now curl-free and derives from a scalar electric potential  $u$

$$\mathbf{E} = -\nabla u. \quad (1.8)$$

Getting the divergence of (1.6) and substituting equations (1.7) and (1.8), we get respectively

$$\nabla \cdot (\nabla \times \mathbf{B}) = \nabla \cdot \mathbf{J} = 0 \quad \text{and} \quad \nabla \cdot (\sigma \mathbf{E}) = 0 \quad (1.9)$$

Therefore, we have the following elliptic equation for the electric potential  $u$  in  $\Omega$

$$\nabla \cdot (\sigma \nabla u) = 0. \quad (1.10)$$

The question is now which boundary conditions are needed to be applied on the boundary of the body  $\Omega$  for modeling EIT.

## 1.4 Different models for the EIT forward problem

The information needed for the EIT inverse problem heavily depends on the accurate computation of the measurements done on the boundary. Thus, electrode models on the boundary that are commonly used in the literature play an important role on the accuracy of the results of EIT. In this section, the different electrode models are introduced and derived. Together with the governing equation derived earlier, boundary conditions are imposed that result to different models for EIT.

### 1.4.1 Continuum or no-gap model

As said in the previous section, EIT is governed by the elliptic equation (1.10) in the domain  $\Omega$ . Let  $\vec{n}$  be the unit normal vector on  $\partial\Omega$  oriented towards the exterior of  $\Omega$ . The normal derivative  $\partial_{\vec{n}}$  is defined as the directional derivative in the direction of the unit normal vector. Considering now the current applied to the body which is formulated as the term  $\sigma \partial_{\vec{n}} u$  [NIM02], a Neumann condition is imposed on the boundary. Take the applied current density on the boundary to be a continuous function  $f$  that satisfies the conservation of charge, that is,

$$\sigma \partial_{\vec{n}} u|_{\partial\Omega} = f \quad \text{such that} \quad \int_{\partial\Omega} f \, ds = 0.$$

The resulting model is referred as *continuum* model for EIT and is given by

$$\begin{cases} \nabla \cdot (\sigma \nabla u) = 0 & \text{in } \Omega \\ \sigma \partial_{\vec{n}} u = f & \text{on } \partial\Omega. \end{cases} \quad (1.11)$$

This model is the simplest and easiest to deal with mathematically.

We know that the voltage pattern and the current pattern is linearly related by the resistance matrix, i.e.,  $V = RI$ . In particular, if a complete set of current patterns and their corresponding characteristic resistances are known, then the prediction of the voltages that result from applying any current pattern is possible [SCI92]. Moreover, in [SCI92; CING89], an EIT system is set-up in such a way that the prediction of the outcome of every applied current pattern is reduced to the characteristic resistances. Thus in order to measure accuracy of different EIT models, a comparison is made from the computed resistances in the different EIT models and that of the experimental data. Experiments show that the continuum model overestimates the resistivity in the body by 25% [SCI92]. Note that resistivity is defined as the reciprocal of conductivity.

This leads us to question on how to choose the current density in such a way that a good approximation for the resistivity of the body is obtained. The different models for EIT are determined by assuming different functions for the applied current density.

## 1.4.2 Gap model

The gap model considers putting electrodes on the boundary where electric current is inserted and the resulting potential is measured. Define a set of patches  $e_\ell \subset \partial\Omega$ ,  $\ell = 1, \dots, L$  as the mathematical model of the contact electrodes. These electrodes are assumed to be strictly disjoint with each other, that is,

$$\bar{e}_\ell \cap \bar{e}_k = \emptyset \text{ for } \ell \neq k. \quad (1.12)$$

Let  $\Gamma_e \subset \partial\Omega$  be defined as

$$\Gamma_e = \bigcup_{\ell=1}^L e_\ell, \quad (1.13)$$

where  $e_\ell$  is the  $\ell$ th electrode on the boundary and  $L \in \mathbb{N}$  is the total number of electrodes on the boundary. Denote by  $I_\ell \in \mathbb{R}$  the current injected on the  $\ell$ th electrode. Thus, the applied current density is defined as a piecewise constant function given by

$$\begin{cases} \frac{I_\ell}{|e_\ell|} & \text{on } e_\ell, \ell = 1, 2, \dots, L, \\ 0 & \text{on } \partial\Omega \setminus \Gamma_e, \end{cases} \quad (1.14)$$

where  $|e_\ell|$  is the length or area of the electrode. Hence, the gap model is described by the following boundary value problem

$$\begin{cases} \nabla \cdot (\sigma \nabla u) = 0 & \text{in } \Omega, \\ \sigma \partial_{\bar{n}} u = \frac{I_\ell}{|e_\ell|} & \text{on } e_\ell, \ell = 1, 2, \dots, L, \\ \sigma \partial_{\bar{n}} u = 0 & \text{on } \partial\Omega \setminus \Gamma_e. \end{cases} \quad (1.15)$$

Gap model is still easy to work with mathematically but only gives slight improvement in the approximation of the voltage. It still overestimates the resistivity in the body because both the continuum model and the gap model ignore

the shorting or shunting effect of the electrodes [SCI92].

### 1.4.3 Shunt model

The ‘‘Shunt’’ model takes into account that the metal electrodes provide low-resistance path for the current. This effect is called the shorting or shunting effect of the electrodes. To address the said effect, the model assumes that the metal electrodes are perfect conductors. This results to the potential on each electrode being a constant value. However, if this condition is incorporated to the continuum model in Section 1.4.1, an over determined problem is obtained. Thus the Neumann boundary condition from the continuum model is replaced by weaker conditions.

In particular, the current density on an electrode is equal to the inserted current and there is no current on the part of boundary where there is no electrode. Mathematically, we have the Shunt model as the equation (1.10) with the following boundary conditions:

$$\left\{ \begin{array}{ll} \nabla \cdot (\sigma \nabla u) = 0, & \text{in } \Omega, \end{array} \right. \quad (1.16)$$

$$\left\{ \begin{array}{ll} u = U_\ell, & \text{on } e_\ell, \ell = 1, 2, \dots, L, \end{array} \right. \quad (1.17)$$

$$\left\{ \begin{array}{ll} \sigma \frac{\partial u}{\partial \vec{n}} = 0, & \text{on } \partial\Omega \setminus \Gamma_e, \end{array} \right. \quad (1.18)$$

$$\left\{ \begin{array}{ll} \int_{e_\ell} \sigma \frac{\partial u}{\partial \vec{n}} ds = I_\ell, & \ell = 1, 2, \dots, L, \end{array} \right. \quad (1.19)$$

where  $I_\ell \in \mathbb{R}$  is the current injected on the  $\ell$ th electrode and  $U_\ell \in \mathbb{R}$  is the voltage on the  $\ell$ th electrode,  $\ell = 1, \dots, L$ .

Experiments show that this model underestimates the resistivity and gives worse results when the spatial frequency becomes higher. Higher spatial frequencies supposedly contain proportionately more information near and around the boundary which leads to some hypothesis that there may be an extra, unaccounted-for resistance between the electrode and the boundary [SCI92]. The said resistance is defined and accounted in the next section which results to the most accurate model for EIT.

### 1.4.4 Complete Electrode Model

We have introduced three electrode models for EIT so far: the continuum model which is the most convenient in theoretical and numerical considerations but does not typically model practical measurement setups that employ a finite number of electrodes, the gap model correctly models the geometry of the electrodes but is mainly useful when the electrodes are very small, and the shunt model that accounts the shunting effect of the electrodes but neglects to consider the effective contact impedance between the electrodes and the object [HM17].

The Complete Electrode Model (CEM) of EIT incorporates the electrode’s size, shape, shunting effect, and effective contact impedance into the forward problem [CING89; SCI92]. In CEM, the voltage experienced by an electrode is modeled more realistically as the integral average of the potential distribution

over its contact surface. It also accounts, for more accurate modeling of electrode shunting, the additional effect of the contact impedance [PLW16; Hyv04].

Effective contact impedance or surface impedance on the electrodes, denoted by  $Z \in \mathbb{R}^L$ , where

$$Z = (z_1, \dots, z_L)^T$$

characterizes the thin, highly resistive layer on the electrodes' interface due to an electrochemical effect. The contact impedance on each electrode  $z_\ell$ ,  $\ell = 1, \dots, L$  is assumed to satisfy

$$z_\ell > z_{\min}, \quad (1.20)$$

where  $z_{\min}$  is a positive constant. Accounting the contact impedance with the applied current, this results to a voltage drop on the electrodes modeled by the term  $z_\ell \sigma \partial_{\vec{n}} u$ . Hence, the Dirichlet boundary condition (1.17) is replaced by an impedance boundary condition

$$u + z_\ell \sigma \partial_{\vec{n}} u = U_\ell \text{ on } e_\ell, \quad \ell = 1, 2, \dots, L.$$

Also, we assume the properties of the electrodes (1.12), (1.13), and (1.14) defined in Section 1.4.2, and in Section 1.4.3, the current density flow on the boundary defined by conditions (1.18) and (1.19). Therefore, the resulting model is called the complete electrode model and is given by

$$\begin{cases} \nabla \cdot (\sigma \nabla u) = 0, & \text{in } \Omega, & (1.21) \\ u + z_\ell \sigma \partial_{\vec{n}} u = U_\ell, & \text{on } e_\ell, \ell = 1, 2, \dots, L, & (1.22) \\ \sigma \frac{\partial u}{\partial \vec{n}} = 0, & \text{on } \partial\Omega \setminus \Gamma_e, & (1.23) \\ \int_{e_\ell} \sigma \frac{\partial u}{\partial \vec{n}} ds = I_\ell, & \ell = 1, 2, \dots, L. & (1.24) \end{cases}$$

It was shown in [Hyv04] that CEM can be viewed as a real-world finite element approximation of the continuum model. The CEM is said to give the most accurate approximation to the resistivity according to experiments and was shown to model real-world electrode measurements reasonably well [SCI92]. It also gives good numerical reconstructions for both experimental and simulated data [Hyv04; VVSK99]. Moreover, an image reconstruction algorithm in 3D with CEM for EIT was described in [VVSK99]. In this thesis, we focus on the CEM for the forward simulations [Ags15; Hyv04; VVSK99; BKIN07; HM17; DS16].

In the next chapter, we give the existence and uniqueness results for the continuum and CEM forward problems. We also treat their numerical approximation using finite element methods.

## Chapter 2

# Study of two forward problems for EIT: the continuum model and the CEM

In the process of reconstructing the conductivity distribution, the EIT system usually consists of two parts: a forward and an inverse problem. Given the conductivity distribution of the body, a solution of the forward problem in EIT is the voltage needed to maintain the current injected around the boundary. The pair of current-voltage measurements from the forward problem gives the data for the reconstruction problem. The forward problem is then solved multiple times using different configurations of current patterns in order to generate a set of data.

In this chapter, we study in detail the existence and uniqueness results for the forward continuum and CEM. Numerical treatment and convergence result are addressed. A numerical validation using an analytic solution in the homogeneous unit disk for the CEM forward problem is performed. Lastly, numerical examples that we will be using all throughout the thesis are presented.

### 2.1 Existence and uniqueness results for forward problems

The existence and uniqueness of a solution of the continuum (2.3), and complete electrode models (1.21)–(1.24) are proven in this section [SCI92; Bor03]. First, we recall the Lax-Milgram lemma [DE12].

**Lemma 2.1.1** (Lax-Milgram). *Let  $X$  be a Hilbert space with associated norm  $\|\cdot\|_X$ , and let  $a : X \times X \rightarrow \mathbb{R}$  be a bilinear form that satisfies*

$$\begin{aligned} |a(u, w)| &\leq \alpha_0 \|u\|_X \|w\|_X, \quad \forall u, w \in X \text{ (continuity)} \\ a(u, u) &\geq \beta_0 \|u\|_X^2, \quad \forall u \in X \text{ (coercivity)}. \end{aligned}$$

*with constants  $\alpha_0, \beta_0 > 0$ . Then for any continuous linear form on  $X$ ,  $b : X \rightarrow \mathbb{R}$ , the variational formulation*

$$a(u, w) = b(w), \quad w \in X,$$

has a unique solution  $u \in X$ . Moreover, the solution  $u$  satisfies

$$\|u\|_X \leq \frac{1}{\beta_0} \|b\|_{X'},$$

where  $X'$  is the topological dual of  $X$ , i.e., the space of continuous linear forms on  $X$ .

### 2.1.1 The continuum model

Let  $\Omega \subset \mathbb{R}^d$ ,  $d = 2, 3$ , be a bounded domain with a smooth boundary  $\partial\Omega$ . We define the space for the current density on the boundary  $\tilde{L}(\partial\Omega)$  by

$$\tilde{L}(\partial\Omega) := \left\{ f \in L^2(\partial\Omega) \left| \int_{\partial\Omega} f \, ds = 0 \right. \right\}. \quad (2.1)$$

This choice ensures the conservation of charge and by consequence, the existence of a solution. Now accounting the choice of ground potentials, the solution space is defined as

$$\mathcal{H} := \left\{ u \in H^1(\Omega) \text{ such that } \int_{\partial\Omega} u \, ds = 0 \right\}. \quad (2.2)$$

Suppose  $f \in \tilde{L}(\partial\Omega)$  and  $\sigma \in L^\infty(\Omega)$  which satisfies Definition 1.2.1. Then the continuum forward problem reads as follows: find  $u \in \mathcal{H}$ , solution to

$$\begin{cases} \nabla \cdot (\sigma \nabla u) = 0, & \text{in } \Omega, \\ \sigma \partial_{\vec{n}} u = f, & \text{on } \partial\Omega. \end{cases} \quad (2.3)$$

Let  $w \in \mathcal{H}$  be an arbitrary test function. Multiplying the first equation of (2.3) by  $w$  and integrating over  $\Omega$ , we have

$$\int_{\Omega} \nabla \cdot (\sigma \nabla u) w \, d\mathbf{x} = 0.$$

Applying integration by parts and using Green's formula, we get

$$0 = \int_{\Omega} \nabla \cdot (\sigma \nabla u) w \, d\mathbf{x} = \int_{\Omega} \sigma \nabla u \cdot \nabla w \, d\mathbf{x} - \int_{\partial\Omega} \sigma (\nabla u \cdot \vec{n}) w \, ds.$$

Using the Neumann boundary condition, we obtain the following variational formulation

$$\int_{\Omega} \sigma \nabla u \cdot \nabla w \, d\mathbf{x} = \int_{\partial\Omega} f w \, ds, \quad \forall w \in \mathcal{H}. \quad (2.4)$$

We define

$$\begin{aligned} a : \mathcal{H} \times \mathcal{H} &\longrightarrow \mathbb{R} \\ (u, w) &\longmapsto \int_{\Omega} \sigma \nabla u \cdot \nabla w \, dx \\ b : \mathcal{H} &\longrightarrow \mathbb{R} \\ w &\longmapsto \int_{\partial\Omega} f w \, ds, \end{aligned}$$

which are a bilinear and linear forms, respectively. It is easy to prove that  $a$  is continuous and coercive, and  $b$  is continuous. Hence, by the Lax-Milgram lemma, the variational formulation (2.4) has a unique solution  $u \in \mathcal{H}$ .

### 2.1.2 The Complete Electrode Model

In the CEM forward problem of EIT, the resulting voltage measurements when currents are inserted on each electrode are discrete and are given by the voltage vector  $U \in \mathbb{R}^L$ . The set of solutions is defined and denoted by

$$H = H^1(\Omega) \oplus \mathbb{R}^L.$$

The Lax-Milgram lemma is used to prove the existence and uniqueness of solution of the CEM forward problem.

Let the contact electrodes  $e_\ell$ ,  $\ell = 1, 2, \dots, L$ , be open, connected subsets of  $\partial\Omega$  satisfying the properties (1.12), (1.13), and (1.14). Suppose that the conductivity function  $\sigma \in L^\infty(\Omega)$  satisfies Definition 1.2.1, and the contact impedance  $Z = (z_\ell)_{\ell=1}^L \in \mathbb{R}^L$  satisfies the relation (1.20).

We call  $I = (I_1, \dots, I_L)^T \in \mathbb{R}^L$  a current pattern if it satisfies the conservation of charge, i.e.,

$$\sum_{\ell=1}^L I_\ell = 0. \quad (2.5)$$

This ensures the existence of a solution. Meanwhile, the uniqueness of the solution is proved by imposing a choice of ground voltages. Let  $U = (U_1, \dots, U_L)^T \in \mathbb{R}^L$  be the voltage vector where the ground voltages satisfy

$$\sum_{\ell=1}^L U_\ell = 0. \quad (2.6)$$

The condition (2.6) plays an important role. The following proposition gives the variational formulation in  $H$  associated with the CEM forward problem (see [SCI92] for the detailed proof).

**Proposition 2.1.2.** *We say that  $(u, U) \in H$  is a weak solution to (1.21) subject to boundary conditions (1.22) – (1.24) if and only if for any  $(w, W) \in H$ ,*

$$B((u, U), (w, W)) = \sum_{\ell=1}^L I_\ell W_\ell, \quad (2.7)$$

where the bilinear form  $B : H \times H \rightarrow \mathbb{R}$  is defined as

$$B((u, U), (w, W)) := \int_{\Omega} \sigma \nabla u \cdot \nabla w \, d\mathbf{x} + \sum_{\ell=1}^L \int_{e_{\ell}} \frac{1}{z_{\ell}} (u - U_{\ell})(w - W_{\ell}) \, ds.$$

In order to use Lax-Milgram lemma, we need to prove the coercivity of the corresponding bilinear form. However, in the solution space  $H$ ,  $(u, U)$  is not necessarily zero if  $|B((u, U), (u, U))| = 0$ . Instead, we have

$$u = \text{constant} = U_1 = \dots = U_{\ell}.$$

This implies that  $\|u\|_H > 0$  since  $(U_{\ell})_{\ell=1}^L$  is not the null vector. Coercivity does not hold because

$$|B((u, U), (u, U))| \not\geq \|u\|_H.$$

To address this issue, we introduce the quotient space defined in [SCI92]

$$\dot{H} := H/\mathbb{R}$$

as the new space of solutions for the CEM forward problem and it is equipped with norm

$$\|(u, U)\|_{\dot{H}} = \inf(\|u - c\|_{H^1(\Omega)}^2 + \|U - C\|_{\mathbb{R}^L}^2)^{1/2}, \quad (2.8)$$

where  $c \in \mathbb{R}$  and  $C = (c)_{\ell=1}^L \in \mathbb{R}^L$ . We also note that

$$\|U - C\|_{\mathbb{R}^L} = \left( \sum_{\ell=1}^L |U_{\ell} - c|^2 \right)^{1/2}$$

and that  $(u, U)$  is equal to  $(v, V)$  in  $\dot{H}$  if

$$u - v = \text{constant} = U_1 - V_1 = \dots = U_L - V_L.$$

In spite of this, the hypotheses of the Lax-Milgram lemma are much easier to prove using a different norm in  $\dot{H}$ . Hence, we consider

$$\|(u, U)\|_* = \left( \|\nabla u\|_{L^2(\Omega)}^2 + \sum_{\ell=1}^L \int_{e_{\ell}} |u - U_{\ell}|^2 \, ds \right)^{1/2}. \quad (2.9)$$

The equivalence between the two norms,  $\|\cdot\|_{\dot{H}}$  and  $\|\cdot\|_*$ , was shown in Lemma 3.2 of [SCI92].

**Lemma 2.1.3.** *The norms,  $\|\cdot\|_{\dot{H}}$  (2.8) and  $\|\cdot\|_*$  (2.9), are equivalent, i.e., for some constants  $0 < \lambda_1 \leq \lambda_2 < \infty$ ,*

$$\lambda_1 \|(u, U)\|_* \leq \|(u, U)\|_{\dot{H}} \leq \lambda_2 \|(u, U)\|_*,$$

for all  $(u, U) \in \dot{H}$ .

We can conclude the existence and uniqueness of a weak solution for the CEM forward problem by the following theorem.

**Theorem 2.1.4.** *Suppose the conductivity  $\sigma \in L^\infty(\Omega)$  satisfy Definition 1.2.1. Let the contact impedance  $Z \in \mathbb{R}^L$  fulfill the condition (1.20). Then for a given current pattern  $I = (I_\ell)_{\ell=1}^L \in \mathbb{R}^L$  satisfying the conservation of charge (2.5), there is a unique  $(u, U)$  in  $\dot{H}$  satisfying*

$$B((u, U), (w, W)) = \sum_{\ell=1}^L I_\ell W_\ell, \quad (2.10)$$

for all  $(w, W) \in \dot{H}$ .

*Proof.* Suppose the hypotheses of the theorem hold. Note that in Proposition 2.1.2,  $B$  is defined as a bilinear form. We first need to prove that  $B$  is continuous on  $\dot{H}$ . We have

$$|B((u, U), (w, W))|^2 = \left| \int_{\Omega} \sigma \nabla u \cdot \nabla w \, d\mathbf{x} + \sum_{\ell=1}^L \int_{e_\ell} \frac{1}{z_\ell} (u - U_\ell)(w - W_\ell) \, ds \right|^2.$$

By the assumption on the conductivity, and applying the Cauchy-Schwarz inequality for  $L^2(\Omega)$ , we get

$$\begin{aligned} |B((u, U), (w, W))|^2 &\leq \sigma_{\max}^2 \|\nabla u\|_{L^2(\Omega)}^2 \|\nabla w\|_{L^2(\Omega)}^2 + \left| \sum_{\ell=1}^L \int_{e_\ell} \frac{1}{z_\ell} (u - U_\ell)(w - W_\ell) \, ds \right|^2 \\ &\quad + 2\sigma_{\max} \|\nabla u\|_{L^2(\Omega)} \|\nabla w\|_{L^2(\Omega)} \left| \sum_{\ell=1}^L \int_{e_\ell} \frac{1}{z_\ell} (u - U_\ell)(w - W_\ell) \, ds \right|. \end{aligned}$$

We express the integrals on the electrodes as an integral on the boundary by using the characteristic function  $\chi_\ell$  on the  $\ell$ th electrode and we write

$$\begin{aligned} |B((u, U), (w, W))|^2 &\leq \sigma_{\max}^2 \|\nabla u\|_{L^2(\Omega)}^2 \|\nabla w\|_{L^2(\Omega)}^2 + \left| \int_{\partial\Omega} \sum_{\ell=1}^L \left[ \frac{1}{z_\ell} (u - U_\ell)(w - W_\ell) \right] \chi_\ell \, ds \right|^2 \\ &\quad + 2\sigma_{\max} \|\nabla u\|_{L^2(\Omega)} \|\nabla w\|_{L^2(\Omega)} \left| \int_{\partial\Omega} \sum_{\ell=1}^L \left[ \frac{1}{z_\ell} (u - U_\ell)(w - W_\ell) \right] \chi_\ell \, ds \right|. \end{aligned}$$

The assumption on the contact impedance  $Z$  implies that

$$\frac{1}{|z_\ell|} < \frac{1}{Z_{\min}}, \forall \ell = 1, 2, \dots, L.$$

We can simplify the variational formulation

$$\begin{aligned}
|B((u, U), (w, W))|^2 &\leq \sigma_{\max}^2 \|\nabla u\|_{L^2(\Omega)}^2 \|\nabla w\|_{L^2(\Omega)}^2 + \frac{1}{Z_{\min}^2} \left| \int_{\partial\Omega} \sum_{\ell=1}^L (u - U_\ell)(w - W_\ell) \chi_\ell \, ds \right|^2 \\
&\quad + \frac{2\sigma_{\max}}{Z_{\min}} \|\nabla u\|_{L^2(\Omega)} \|\nabla w\|_{L^2(\Omega)} \left| \int_{\partial\Omega} \sum_{\ell=1}^L (u - U_\ell)(w - W_\ell) \chi_\ell \, ds \right|. \\
&\leq \max \left\{ \sigma_{\max}^2, \frac{\sigma_{\max}}{Z_{\min}}, \frac{1}{Z_{\min}^2} \right\} \left[ \|\nabla u\|_{L^2(\Omega)}^2 + \sum_{\ell=1}^L \int_{e_\ell} |u - U_\ell|^2 \, ds \right] \\
&\quad \times \left[ \|\nabla w\|_{L^2(\Omega)}^2 + \sum_{\ell=1}^L \int_{e_\ell} |w - W_\ell|^2 \, ds \right] \\
&\leq K \|(u, U)\|_*^2 \|(w, W)\|_*^2,
\end{aligned}$$

where  $K$  is a positive constant. Using the norm equivalence given in Lemma 2.1.3,  $B$  is continuous on  $\dot{H}$ . Next, the coercivity of  $B$  on  $\dot{H}$  also follows because we have for all  $(u, U)$ ,

$$\begin{aligned}
|B((u, U), (u, U))| &= \left| \int_{\Omega} \sigma |\nabla u|^2 \, dx + \sum_{\ell=1}^L \int_{e_\ell} \frac{1}{z_\ell} |u - U_\ell|^2 \, ds \right| \\
&\geq \min \left\{ \sigma_{\min}, \min_{\ell=1, \dots, L} \frac{1}{|z_\ell|} \right\} \left( \|\nabla u\|_{L^2(\Omega)}^2 + \sum_{\ell=1}^L \int_{e_\ell} |u - U_\ell|^2 \, ds \right) \\
&\geq \tilde{K} \|(u, U)\|_*^2,
\end{aligned}$$

with a positive constant  $\tilde{K}$ . Finally, we define a linear map

$$\begin{aligned}
g: \quad \dot{H} &\longrightarrow \mathbb{R} \\
(w, W) &\longmapsto \sum_{\ell=1}^L I_\ell W_\ell.
\end{aligned}$$

Note that  $g$  is well-defined since if  $(w, W) = (\tilde{w}, \tilde{W})$ , then  $w - \tilde{w} = \text{constant} = W_1 - \tilde{W}_1 = \dots = W_L - \tilde{W}_L$ . Thus, by the conservation of charge (2.5)

$$g(w, W) = \sum_{\ell=1}^L I_\ell W_\ell = \sum_{\ell=1}^L I_\ell (W_\ell - \text{constant}) = \sum_{\ell=1}^L I_\ell \tilde{W}_\ell = g(\tilde{w}, \tilde{W}).$$

Furthermore, we choose a constant  $c \in \mathbb{R}$  such that

$$(\|w - c\|_{H^1(\Omega)}^2 + \|W - C\|_{\mathbb{R}^L}^2)^{1/2} \leq \|(w, W)\|_{\dot{H}} + \epsilon,$$

where  $\epsilon > 0$ . Thus, by the conservation of charge, we have  $\forall(w, W) \in \dot{H}$

$$\begin{aligned} |g(w, W)| &= \left| \sum_{\ell=1}^L I_\ell W_\ell \right| = \left| \sum_{\ell=1}^L I_\ell (W_\ell - c) \right| \\ &\leq \|I\|_{\mathbb{R}^L} \|W - C\|_{\mathbb{R}^L} \\ &\leq \|I\|_{\mathbb{R}^L} (\|(w, W)\|_{\dot{H}} + \epsilon). \end{aligned}$$

Since  $I \in \mathbb{R}^L$  and  $\epsilon$  is arbitrary, we obtain

$$|g(w, W)| \leq K \|(w, W)\|_{\dot{H}}, \quad K > 0.$$

This implies that  $g$  is also continuous. By the Lax-Milgram lemma, there exists a unique solution  $(u, U) \in \dot{H}$  for (2.10).  $\square$

The theorem above ensures the uniqueness in  $\dot{H}$  up to a constant. The choice of ground potential (2.6) is imposed in order to obtain the uniqueness in  $H$ . Assume that there are two solutions  $(u, U)$  and  $(\tilde{u}, \tilde{U})$  of the CEM forward problem satisfying (1.21) – (1.24). Let  $(w, W) = (u, U) - (\tilde{u}, \tilde{U})$ . Hence we have  $(w, W)$  satisfying the following boundary-value problem

$$\begin{cases} \nabla \cdot (\sigma \nabla w) = 0 & \text{in } \Omega, & (2.11) \\ w + z_\ell \sigma \partial_{\bar{n}} w = W_\ell & \text{on } e_\ell, \ell = 1, 2, \dots, L, & (2.12) \\ \sigma \partial_{\bar{n}} w = 0 & \text{on } \partial\Omega \setminus \Gamma_e, & (2.13) \\ \int_{e_\ell} \sigma \partial_{\bar{n}} w \, ds = 0 & \ell = 1, 2, \dots, L. & (2.14) \end{cases}$$

Multiplying the same test function  $w$  to (2.11), integrating by parts, and applying the Green's Theorem, we have

$$\int_{\Omega} \sigma |\nabla w|^2 \, d\mathbf{x} = \int_{\partial\Omega} w \sigma \partial_{\bar{n}} w \, ds = - \sum_{\ell=1}^L z_\ell \int_{e_\ell} |\sigma \partial_{\bar{n}} w|^2 \, ds.$$

Since  $z_\ell \geq 0$ ,  $\forall \ell = 1, \dots, L$ , both sides of the equation above are forced to be equal to zero. This implies that  $w$  is constant. Moreover, by (2.12), we have

$$w = \text{constant} = W_\ell, \quad \ell = 1, \dots, L.$$

The choice of ground potential (2.6) leads to

$$\sum_{\ell=1}^L U_\ell = 0 = \sum_{\ell=1}^L \tilde{U}_\ell.$$

Thus, we get,

$$\sum_{\ell=1}^L W_\ell = 0.$$

Since all the voltages on the electrodes are equal to the same constant, the sum above forces the constant to be zero.

$$W_\ell = 0 = w, \quad \ell = 1, \dots, L.$$

This proves the uniqueness of the solution in  $H$  of the CEM forward problem.

Lastly, for convenience, we introduce the spaces

$$\mathbb{R}_\diamond^L := \left\{ U = (U_\ell)_{\ell=1}^L \in \mathbb{R}^L \mid \sum_{\ell=1}^L U_\ell = 0 \right\}$$

and

$$H_\diamond := H^1(\Omega) \oplus \mathbb{R}_\diamond^L.$$

The existence and uniqueness results given above and in Theorem 2.1.4 extend to  $H_\diamond$ .

*Remark 1.* The uniqueness result above is supported by the equivalence of the norms of the quotient space  $H_\diamond/\mathbb{R}$  and  $H_\diamond$ . The norm equivalence is from the continuous and bijective embedding  $H_\diamond \hookrightarrow H_\diamond/\mathbb{R}$  due to

$$\begin{aligned} \|(u, U)\|_{H_\diamond/\mathbb{R}}^2 &= \|\nabla u\|_{L^2(\Omega)}^2 + \inf_{c \in \mathbb{R}} \{ \|u + c\|_{L^2(\Omega)} + |U + c|_2^2 \} \\ &\leq \|\nabla u\|_{L^2(\Omega)}^2 + \|u\|_{L^2(\Omega)} + |U|_2^2 \\ &\leq \|(u, U)\|_{H_\diamond}. \end{aligned}$$

## 2.2 Discretization using Finite Element Method

In solving PDEs numerically, there are usually two main approaches: the Finite Difference Method and the Finite Element Method (FEM). The latter approach is usually employed when dealing with complex geometries. We consider it for the discretization of the different variational problems of this thesis. In particular, consider the continuous variational problem on a Hilbert space  $X$ : find  $u \in X$  such that

$$a(u, w) = b(w), \quad \forall w \in X.$$

The basic principle of the finite element method consists of replacing the Hilbert space  $X$  of the continuous weak formulation with a finite-dimensional subspace  $X_h$  of  $X$  [Bra02; DE12; Cia78]. The corresponding discrete weak formulation reads: find  $u_h \in X_h$  such that

$$a(u_h, w_h) = b(w_h), \quad \forall w_h \in X_h.$$

In this section, we apply the Lagrange Finite-Element Method for the discretization of the variational formulations obtained in the previous section. We then proceed to the numerical treatment of the continuum and CEM forward problems using FEM.

### 2.2.1 Lagrange Finite-Element Method

Consider a triangulation  $\mathcal{T}_h$  of the domain  $\Omega$  satisfying the properties stated in [Cia78]. In particular, the mesh  $\mathcal{T}_h$  is a collection of geometrically simple elements  $K$ , called finite elements, with the parameter  $h$  equal to

$$h = \max_{K \in \mathcal{T}_h} \text{diam}(K).$$

Furthermore, for any  $h$ , we denote by  $\Omega_h = \bigcup_{K \in \mathcal{T}_h} K$  the discrete domain and by  $\mathcal{N}$  the set of nodes of  $\mathcal{T}_h$ . On  $\mathcal{T}_h$ , we introduce the standard vector space of Lagrange finite element of type P1

$$X_h = \{v_h \in \mathcal{C}^0(\overline{\Omega_h}) \mid v_{h|K} \in \mathbb{P}_1(K) \forall K \in \mathcal{T}_h\}, \quad (2.15)$$

where  $\dim X_h = N$ , and  $\mathbb{P}_1(K)$  denotes the space of polynomials of degree less than or equal to 1 on  $K$ . We also define the discretization space  $V_h = X_h \cap L^2(\Omega_h)$  of P1 finite elements with zero mean value on  $\Omega_h$ .

Lastly, a basis of  $X_h$  is typically composed of functions whose support is restricted on one or few elements of  $\mathcal{T}_h$  and the polynomials are usually of low degree. Let the  $k$ th basis function at the  $i$ th node be defined by

$$\varphi_k(\mathbf{x}_i) = \delta_{ki}, \quad \mathbf{x}_i \in \mathcal{N}, \quad 1 \leq i, k \leq N \quad (2.16)$$

for  $i = 1, \dots, N$ , where  $\varphi_k \in X_h$ . Denote  $\mathcal{B}_h := \{\varphi_k, k = 1, 2, \dots, N\}$  as the set of basis functions. We can now express the elements of  $X_h$  as a linear combination of these basis functions and we can define the corresponding discrete forms of both the continuum and CEM variational problems. These are discussed in detail in the succeeding sections.

To summarize, in using FEM to solve the forward problem, we first determine the variational formulation of the problem. The discretized variational formulation can be expressed as a system of linear equations, i.e.,  $Au_h = B$ . The unknown  $u_h$  is the vector of values of the potential function at each node and the linear system is usually solved by a direct sparse solver.

### 2.2.2 Discretization of the continuum forward problem

Consider the continuum forward model given by (2.3) with the following variational problem: find  $u \in \mathcal{H}$  such that for any  $w \in \mathcal{H}$ ,

$$a(u, w) := \int_{\Omega} \sigma \nabla u \cdot \nabla w \, d\mathbf{x} = \int_{\partial\Omega} f w \, ds =: b(w).$$

To impose the conservation of charge in the space of  $\tilde{L}(\partial\Omega)$ , a penalty method is used. In particular, a Lagrange multiplier  $\lambda \in \mathbb{R}$  is introduced to the variational formulation as a penalty and thus, we have the following resulting variational

problem: find  $u \in \mathcal{H}$  such that  $\forall w \in \mathcal{H}$ ,

$$\begin{cases} \int_{\Omega} \sigma \nabla u \cdot \nabla w \, d\mathbf{x} + \int_{\Omega} \lambda w \, d\mathbf{x} = \int_{\partial\Omega} f w \, ds \\ \int_{\Omega} u \, d\mathbf{x} = 0. \end{cases} \quad (2.17)$$

We consider a triangular mesh  $\mathcal{T}_h$  for 2D geometries  $\Omega$  and on  $\mathcal{T}_h$ , we introduce  $X_h$ , the standard vector space of Lagrange finite elements of type P1 and  $\mathcal{B}_h$ , the set of basis functions in  $X_h$ . The approximation  $u_h \in X_h$  of the electric potential  $u$  is of the form

$$u_h(\mathbf{x}) = \sum_{j=1}^N v_j \varphi_j(\mathbf{x}), \quad \mathbf{x} \in \Omega_h, \quad (2.18)$$

where  $v_j$  is an approximation of the value of the potential  $u$  at  $\mathbf{x}_j \in \Omega_h$ , and  $\varphi_j$ 's are linear basis functions defined by (2.16). We set  $w(\mathbf{x}) = \varphi_i(\mathbf{x})$ , for  $i = 1, 2, \dots, N$ . Upon substituting (2.18) to (2.17), for each  $i = 1, \dots, N$ ,

$$\begin{cases} \sum_{j=1}^N v_j \left( \int_{\Omega} \sigma \nabla \varphi_i \cdot \nabla \varphi_j \, d\mathbf{x} \right) + \lambda \left( \int_{\Omega} \varphi_i \, d\mathbf{x} \right) = \sum_{j=1}^N f_j \int_{\partial\Omega} \varphi_i \varphi_j \, ds \\ v_j \left( \int_{\Omega} \varphi_j \, d\mathbf{x} \right) = 0. \end{cases}$$

We obtain a linear system of order  $N + 1$  which can be written in the following matrix form:

$$\begin{bmatrix} A & b \\ b^T & 0 \end{bmatrix} \begin{bmatrix} v \\ \lambda \end{bmatrix} = \begin{bmatrix} g \\ 0 \end{bmatrix}, \quad (2.19)$$

where  $v = (v_j)_{j=1}^N$ ,  $A = (A_{ij}) \in \mathbb{R}^{N \times N}$  of coefficients  $A_{ij} = \int_{\Omega} \sigma \nabla \varphi_j \cdot \nabla \varphi_i \, d\mathbf{x}$ ,  $b = (b_i) \in \mathbb{R}^N$  with  $b_i = \int_{\Omega} \varphi_i \, d\mathbf{x}$ ,  $g = (g_i) \in \mathbb{R}^N$  of elements  $g_i = \sum_{j=1}^N f_j \int_{\partial\Omega} \varphi_i \varphi_j \, ds$ , and  $\lambda \in \mathbb{R}$ .

*Remark 2.* The matrix  $A$  is symmetric and semi-positive definite by the properties of the bilinear form  $a$  and the conductivity distribution  $\sigma$  [Dia17; Cra17]. Furthermore, by implementing the choice of ground potential, the linear system (2.19) admits a unique solution [Cra17].

### 2.2.3 Discretization of the CEM forward problem

Consider the problem described by the equations (1.21)–(1.24). Note that we use the variational formulation defined by (2.10): find  $(u, U) \in H_{\diamond}$  such that  $\forall (w, W) \in H_{\diamond}$

$$\int_{\Omega} \sigma \nabla u \cdot \nabla w \, d\mathbf{x} + \sum_{\ell=1}^L \frac{1}{z_{\ell}} \int_{e_{\ell}} (u - U_{\ell})(w - W_{\ell}) \, ds = \sum_{\ell=1}^L I_{\ell} W_{\ell}.$$

We consider a triangular mesh  $\mathcal{T}_h$  of the domain and the corresponding standard vector space  $X_h$  (2.15) of Lagrange finite elements of type P1 as in the previous section. Recall that  $X_h$  defines a finite-dimensional subspace of  $H^1(\Omega)$ . The approximation  $u_h \in X_h$  of the electric potential  $u$  is expressed as

$$u_h(\mathbf{x}) = \sum_{j=1}^N v_j \varphi_j(\mathbf{x}), \quad \mathbf{x} \in \Omega_h. \quad (2.20)$$

We focus on the numerical implementation proposed in [KKS00] and we explain here the main lines of the approach.

To impose the uniqueness condition (2.6), a different representation of the voltage  $U$  is used. Define a set of vectors  $\phi_\ell \in \mathbb{R}^L$ ,  $\ell = 1, \dots, L-1$ , by  $\phi_1 = (1, -1, 0, \dots, 0)^T$ ,  $\phi_2 = (1, 0, -1, \dots, 0)^T$ ,  $\dots$ ,  $\phi_{L-1} = (1, 0, \dots, -1)^T$ . Thus, the approximation  $U_h$  of the vector  $U$  is given by

$$U_h = \sum_{k=1}^{L-1} \beta_k \phi_k \in \mathbb{R}_\diamond^L, \quad (2.21)$$

where  $\beta_k \in \mathbb{R}$ ,  $k = 1, \dots, L-1$ . Let  $\beta = (\beta_k)^T \in \mathbb{R}^{L-1}$  and define the matrix  $P = (\phi_1 | \dots | \phi_{L-1}) \in \mathbb{R}^{L \times L-1}$ . Thus, the voltages  $U_h$  are determined by

$$U_h = P\beta. \quad (2.22)$$

Consider the test functions  $(w, W) = (\varphi_i, \mathbf{0})$ . Substituting (2.20) – (2.21) to (2.10), we get for each  $i = 1, \dots, N$

$$\sum_{j=1}^N v_j \int_{\Omega} \sigma \nabla \varphi_j \cdot \nabla \varphi_i \, d\mathbf{x} + \sum_{\ell=1}^L \frac{1}{z_\ell} \int_{e_\ell} \left( \sum_{j=1}^N v_j \varphi_j - \sum_{k=1}^{L-1} \beta_k \phi_k \right) \varphi_i \, ds = 0.$$

This yields the following linear system

$$\begin{bmatrix} S + M & C \end{bmatrix} \begin{bmatrix} v \\ \beta \end{bmatrix} = \begin{bmatrix} \mathbf{0}_{\mathbb{R}^N} \end{bmatrix}, \quad (2.23)$$

where  $v = (v_j)_{j=1}^N$ ,  $S = (S_{ij}) \in \mathbb{R}^{N \times N}$  of coefficients

$$S_{ij} = \int_{\Omega} \sigma \nabla \varphi_i \cdot \nabla \varphi_j \, d\mathbf{x}, \quad (2.24)$$

$M = (M_{ij}) \in \mathbb{R}^{N \times N}$  with

$$M_{ij} = \sum_{\ell=1}^L \frac{1}{z_\ell} \int_{e_\ell} \varphi_i \varphi_j \, ds, \quad (2.25)$$

and  $C = (C_{i\ell}) \in \mathbb{R}^{N \times (L-1)}$  with

$$C_{i\ell} = - \left( \frac{1}{z_1} \int_{e_1} \varphi_i ds - \frac{1}{z_{\ell+1}} \int_{e_{\ell+1}} \varphi_i ds \right). \quad (2.26)$$

Moreover, the conditions (1.22) and (1.23) give

$$\frac{1}{z_\ell} \int_{e_\ell} (U_\ell - u) ds = I_\ell, \quad \ell = 1, 2, \dots, L. \quad (2.27)$$

Then, the approximations (2.20) and (2.21) are used in (2.27). In order to obtain a symmetric system of equations at the end, the number of equations above should be reduced to  $L - 1$  which is done by subtracting from  $I_1$  all the remaining current values  $I_\ell$ ,  $\ell = 2, 3, \dots, L$ .

$$\begin{aligned} I_1 - I_2 &= \sum_{j=1}^N \left( -\frac{1}{z_1} \int_{e_1} \varphi_j ds + \frac{1}{z_2} \int_{e_2} \varphi_j ds \right) u_j^h + \left( \frac{1}{z_1} \int_{e_1} ds + \frac{1}{z_2} \int_{e_2} ds \right) \beta_1 \\ &\quad + \sum_{\ell=1, \ell \neq 1}^{L-1} \left( \frac{1}{z_1} \int_{e_1} ds \right) \beta_\ell \end{aligned}$$

$$\begin{aligned} I_1 - I_3 &= \sum_{j=1}^N \left( -\frac{1}{z_1} \int_{e_1} \varphi_j ds + \frac{1}{z_3} \int_{e_3} \varphi_j ds \right) u_j^h + \left( \frac{1}{z_1} \int_{e_1} ds + \frac{1}{z_3} \int_{e_3} ds \right) \beta_2 \\ &\quad + \sum_{\ell=1, \ell \neq 2}^{L-1} \left( \frac{1}{z_1} \int_{e_1} ds \right) \beta_\ell \end{aligned}$$

⋮

$$\begin{aligned} I_1 - I_L &= \sum_{j=1}^N \left( -\frac{1}{z_1} \int_{e_1} \varphi_j ds + \frac{1}{z_L} \int_{e_L} \varphi_j ds \right) u_j^h + \left( \frac{1}{z_1} \int_{e_1} ds + \frac{1}{z_L} \int_{e_L} ds \right) \beta_{L-1} \\ &\quad + \sum_{\ell=1, \ell \neq L-1}^{L-1} \left( \frac{1}{z_1} \int_{e_1} ds \right) \beta_\ell. \end{aligned}$$

Note that  $\int_{e_\ell} ds = |e_\ell|$ , where  $|e_\ell|$  is the length (respectively the area) of the electrode in the two-dimensional case (respectively in the three-dimensional case) and that  $P^T I = (I_1 - I_2, I_1 - I_3, \dots, I_1 - I_L)^T$ . Therefore, we have the following matrix form of the  $L - 1$  equations equivalent to (2.27)

$$\begin{bmatrix} C^T & G \end{bmatrix} \begin{bmatrix} v \\ \beta \end{bmatrix} = \begin{bmatrix} P^T I \end{bmatrix}, \quad (2.28)$$

where  $G \in \mathbb{R}^{(L-1) \times (L-1)}$  is given by

$$G_{ik} = \begin{cases} \frac{|e_1|}{z_1} & , \quad i \neq k \\ \frac{|e_1|}{z_1} + \frac{|e_{k+1}|}{z_{k+1}} & , \quad i = k. \end{cases} \quad (2.29)$$

Finally, an approximate solution of the CEM is obtained by solving the following linear system of size  $N + L - 1$

$$\underbrace{\begin{bmatrix} S + M & C \\ C^T & G \end{bmatrix}}_{:= K} \begin{bmatrix} v \\ \beta \end{bmatrix} = \begin{bmatrix} \mathbf{0}_{\mathbb{R}^N} \\ P^T I \end{bmatrix}, \quad (2.30)$$

where the matrix  $K \in \mathbb{R}^{(N+L-1) \times (N+L-1)}$  is sparse, symmetric and positive-definite [Cra17; KKS00; LR06]. The vector  $v = (v_j)_j \in \mathbb{R}^N$  gives the approximation  $u_h$  of the potential  $u$ , and  $\beta$  leads to the calculation of the voltages  $U_h$  at electrodes via (2.22).

## 2.3 Numerical validation of the CEM in the homogeneous unit disk case

Analytical solutions for the CEM forward problem are available for some particular domains. Semi-analytic solutions for homogeneous conductivities on the unit disk was discussed in [Dem11] and on a 2D square domain in [Cra17]. Moreover, in [SCI92], the analytical solution of the CEM on a body with  $N$ -rings and constant real-valued conductivity was derived. In this section, we implement our code with FreeFem++ [SCI92] and the numerical validation is performed for the unit disk with homogeneous conductivity.

### 2.3.1 Set-up and analytical solution

In a circular body  $\Omega$  with radius  $r_n = 1$  in two dimensions, attach  $L = 16$  identical, equally-spaced electrodes, on its boundary. Let the midpoints of the electrodes  $e_\ell, \ell = 1, 2, \dots, L$ , be given by  $\theta_\ell = 2\pi\ell/L, \ell = 1, 2, \dots, L$ , and the current injected on each electrode be  $I_\ell$ . The angular width of an electrode is assumed to be constant for all electrodes. The current pattern  $I = (I_\ell)_{\ell=1}^L$  follows the symmetry of the cosine function, that is,  $I_\ell = I_{- \ell} = I_{L-\ell}, \ell = 0, 1, \dots, L - 1$ . Note that there is a shift in the indexes of the electrodes where  $e_0$  corresponds to  $e_L$ .

Assume that the contact impedance values are equal on each electrode, i.e.,  $z_\ell = z$ , where  $z$  is a positive constant. Moreover, the body  $\Omega$  is the unit disk with constant real conductivity distribution,

$$\sigma = \sigma(r) = 1 \quad \text{for } 0 < r < 1.$$

We have the following form of analytical solution for CEM

$$u(r, \theta) = \sum_{m=1}^{\infty} \frac{1}{\sqrt{m}} \left[ a_m^{(n)} \left( \frac{r_n}{r} \right)^m + b_m^{(n)} \left( \frac{r}{r_n} \right)^m \right] \cos(m\theta), \quad (2.31)$$

where  $r_1 := 0 < r < 1 := r_n$  and  $\theta \in [0, 2\pi]$ . In order to define  $u$  at the origin, i.e.,  $r = 0$ , we assume that  $a_m^{(1)} = 0$ . To form the above equation, we need to compute the Fourier coefficients  $a_m^{(n)}$  and  $b_m^{(n)}$ . We refer the reader to [SCI92] for the detail on how to get the said coefficients.

### 2.3.2 Numerical validation

The analytical solution (2.31) is expressed as an infinite series. We thus take a truncated series of the exact solution which can be easily computed. Let us denote by  $M$  the truncation number. Furthermore, since (2.31) is undefined when  $r = 1$ , the analytical solution is restricted to  $r \leq 0.8$ . We consider three triangular meshes with decreasing mesh size  $h$  (Table 2.1).

Mesh	Nodes	Triangle Elements	$h_{\min}$	$h_{\max}$
$M_1$	2 896	1 513	0.035	0.079
$M_2$	14 374	7 332	0.015	0.037
$M_3$	120 426	60 630	0.005	0.017

TABLE 2.1: Mesh description of a disk

The discretization of CEM is realized as explained in Section 2.2.3. All simulations are executed with the software FreeFem++ [Hec12]. The linear system (2.30) is solved with a direct sparse solver. The analytical solution is calculated with Matlab. We compare three values of contact impedance:  $z = 0.001$ ,  $z = 0.01$ , and  $z = 0.1$ . We first cite the work of Dardé and Staboulis [DS16] which have studied the effect of contact impedance in the regularity and convergence of the finite-element method for CEM by comparing it to that of the shunt model. In particular, FEM gives more accurate approximation for CEM when  $z \gg 0$ . We also note the result of Crabb [Cra17] that demonstrates how the solution becomes unbounded as the contact impedance decreases. Moreover, convergence rates that are smaller than  $\mathcal{O}(h^{1-\epsilon})$  and  $\mathcal{O}(h^{2-\epsilon})$  as  $h \rightarrow 0$  in the  $H^1$  and  $L^2$  norms, respectively, are likely to be obtained.

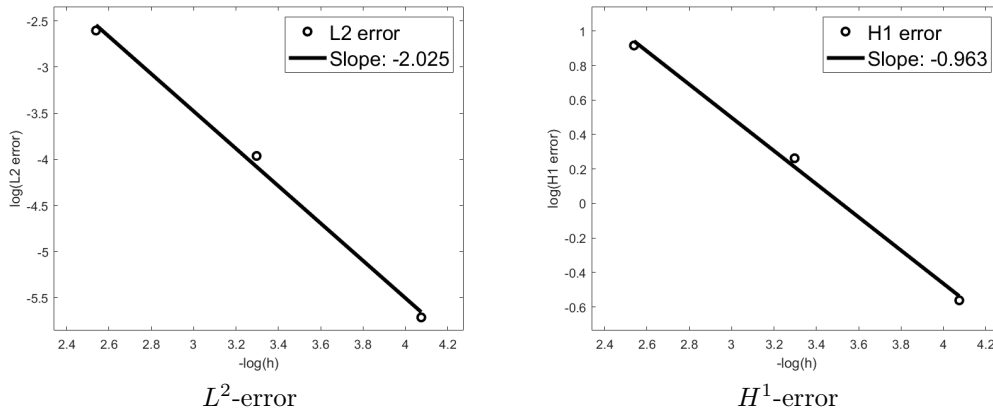
#### Case when $z = 0.001$

The truncation number is  $M = 1020$ . Table 2.2 displays the  $L^2$  and  $H^1$  errors of the potential  $u$  and the Euclidean error of the boundary voltage  $U$ . Meanwhile, Table 2.3 gives the numerical estimation of the convergence order for  $u$  and  $U$ , and Figure 2.1 displays the plot for the  $H^1$  and  $L^2$  errors of  $u_h$ .

Mesh	$\ u - u_h\ _{L^2}$	$\ u - u_h\ _{H^1}$	$\ U - U_h\ _2$
$M_1$	7.4E-02	2.5E-00	4.8E-01
$M_2$	1.9E-02	1.3E-00	1.4E-01
$M_3$	3.3E-03	5.7E-01	2.8E-02

 TABLE 2.2: Case when  $z = 0.001$ : errors on potential  $u$  and  $U$ 

Error	$\ u - u_h\ _{L^2}$	$\ u - u_h\ _{H^1}$	$\ U - U_h\ _2$
Numerical convergence order	-2.025	-0.963	-1.894

 TABLE 2.3: Case when  $z = 0.001$ : numerical validation of the FEM solver convergence

 FIGURE 2.1: Unit disk. Case when  $z = 0.001$ .  $\sigma = 1$ . Errors  $u - u_h$  in  $L^2$  norm (left) and  $H^1$  norm with respect to the mesh size  $h$  in logarithm scale.

### Case when $z = 0.01$

We fix  $M = 680$ . Tables 2.4, 2.5, and Figure 2.2 summarize the convergence results of the solver.

Mesh	$\ u - u_h\ _{L^2}$	$\ u - u_h\ _{H^1}$	$\ U - U_h\ _2$
$M_1$	1.5E-02	5.1E-01	1.5E-01
$M_2$	4.3E-03	2.8E-01	4.6E-02
$M_3$	7.3E-04	1.2E-01	8.6E-03

 TABLE 2.4: Case when  $z = 0.01$ : errors on potential  $u$  and  $U$

Error	$\ u - u_h\ _{L^2}$	$\ u - u_h\ _{H^1}$	$\ U - U_h\ _2$
Numerical convergence order	-1.969	-0.942	-1.912

TABLE 2.5: Case when  $z = 0.01$ : numerical validation of the FEM solver convergence

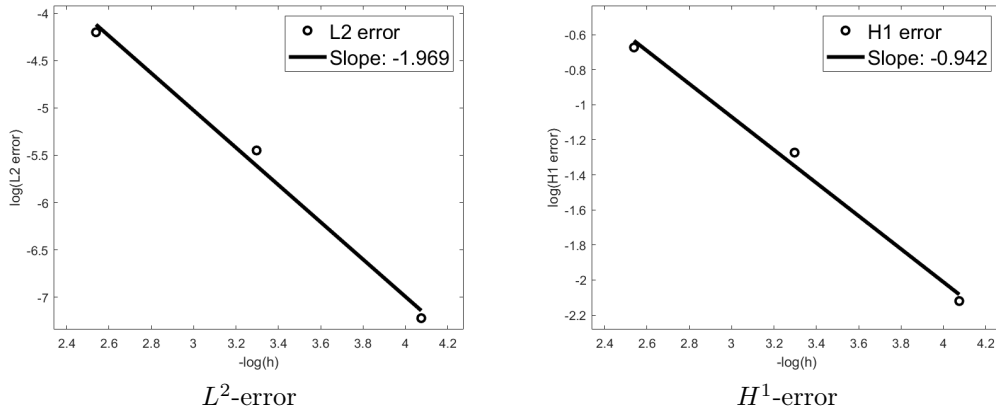


FIGURE 2.2: Unit disk. Case when  $z = 0.01$ .  $\sigma = 1$ . Errors  $u - u_h$  in  $L^2$  norm (left) and  $H^1$  norm with respect to the mesh size  $h$  in logarithm scale

### Case when $z = 0.1$

Let  $M = 360$  be the optimal truncation number. Results are presented in Tables 2.6, 2.7, and Figure 2.3.

Mesh	$\ u - u_h\ _{L^2}$	$\ u - u_h\ _{H^1}$	$\ U - U_h\ _2$
$M_1$	1.5E-03	5.0E-02	6.6E-02
$M_2$	4.0E-04	2.7E-02	1.8E-02
$M_3$	5.8E-05	9.9E-03	2.8E-03

TABLE 2.6: Case when  $z = 0.1$ : errors on potential  $u$  and  $U$

Error	$\ u - u_h\ _{L^2}$	$\ u - u_h\ _{H^1}$	$\ U - U_h\ _2$
Numerical convergence order	-2.119	-1.055	-2.105

TABLE 2.7: Case when  $z = 0.1$ : numerical validation of the FEM solver convergence

We observe that the approximation errors of  $u_h$  and  $U_h$  decreases when the value of the contact impedance increases. This is in accordance with the conclusion in [DS16], that is, FEM gives more accurate approximation for the CEM when  $z \gg 0$ . It also affirms the unboundedness of the solution as the

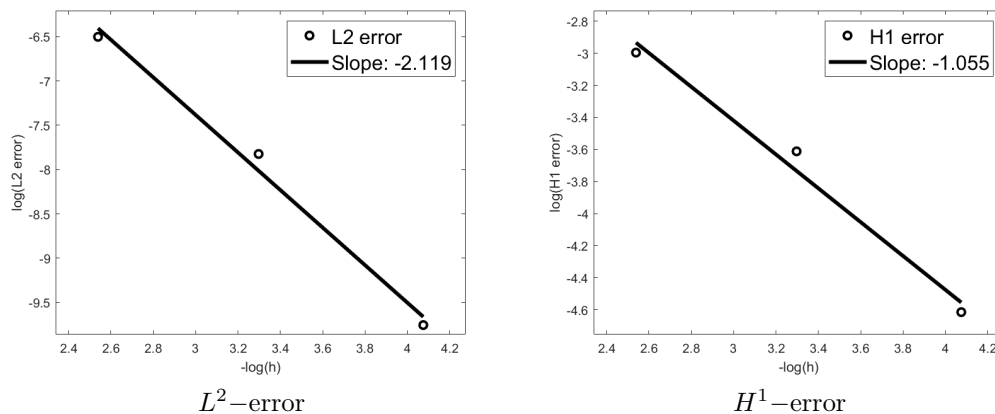


FIGURE 2.3: Unit disk. Case when  $z = 0.1$ .  $\sigma = 1$ . Errors  $u - u_h$  in  $L^2$  norm (left) and  $H^1$  norm with respect to the mesh size  $h$  in logarithm scale

contact impedance decreases [Cra17]. The  $H^1$  and  $L^2$  errors for  $u_h$ , and the error of  $U_h$  using Euclidean norm corroborate the classical predicted theoretical convergence estimates. This validates our code.

## 2.4 Numerical simulations

All throughout the document, the following domain cases and conductivity distributions are considered for the numerical examples or in some cases, there might be changes in some parameters which will be mentioned. The conductivity distribution for each configuration is shown in Figure 2.4. We plotted the conductivity distribution in a very fine mesh.

Case 1a. *Unit disk*. The conductivity distribution is homogeneous with value equal to  $\sigma_0 = 0.33 \text{ S} \cdot \text{m}^{-1}$ .

Case 1b. *Unit disk with one elliptical inclusion*. We take the unit disk, and the general equation of the elliptical inclusion is represented by the following equation.

$$a[(x - h) \cos \theta + (y - k) \sin \theta]^2 + b[(x - h) \sin \theta - (y - k) \cos \theta]^2 = r^2.$$

The center of the ellipse is  $(h, k) = (-0.4, 0.5)$ , the lengths are  $(a, b) = (0.4, 0.7)$ , the rotation angle is  $\theta = 3\pi/8$ , and  $r = 0.1$ . The conductivity inside the elliptical perturbation is  $\sigma_e = 1.0 \text{ S} \cdot \text{m}^{-1}$  and the background conductivity is  $\sigma_0 = 0.33 \text{ S} \cdot \text{m}^{-1}$ .

Case 2a. *Head model*. A classical head model is commonly used in the literature. This model is built of three concentric circles/spheres representing brain, skull, and scalp. Here, we consider the two-dimensional model (see Figure 2.4). This three-layer head model represents the brain  $\Omega_1$ , the skull  $\Omega_2$ , and the scalp  $\Omega_3$  with respective radii 1, 0.9, and 0.87. The adopted

conductivities are  $0.33 \text{ S} \cdot \text{m}^{-1}$  for the brain and the scalp, and  $0.004 \text{ S} \cdot \text{m}^{-1}$  for the skull.

Case 2b. *Head model with one circular inclusion.* We consider the head model in Case 2a but we add a disk inclusion with general equation,

$$(x - h)^2 + (y - k)^2 = r^2,$$

inside the brain region. We fix the center  $(h, k) = (0.4, 0)$ , and the radius  $r = 0.1$  with conductivity  $1.0 \text{ S} \cdot \text{m}^{-1}$ .

Case 3a. *Thorax.* The CT scan of a thorax domain is obtained from [VN17]. Solving the forward problem using the finite element method requires the parametrization of the boundaries of the lungs, the heart, and the whole body. These parametric curves are approximated using Fourier series. The coefficients of the Fourier series are estimated by finding the parametric curve that fits the data points on the boundary curve. With this, any practical domain or object may be studied for real-life applications of EIT. The background conductivity modeling the blood is set to  $0.67 \text{ S} \cdot \text{m}^{-1}$ . The conductivities of the lungs and the heart are respectively fixed to  $0.09 \text{ S} \cdot \text{m}^{-1}$  and  $0.4 \text{ S} \cdot \text{m}^{-1}$  [MPH06].

Case 3b. *Thorax with one circular inclusion.* A disk inclusion with center  $(h, k) = (2.62, 2.25)$ , and  $r = 0.1$  is incorporated in the thorax domain. The said inclusion could model a breast tumor and its conductivity is equal to  $0.2 \text{ S} \cdot \text{m}^{-1}$ .

### 2.4.1 The continuum forward problem

As mentioned, the forward problem gives the synthetic data needed for the reconstruction of the conductivity in the inverse part of EIT. We solve the forward problem numerically for each domain case by solving the system of equations (2.19). All simulations are executed with the software FreeFem++ [Hec12]. The description of the FEM mesh structure used for each case is presented in Table 2.8.

	Nodes	Triangle Elements	$h_{\min}$	$h_{\max}$
Cases 1a-1b	8 992	17 662	0.013	0.038
Cases 2a-2b	8 989	17 676	0.013	0.038
Cases 3a-3b	9 386	18 450	0.008	0.043

TABLE 2.8: FEM mesh structure

Figure 2.5 exhibits the injected current on the boundary. Numerical computations are done for each domain case described in the previous section and the potential solutions are reported in Figure 2.6. The potential in the domain follows the form of the current injected given in Figure 2.5 except in Case 2.

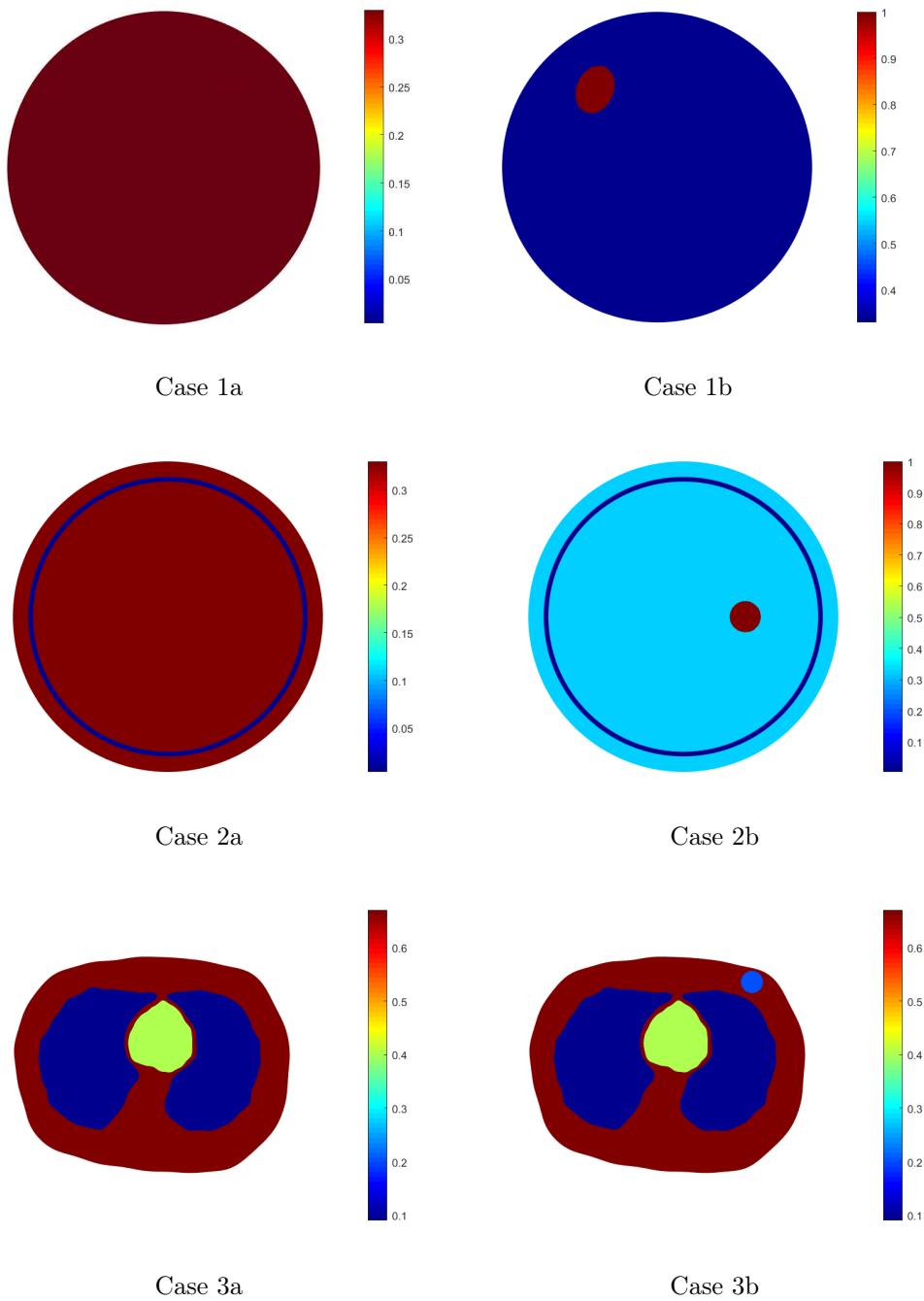


FIGURE 2.4: Conductivity distribution for the different configurations studied in this thesis.

This can be attributed to the effect of the skull with a very low conductivity value. The adult skull is extremely resistive compared to the other tissues and acts as an electrical shield between the scalp and the brain. Notice that the values of the potential are very high in the skull and scalp regions.

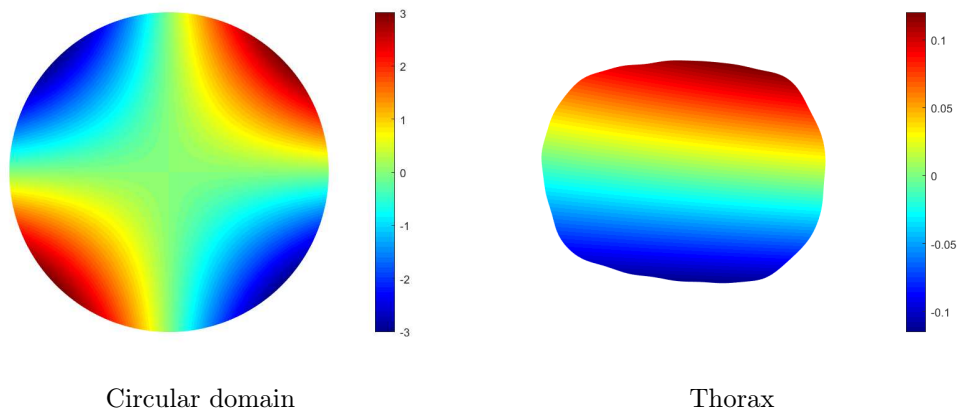


FIGURE 2.5: Continuum model. Left: Injected current density  $f$  for Cases 1a, 1b, 2a, and 2b. Right: Injected current density  $f$  for Cases 3a and 3b.

## 2.4.2 The CEM forward problem

We solve the forward problem numerically for each domain case by solving the system of equations (2.30). The number of electrodes attached around the boundary of the studied domain  $\Omega$  is set to  $L = 32$  (see Figure 2.7). We note that for the disk domain, the midpoint of the first electrode is located on the positive side of the  $x$ -axis and the next ones will follow in a counter-clockwise direction. Meanwhile for the thorax domain, the first electrode's midpoint is defined on the negative side of the  $x$ -axis and the next electrodes will also follow the counter-clockwise direction.

The contact impedance  $Z = (z_\ell)_\ell$  is constant across all electrodes and it is equal to  $z = 0.1$ . The current pattern  $I = (I_\ell)_\ell$  is defined by

$$I_\ell = \sin\left(\frac{2\pi\ell}{L}\right), \quad \ell = 0, 1, 2, \dots, L-1. \quad (2.32)$$

In order to impose the conservation of charge in real-life systems, when a current is injected through one electrode, its corresponding negative measure is injected through the opposite electrode. The sine function satisfies this requirement in 2D set-up and [SCI92] discussed in detail this choice of current pattern. All simulations are executed with the software FreeFem++ [Hec12]. The same FEM mesh structures as described in Table 2.8 are used.

Figure 2.8 shows the interior potentials for each given conductivity distribution described in Figure 2.4. We again observe the difference between the values of the potential for Cases 1a and 1b, and for Cases 2a and 2b. For all the cases, the potential in the domain follows the form of the injected current, sine function, which explains why we have two poles: a positive one and a negative one. Note again that for the disk domain, the first 16 electrodes, which have midpoints in the interval  $[0, \pi]$ , are located in the upper semi-circle which explains the positive potentials in that area and negative ones in the lower semi-circle. On the other hand, for the thorax domain, the first 16 electrodes are located in

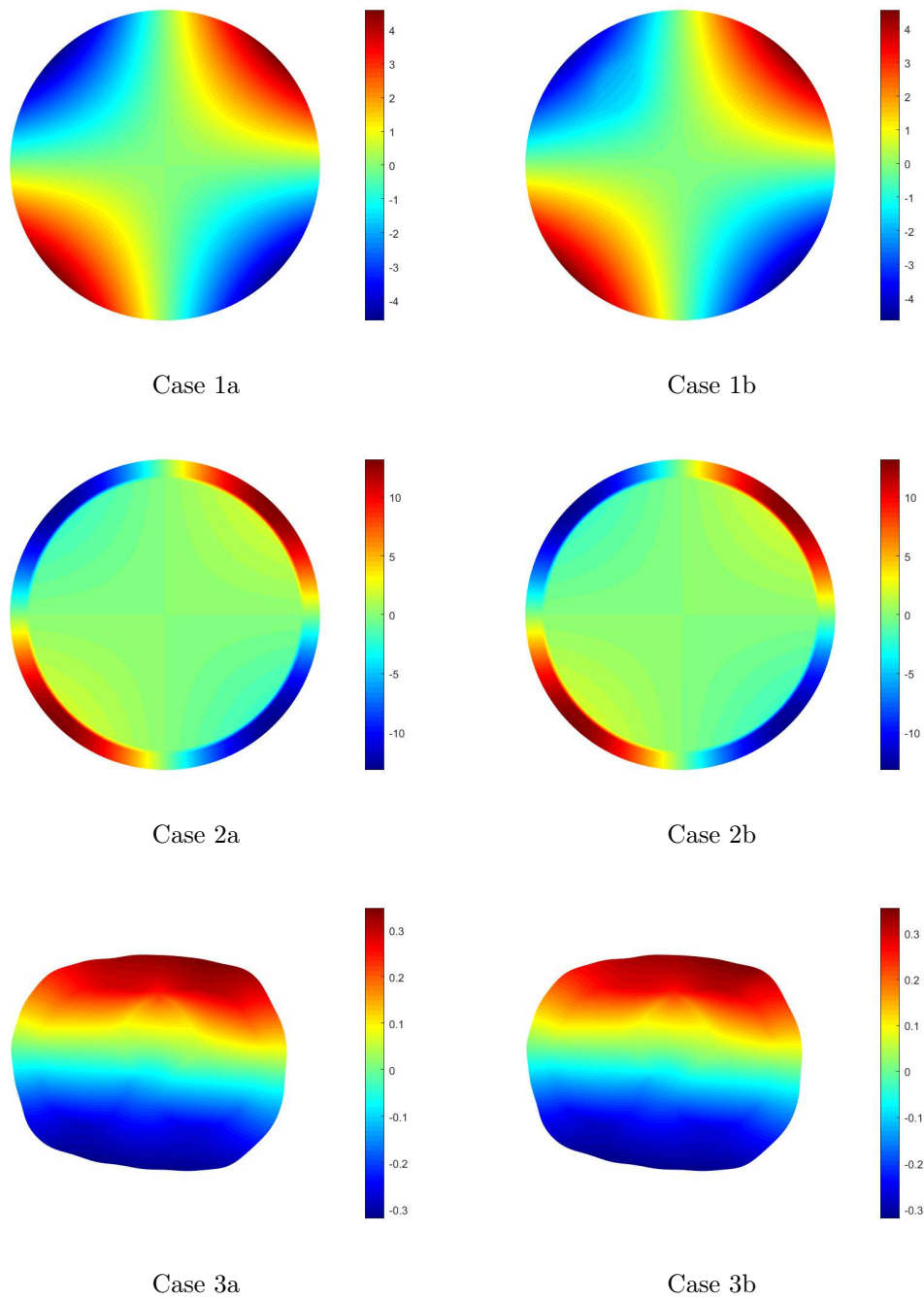


FIGURE 2.6: Potential solutions  $u_h$  of the continuum forward model for each considered domain.

the lower part of the thorax which justifies the positive values of the potential in that area and negative ones in the upper part.

Observe that we hardly see the difference between the values of the interior potential  $u_h$  with an inclusion (Cases b) and without (Cases a). Let  $(u, U)$  be the solution to the CEM forward problem with homogeneous conductivity

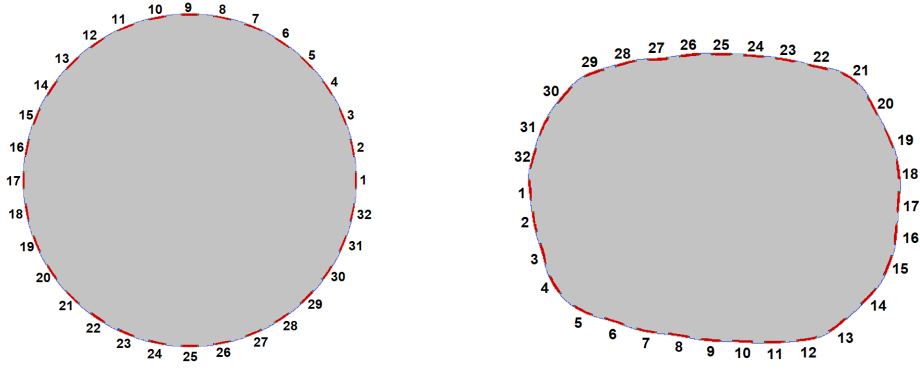


FIGURE 2.7: Location of the electrodes

distribution, that is,

$$\sigma = \sum_{i=0}^n \sigma_i \chi_i,$$

where  $\chi_i$  is the characteristic function of a fixed geometry  $\Omega_i$ , with known conductivity, in the domain  $\Omega$ . Suppose also  $(u_p, U_p)$  is the solution of the perturbed CEM forward problem, that is, the conductivity distribution is given by

$$\sigma_p = \sum_{i=0}^n \sigma_i \chi_i + \sigma_e \chi_e,$$

where  $\sigma_e$  is the value of the conductivity inside the inclusion  $\Omega_e$  with characteristic function  $\chi_e$ . We then compute the difference of the two solutions (Cases 1a and 1b, Cases 2a and 2b, and Cases 3a and 3b). We also obtain the difference between the interior potential values of a homogeneous disk (Case 1a) and disk with 2 elliptical inclusions (Case 4). The numerical approximations of the interior potential  $u_p - u$  are displayed in Figures 2.9 and 2.12.

For each case, the impact of the inclusion is visible. This means that the interior potential  $u_p - u$  contains information on the perturbations. This property may be useful for the numerical resolution of the associated inverse problem. Recall that the data of the EIT inverse problem are the values of the voltage  $U$  at the electrodes. Thus, it seems interesting to identify them at the different electrodes, particularly those close to the inclusion and those far from it.

We reported in Tables 2.9, 2.10, 2.11, and 2.12 the boundary voltages on some electrodes for Cases 1, 2, 3, and 4, respectively. The more significant changes of voltage values are recorded at the electrodes which are near the inclusion. Only some electrodes measure the effect of the inclusion. This is more marked for Cases 1, 3, and 4 than for Case 2. Here again, the skull with a very small conductivity plays a role and retains information which is available for EIT inversion. We observe that adding more perturbation (Case 4 - two ellipses), we retrieve highest values of the voltages at the electrodes near to each inhomogeneity.

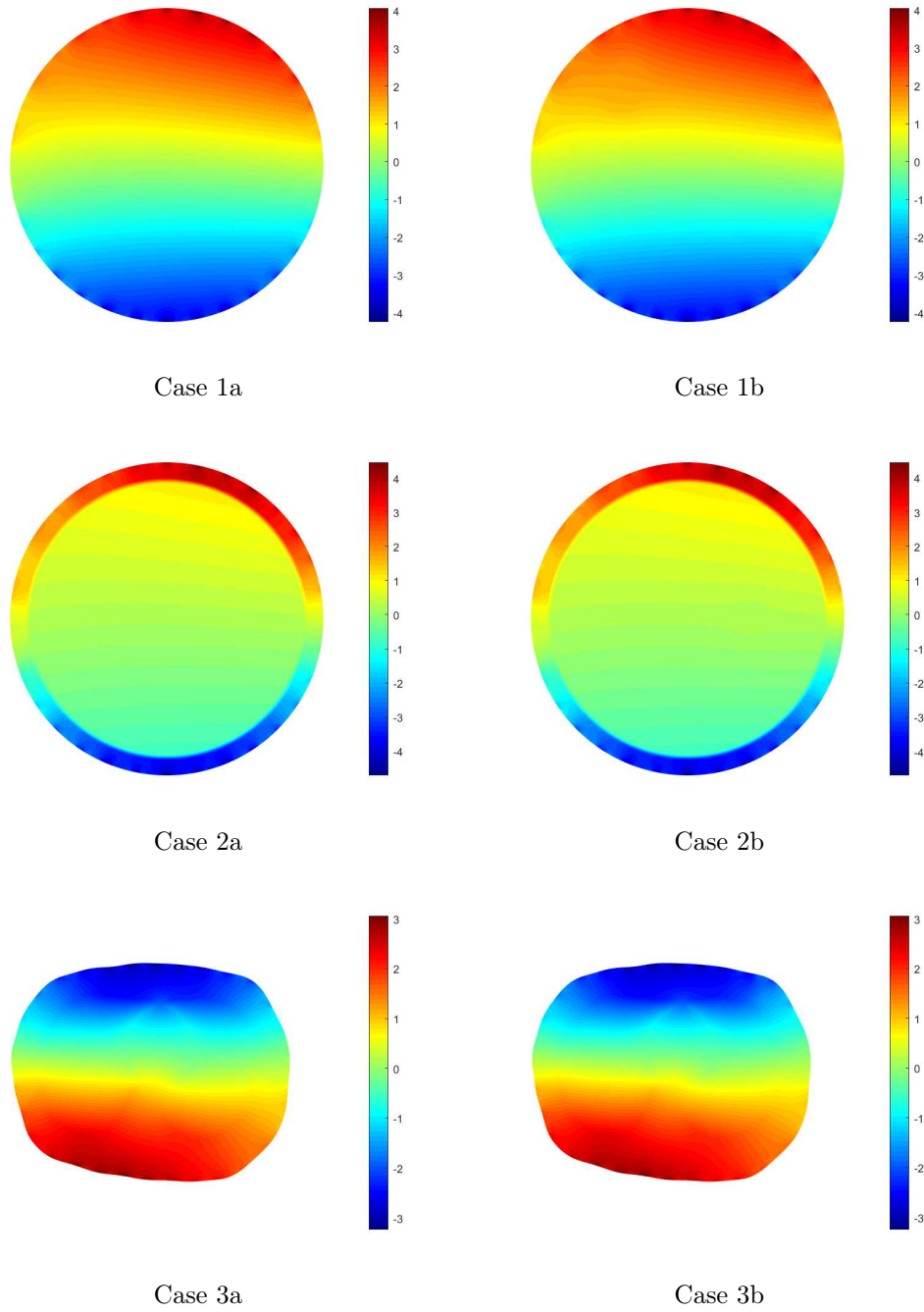
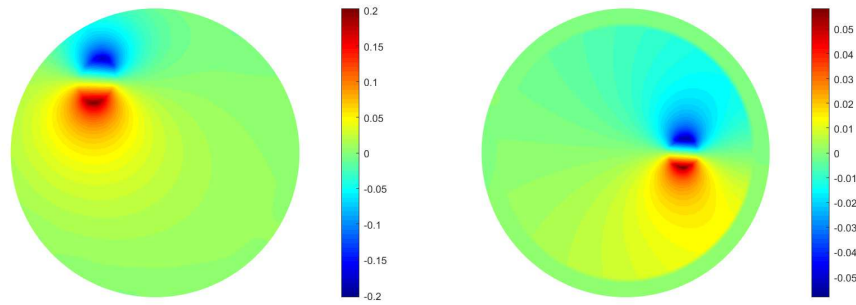


FIGURE 2.8: Approximated interior potentials  $u_h$  of the complete electrode forward model for each considered domain.



Case 1 -Unit disk

Case 2 -Head model

FIGURE 2.9: CEM: perturbed interior potential ( $u_p - u$ ) for each considered domain.

Case 1 - Unit disk			
Electrode	$U$	$U_p$	$U_p - U$
3	2.6471	2.6472	0.0001
12	3.0959	3.0555	-0.0404
18	-0.2220	-0.2076	0.0144
24	-4.8217	-4.8224	-0.0007

TABLE 2.9: CEM Case 1: Values of the voltages at selected electrodes

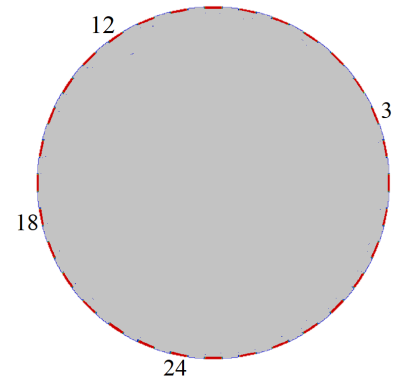


FIGURE 2.10: CEM Case 1: Location of electrodes

Case 2 - Head model			
Electrode	$U$	$U_p$	$U_p - U$
4	3.9555	3.9541	-0.0014
13	2.2224	2.2224	0.0000
17	0.6954	0.6953	-0.0000
30	-4.1582	-4.1570	0.0012

TABLE 2.10: CEM Case 2: Values of the voltages at selected electrodes

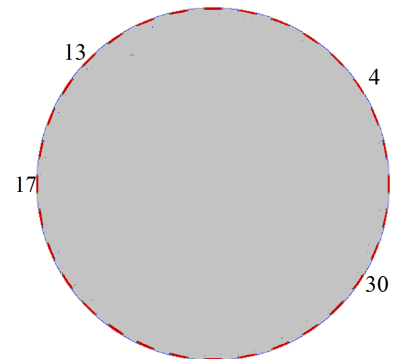


FIGURE 2.11: CEM Case 2: Location of electrodes

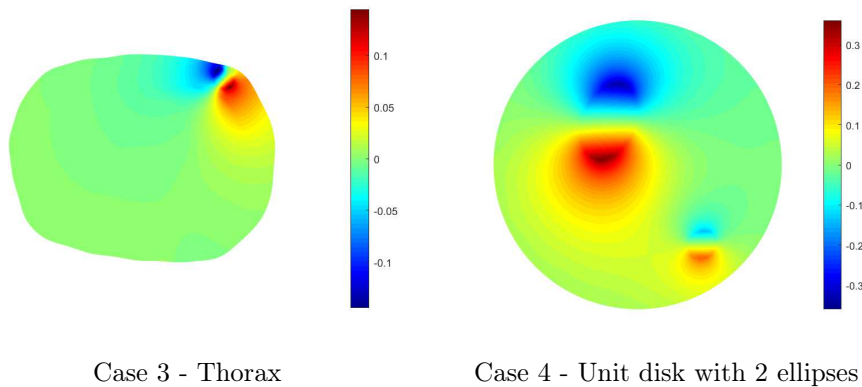


FIGURE 2.12: CEM: perturbed interior potential ( $u_p - u$ ) for each considered domain.

Case 3 - Thorax			
Electrode	$U$	$U_p$	$U_p - U$
6	3.6855	3.6867	0.0011
20	-1.9436	-1.8854	0.0582
22	-3.0368	-3.1417	-0.1049
27	-3.6870	-3.6920	-0.0050

TABLE 2.11: CEM Case 3: Values of the voltages at selected electrodes

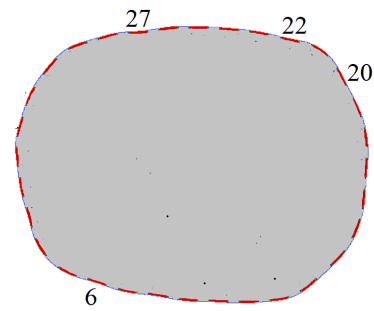


FIGURE 2.13: CEM Case 3: Location of electrodes

Case 4 - Disk with two ellipses			
Electrode	$U$	$U_p$	$U_p - U$
5	3.9818	3.9481	-0.0337
10	4.1257	4.0687	-0.0571
21	-3.4233	-3.3972	0.0261
30	-2.6716	-2.6660	0.0056

TABLE 2.12: CEM Case 4: Values of the voltages at selected electrodes

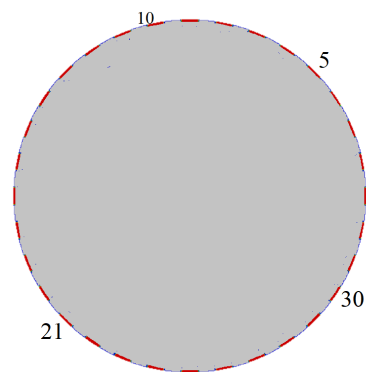


FIGURE 2.14: CEM Case 4: Location of electrodes

## 2.5 Conclusion

In this chapter, we have presented existence and uniqueness results for both the continuum model and the complete electrode model. We then applied the FEM to the corresponding variational problems. Numerical validation has been carried out in the case of an homogeneous conductivity distribution. The error has been computed in the  $L^2$  norm and the  $H^1$  norm in the interior computational domain for different meshes, and in the Euclidean norm for the voltages on the boundary. The numerical convergence rates coincide with the theoretical results. We have provided several numerical simulations for different configurations that we will consider in the succeeding chapters. Lastly, we have numerically observed the impact of an inclusion in a background medium on the values of the electric potential in the domain under inspection and at the surface electrodes (which are the data of the EIT inverse problem). This provides an insight about the surface electrodes on which the electrical potential is affected by variations in the conductivity of the medium. It would seem that the perturbed potential contains information on the characteristics of the inclusion. We investigate more of this property in the next chapter and we also propose a rigorous sensitivity analysis of the potential with respect to small variations of the conductivity or of the contact impedance of the electrodes.

## Chapter 3

# Sensitivity analysis of the electric potential in Complete Electrode Model

In this chapter, we introduce an analysis tool to investigate the sensitivity of the electric potential with respect to the variations in the conductivity and in the contact impedance of electrodes. From a mathematical point of view, sensitivity is the directional derivative of the solution with respect to conductivity and to contact impedance. We prove that the electrical potential, solution to the CEM forward problem, is Gâteaux differentiable at  $\sigma$  and at  $Z$  and we express its respective derivative. Numerical results illustrate this concept.

### 3.1 Introduction and notations

The EIT forward problem gives the potential distribution in  $\Omega$  which are the data of the inverse conductivity problem. With this, knowing the effect of some parameters such as the conductivity distribution and the electrode contact impedance on the forward solution might provide us an information needed for the reconstruction problem. The study of how the input perturbations of a mathematical model influence the variability of its output is called sensitivity analysis. Sensitivity indicates the behavior of the potential when there is a slight variation of physical parameters. There are two approaches: global and local sensitivity analysis. The global sensitivity analysis focuses on how the input parameters, as a whole, influence the variance output, and it usually uses statistical tools and methods such as Sobol indices and Monte Carlo estimation [Mor11]. Meanwhile, local sensitivity analyses how a small perturbation near an input space value influences the output, and it is usually derivative-based [Mor11; Dia17].

In this chapter, we focus on the local sensitivity analysis of the electric potential in the CEM forward problem. In particular, we are interested in the sensitivity with respect to the conductivity and with respect to the contact impedance of electrodes. This allows to measure the effect of uncertainty in both conductivity and contact impedance values on the CEM forward model. This also permits to understand the impact of possible perturbations of the conductivity (e.g. tumors or strokes in medical applications) or small electrode

defects on the potential measurements. Mathematically, a rigorous way to describe sensitivity is given by Gâteaux differentiability which expresses a weak concept of derivative.

**Definition 3.1.1** (Gâteaux derivative). Let  $w : X \rightarrow Y$  be an application between two Banach spaces  $X$  and  $Y$ . Let  $O \subset X$  be an open set. The directional derivative  $D_\mu w(p)$  of  $w$  at  $p \in O$  in the direction  $\mu \in X$  is defined by

$$D_\mu w(p) = \lim_{h \rightarrow 0} \frac{w(p + \mu h) - w(p)}{h}$$

if the limit exists. If  $D_\mu w(p)$  exists for any direction  $\mu \in X$  and if the map  $\mu \mapsto D_\mu w(p)$  is linear continuous from  $X$  to  $Y$ ,  $w$  is called Gâteaux differentiable at  $p$ .

## 3.2 Sensitivity analysis of the electric potential with respect to the conductivity

Let  $I = (I_1, \dots, I_L)^T \in \mathbb{R}^L$  be a fixed current pattern and  $Z = (z_1, \dots, z_L)^L \in \mathbb{R}^L$  be fixed positive contact impedance values. Let the set of admissible conductivities  $\mathcal{P}_{\text{adm}}$  be defined as in Definition 1.2.1, that is,

$$\mathcal{P}_{\text{adm}} = \{\sigma \text{ such that } \sigma|_{\Omega_j} \in C(\overline{\Omega_j}), 1 \leq j \leq N \text{ and } \sigma_{\min} \leq \sigma(\mathbf{x}) \leq \sigma_{\max}, \mathbf{x} \in \Omega\}.$$

Denote  $B_\sigma$  to be the map from the conductivity  $\sigma$  to the bilinear operator  $B$  in (2.10), that is,  $\sigma \mapsto B(\cdot, \cdot)$ . We set  $(u, U) := (u(\cdot, \sigma), U(\sigma))$  as the solution of the variational formulation

$$B_\sigma((u, U), (w, W)) = \sum_{\ell=1}^L I_\ell W_\ell, \quad (3.1)$$

where  $B_\sigma((u, U), (w, W)) = \int_{\Omega} \sigma \nabla u \cdot \nabla w \, d\mathbf{x} + \sum_{\ell=1}^L \frac{1}{z_\ell} \int_{e_\ell} (u - U_\ell)(w - W_\ell) \, ds$ . We

have proven in Section 2.1.2 that the variational problem (3.1) with conductivity  $\sigma \in \mathcal{P}_{\text{adm}}$  admits a unique solution  $(u, U) \in H_\diamond$ . The aim is to prove differentiability of  $(u, U)$  with respect to  $\sigma$  and to identify its derivative in a given direction  $\mu$ . We consider a direction  $\mu \in L^\infty(\Omega)$  with  $\|\mu\|_\infty = 1$  such that  $\sigma + h\mu \in \mathcal{P}_{\text{adm}}$  for any  $h \in [-h_0, h_0]$ ,  $h_0 > 0$ . We set  $(u^h, U^h) := (u(\cdot, \sigma + h\mu), U(\sigma + h\mu)) \in H_\diamond$  the solution of the perturbed CEM forward problem with conductivity  $\sigma + h\mu$ . The associated variational formulation reads: find  $(u^h, U^h) \in H_\diamond$  such that

$$B_{\sigma+h\mu}((u^h, U^h), (w, W)) = \sum_{\ell=1}^L I_\ell W_\ell, \quad (3.2)$$

for all  $(w, W) \in H_\diamond$ , where the bilinear form is defined by

$$B_{\sigma+h\mu}((u^h, U^h), (w, W)) := \int_{\Omega} (\sigma+h\mu) \nabla u^h \cdot \nabla w \, d\mathbf{x} + \sum_{\ell=1}^L \frac{1}{z_\ell} \int_{e_\ell} (u^h - U_\ell^h)(w - W_\ell) \, ds. \quad (3.3)$$

In the sequel, we write  $a \lesssim b$  if there is a constant  $C > 0$  independent from the quantities  $a$  and  $b$  such that  $a \leq Cb$ . We have the following preliminary lemma for the sensitivity with respect to  $\sigma$ .

**Lemma 3.2.1.** *Let  $\sigma \in \mathcal{P}_{adm}$  and  $h_0 > 0$  such that  $\sigma + h\mu \in \mathcal{P}_{adm}$  for any  $h \in [-h_0, h_0]$  and any  $\mu \in L^\infty(\Omega)$  with  $\|\mu\|_{L^\infty(\Omega)} = 1$ . Let  $(u, U)$  and  $(u^h, U^h)$  as the respective solutions in  $H_\diamond$  of the variational problems (3.1) and (3.2) for all  $(w, W) \in H_\diamond$ . Then, we have the following estimate*

$$\|\nabla(u^h - u)\|_{L^2(\Omega)} \lesssim h \|\mu\|_{L^\infty(\Omega)}.$$

*Proof.* Subtracting (3.1) from (3.2) leads to

$$B_\sigma((u^h - u, U^h - U), (w, W)) = -h \int_{\Omega} \mu \nabla u^h \cdot \nabla w \, d\mathbf{x}, \quad \forall (w, W) \in H_\diamond. \quad (3.4)$$

Taking  $(w, W) = (u^h - u, U^h - U)$ , and using Cauchy-Schwarz inequality, we get

$$|B_\sigma((u^h - u, U^h - U), (u^h - u, U^h - U))| \leq h \|\mu\|_{L^\infty(\Omega)} \|\nabla u^h\|_{L^2(\Omega)} \|\nabla(u^h - u)\|_{L^2(\Omega)}.$$

Furthermore, the coercivity of  $B_\sigma$  on  $H_\diamond$  and (3.4) gives

$$\|(u^h - u, U^h - U)\|_*^2 \lesssim |B_\sigma((u^h - u, U^h - U), (u^h - u, U^h - U))|.$$

By the equivalence of the norms  $\|\cdot\|_{H_\diamond}$  and  $\|\cdot\|_*$  given in Lemma 2.1.3 and Remark 1 (see pp. 14 and 17), we obtain

$$\begin{aligned} \|(u^h - u, U^h - U)\|_*^2 &\lesssim h \|\mu\|_{L^\infty(\Omega)} \|\nabla u^h\|_{L^2(\Omega)} \|\nabla(u^h - u)\|_{L^2(\Omega)} \\ &\lesssim h \|\mu\|_{L^\infty(\Omega)} \|\nabla u^h\|_{L^2(\Omega)} \|(u^h - u, U^h - U)\|_*. \end{aligned}$$

Hence, we get

$$\|(u^h - u, U^h - U)\|_* \lesssim h \|\mu\|_{L^\infty(\Omega)} \|\nabla u^h\|_{L^2(\Omega)}. \quad (3.5)$$

By studying in the same way the variational problem (3.2), we prove that

$$\|\nabla u^h\|_{L^2(\Omega)} \leq C(\sigma_{\min}),$$

with  $C(\sigma_{\min})$  a positive constant independent from  $h$ . Hence, (3.5) reads

$$\|(u^h - u, U^h - U)\|_* \lesssim h \|\mu\|_{L^\infty(\Omega)}$$

and finally, from the definition of (2.9)

$$\|\nabla(u^h - u)\|_{L^2(\Omega)} \lesssim h\|\mu\|_{L^\infty(\Omega)}.$$

□

Now we proceed to the Gâteaux differentiability of the potential given in the following proposition. Its derivative is also expressed in this proposition.

**Proposition 3.2.2.** *Let  $I$  be a fixed current pattern and  $\sigma$  a known conductivity distribution satisfying (2.5). Let  $\sigma \in \mathcal{P}_{adm}$  and  $h_0 > 0$  such that  $\sigma + h\mu \in \mathcal{P}_{adm}$  for any  $h \in [-h_0, h_0]$  and  $\mu \in L^\infty(\Omega)$  with  $\|\mu\|_{L^\infty(\Omega)} = 1$ . Then the solution  $(u(\cdot, \sigma), U(\sigma))$  of (3.1) is Gâteaux differentiable with respect to  $\sigma$ . Moreover, the Gâteaux derivative of  $(u, U)$  in the direction  $\mu \in L^\infty(\Omega)$  is the unique solution of the following variational problem: find  $(u^1, U^1) \in H_\diamond$  such that*

$$B_\sigma((u^1, U^1), (w, W)) = - \int_{\Omega} \mu \nabla u \cdot \nabla w \, d\mathbf{x} \quad (3.6)$$

for all  $(w, W) \in H_\diamond$ .

*Proof.* Let  $(u, U)$  be the solution to the CEM forward problem (1.21)–(1.24) that satisfies the variational formulation (3.1). Also, let  $(u^h, U^h)$  be the solution of the variational formulation (3.2) to the perturbed CEM forward problem. Let us introduce the differential quotients

$$u^{h,1} := \frac{u^h - u}{h} \quad \text{and} \quad U^{h,1} := \frac{U^h - U}{h}.$$

Subtracting (3.1) from (3.2), we have  $\forall (w, W) \in H_\diamond$

$$\begin{aligned} \int_{\Omega} \sigma \nabla(u^h - u) \cdot \nabla w \, d\mathbf{x} + \sum_{\ell=1}^L \frac{1}{z_\ell} \int_{e_\ell} ((u^h - u) - (U_\ell^h - U_\ell)(w - W_\ell)) \, ds \\ + \int_{\Omega} \mu h \nabla u^h \cdot \nabla w \, d\mathbf{x} = 0 \\ B_\sigma((u^h - u, U^h - U), (w, W)) = - \int_{\Omega} \mu h \nabla u^h \cdot \nabla w \, d\mathbf{x}. \end{aligned}$$

Dividing by  $h$  leads to

$$B_\sigma((u^{h,1}, U^{h,1}), (w, W)) \equiv - \int_{\Omega} \mu \nabla u^h \cdot \nabla w \, d\mathbf{x}, \quad \forall (w, W) \in H_\diamond. \quad (3.7)$$

We compare the previous formulation (3.7) with the variational formulation (3.6):

$$B_\sigma((u^{h,1} - u^1, U^{h,1} - U^1), (w, W)) = - \int_{\Omega} \mu \nabla(u^h - u) \cdot \nabla w \, d\mathbf{x}.$$

We take  $(w, W) = (u^{1,h} - u^1, U^{1,h} - U^1)$ . Using the coercivity of  $B_\sigma$  on  $H_\diamond$  and the equivalence of the norms  $\|\cdot\|_{H_\diamond}$  and  $\|\cdot\|_*$  given in Lemma 2.1.3 and Remark

1, we get

$$\begin{aligned} \|(u^{1,h} - u^1, U^{1,h} - U^1)\|_*^2 &\lesssim |B_\sigma((u^{1,h} - u^1, U^{1,h} - U^1), (u^{1,h} - u^1, U^{1,h} - U^1))| \\ &\lesssim \|\mu\|_{L^\infty(\Omega)} \|\nabla(u^h - u)\|_{L^2(\Omega)} \|\nabla(u^{1,h} - u^h)\|_{L^2(\Omega)}. \end{aligned}$$

The definition of the norm  $\|\cdot\|_*$  leads to

$$\begin{aligned} \|(u^{1,h} - u^1, U^{1,h} - U^1)\|_*^2 &\lesssim \|\mu\|_{L^\infty(\Omega)} \|\nabla(u^h - u)\|_{L^2(\Omega)} \|(u^{1,h} - u^1)\|_{H^1(\Omega)} \\ &\lesssim \|\mu\|_{L^\infty(\Omega)} \|\nabla(u^h - u)\|_{L^2(\Omega)} \|(u^{1,h} - u^1, U^{1,h} - U^1)\|_{H_\diamond}. \end{aligned}$$

Hence, we obtain

$$\|(u^{1,h} - u^1, U^{1,h} - U^1)\|_* \lesssim \|\mu\|_{L^\infty(\Omega)} \|\nabla(u^h - u)\|_{L^2(\Omega)}. \quad (3.8)$$

Finally, by Lemma 3.2.1, (3.8) reads

$$\|(u^{1,h} - u^1, U^{1,h} - U^1)\|_* \lesssim h \|\mu\|_{L^\infty(\Omega)}^2.$$

This proves the strong convergence of the sequence  $(u^{1,h}, U^{1,h})_h$  to  $(u^1, U^1)$  in  $H_\diamond$ .

Now it remains to show that the map  $\mu \mapsto (u^1, U^1)$  is linear continuous from  $L^\infty(\Omega)$  to  $H_\diamond$ . For fixed  $\mu$ , the derivative is defined by the solution of (3.6) and the right-hand side of (3.6) is linear in  $\mu$ . The continuity of the linear application  $\mu \mapsto (u^1, U^1)$  follows from the following estimate: taking  $(w, W) = (u^1, U^1)$  in (3.6), we get

$$\begin{aligned} \|(u^1, U^1)\|_*^2 &\lesssim |B_\sigma((u^1, U^1), (u^1, U^1))| \\ &\lesssim \|\mu\|_{L^\infty(\Omega)} \|\nabla u\|_{L^2(\Omega)} \|\nabla u^1\|_{L^2(\Omega)} \\ &\lesssim \|\mu\|_{L^\infty(\Omega)} \|\nabla u\|_{L^2(\Omega)} \|(u^1, U^1)\|_*. \end{aligned}$$

Since  $u \in H^1(\Omega)$ , we have

$$\|(u^1, U^1)\|_* \lesssim \|\mu\|_{L^\infty(\Omega)}.$$

This yields the continuity of the directional derivative with respect to  $\mu$  and proves that  $(u(\cdot, \sigma), U(\sigma))$  is Gâteaux differentiable with respect to the conductivity  $\sigma$ .  $\square$

### 3.2.1 Discretization of the sensitivity equation with respect to the conductivity

The derivative  $(u^1, U^1)$  of the potential  $(u, U)$  with respect to the conductivity  $\sigma$  in the direction  $\mu$  is the solution of the following boundary value problem

$$\begin{aligned}
-\nabla \cdot (\sigma \nabla u^1) &= \nabla \cdot (\mu \nabla u) && \text{in } \Omega, \\
u^1 + z_\ell \sigma \partial_{\bar{n}} u^1 &= -z_\ell \mu \partial_{\bar{n}} u + U_\ell^1 && \text{on } e_\ell, \ell = 1, \dots, L, \\
\int_{e_\ell} \sigma \partial_{\bar{n}} u^1 ds &= - \int_{e_\ell} \mu \partial_{\bar{n}} u ds && \ell = 1, \dots, L, \\
\sigma \partial_{\bar{n}} u^1 &= -\mu \partial_{\bar{n}} u && \text{on } \partial\Omega \setminus \Gamma_e,
\end{aligned} \tag{3.9}$$

where  $u$  is the solution of the unperturbed problem, i.e. satisfies  $\nabla \cdot (\sigma \nabla u) = 0$ . Formally, consider a perturbation of  $\sigma$  of the form  $\sigma + \mu h$  for fixed  $\mu$ . The potential  $u^h$  is solution of the perturbed equation  $\nabla \cdot ((\sigma + \mu h) \nabla u) = 0$ . Subtracting the above equations and dividing by  $h$  yields

$$-\nabla \cdot \left( \sigma \nabla \left( \frac{u^h - u}{h} \right) \right) = \nabla \cdot (\mu \nabla u).$$

At the limit  $h \rightarrow 0$ , we get that the sensitivity  $u^1$  satisfies the first equation of (3.9). The different boundary equations can be obtained in a similar way. The variational formulation of the problem (3.9) is given by (3.6).

We consider a triangular mesh  $\mathcal{T}_h$  for 2D geometries  $\Omega$  and on  $\mathcal{T}_h$ , we introduce  $X_h$  the standard vector space of Lagrange finite elements of type P1 and  $\mathcal{B}_h$  the set of basis functions in  $X_h$ . The approximation  $u_h \in X_h$  of the electric potential  $u$ , solution to the CEM forward problem, is given by (2.20). The approximation  $u_h^1$  of the sensitivity  $u^1$  is defined by

$$u_h^1(\mathbf{x}) = \sum_{j=1}^N v_j^1 \varphi_j(\mathbf{x}) \tag{3.10}$$

where  $v_j^1$  is the approximated value of  $u^1$  at the  $j$ th node. Here again, to ensure that the potential  $U^1$  satisfy the condition (2.6), we search the approximation  $U_h^1$  of  $U^1$  under the form

$$U_h^1 = \sum_{k=1}^{L-1} \beta_k^1 \phi_k, \tag{3.11}$$

with  $U_h^1 = P\beta^1$  and  $\beta^1 = (\beta_k^1)^T \in \mathbb{R}^{L-1}$  (see (2.22)).

We set the test functions  $(w, W) = (\varphi_i, \mathbf{0})$ . We substitute (2.20) and (3.10) to (3.6), and we get for  $i = 1, \dots, N$

$$\begin{aligned} \sum_{j=1}^N v_j^1 \int_{\Omega} \sigma \nabla \varphi_j \cdot \nabla \varphi_i \, d\mathbf{x} + \sum_{\ell=1}^L \frac{1}{z_{\ell}} \int_{e_{\ell}} \left( \sum_{j=1}^N v_j^1 \varphi_j - \sum_{k=1}^{L-1} \beta_k^1 \phi_k \right) \varphi_i \, ds \\ = - \sum_{j=1}^N v_j \int_{\Omega} \mu \nabla \varphi_j \cdot \nabla \varphi_i \, d\mathbf{x}, \end{aligned} \quad (3.12)$$

where  $v = (v_j)_{j=1}^N$  represent the degrees of freedom of the solution  $u$  of the unperturbed CEM (1.21)-(1.22)-(1.23)-(1.24). Furthermore, from the boundary conditions in (3.9), we deduce

$$\frac{1}{z_{\ell}} \int_{e_{\ell}} (U_{\ell}^1 - u^1) \, ds = 0, \quad \ell = 1, 2, \dots, L. \quad (3.13)$$

We use the same method which is presented previously in Section 2.2.3 to treat (2.27). Finally, we obtain the following linear system of size  $N + L - 1$

$$\begin{bmatrix} S + M & C \\ C^T & G \end{bmatrix} \begin{bmatrix} v^1 \\ \beta^1 \end{bmatrix} = \begin{bmatrix} Fv \\ \mathbf{0}_{\mathbb{R}^{L-1}} \end{bmatrix}, \quad (3.14)$$

where matrices  $S$ ,  $M$ ,  $C$ , and  $G$  are defined by (2.24), (2.25), (2.26), and (2.29), respectively,  $v^1 = (v_j^1)_{j=1}^N$ ,  $F = (F_{ij}) \in \mathbb{R}^{N \times N}$  with coefficients  $F_{ij} = - \int_{\Omega} \mu \nabla \varphi_j \cdot \nabla \varphi_i \, d\mathbf{x}$ . The vector  $v$  is computed using the resolution of the linear system (2.30).

### 3.3 Sensitivity analysis of CEM with respect to the contact impedance

Let the set of admissible values of the contact impedance vector be

$$\mathcal{Z}_{\text{adm}} := \{Z \in \mathbb{R}^L \mid z_{\min} < z_{\ell} < z_{\max}\},$$

with  $0 < z_{\min} \leq z_{\max} < +\infty$ . Let  $I = (I_1, \dots, I_L)^T \in \mathbb{R}_{\diamond}^L$  be a fixed current pattern and  $\sigma$  be a fixed conductivity distribution in  $\Omega$ . Denote  $B_Z$  to be the map from the contact impedance vector  $Z$  to the bilinear operator  $B$  in (2.10), i.e.,  $Z \mapsto B(\cdot, \cdot)$ . We set  $(u, U) := (u(\cdot, Z), U(Z))$  as the solution of the variational formulation

$$B_Z((u, U), (w, W)) = \sum_{\ell=1}^L I_{\ell} W_{\ell}, \quad (3.15)$$

where the bilinear operator is defined as

$$B_Z((u, U), (w, W)) := \int_{\Omega} \sigma \nabla u \cdot \nabla w \, dx + \sum_{\ell=1}^L \frac{1}{z_{\ell}} \int_{e_{\ell}} (u - U_{\ell})(w - W_{\ell}) \, ds. \quad (3.16)$$

Note that the bilinear forms  $B_{\sigma}$  and  $B_Z$  coincide and that problem (3.15) with contact impedance  $Z \in \mathcal{Z}_{\text{adm}}$  admits a unique solution  $(u, U) \in H_{\diamond}$ . We want to prove the differentiability of  $(u, U)$  with respect to  $Z$  and to identify its derivative in a given direction  $\eta$ . We consider a direction  $\eta \in \mathbb{R}^L$  such that  $\tilde{Z} := Z + \eta h \in \mathcal{Z}_{\text{adm}}$  for any  $h \in [-h_0, h_0]$ ,  $h_0 > 0$ . We set  $(\tilde{u}^h, \tilde{U}^h) := (u(\cdot, \tilde{Z}), U(\tilde{Z})) \in H_{\diamond}$  as the solution of the perturbed CEM forward problem with contact impedance  $\tilde{Z}$ . The associated variational formulation reads: find  $(\tilde{u}^h, \tilde{U}^h) \in H_{\diamond}$  such that

$$B_{\tilde{Z}}((\tilde{u}^h, \tilde{U}^h), (w, W)) = \sum_{\ell=1}^L I_{\ell} W_{\ell} \quad (3.17)$$

for all  $(w, W) \in H_{\diamond}$ , where the bilinear form is defined by

$$B_{\tilde{Z}}((\tilde{u}^h, \tilde{U}^h), (w, W)) := \int_{\Omega} \sigma \nabla \tilde{u}^h \cdot \nabla w \, dx + \sum_{\ell=1}^L \frac{1}{z_{\ell} + \eta_{\ell} h} \int_{e_{\ell}} (\tilde{u}^h - \tilde{U}_{\ell}^h)(w - W_{\ell}) \, ds. \quad (3.18)$$

**Proposition 3.3.1.** *Let  $I$  be a fixed current pattern and  $\sigma$  a known conductivity distribution satisfying (2.5). Let  $Z \in \mathcal{Z}_{\text{adm}}$  such that  $Z + \eta h \in \mathcal{Z}_{\text{adm}}$  for any  $h \in [-h_0, h_0]$  and  $\eta \in \mathbb{R}^L$ . Then the solution  $(u, U)$  of (3.15) is Gâteaux differentiable with respect to  $Z$ . Furthermore, its Gâteaux derivative in the direction  $\eta$  is the unique solution of the following variational problem: find  $(u^2, U^2) \in H_{\diamond}$  such that*

$$B_Z((u^2, U^2), (w, W)) = \sum_{\ell=1}^L \frac{\eta_{\ell}}{z_{\ell}^2} \int_{e_{\ell}} (u - U_{\ell})(w - W_{\ell}) \, ds \quad (3.19)$$

for all  $(w, W) \in H_{\diamond}$ .

*Proof.* Let  $(u, U)$  be the solution in  $H_{\diamond}$  of the variational problem (3.15). Assume that  $(\tilde{u}^h, \tilde{U}^h)$  is the solution in  $H_{\diamond}$  of the perturbed CEM forward problem with contact impedance  $\tilde{Z}$ .

Subtracting (3.15) from (3.17) and dividing by  $h$ , we have

$$\begin{aligned} \int_{\Omega} \sigma \nabla \left( \frac{\tilde{u}^h - u}{h} \right) \cdot \nabla w \, dx &+ \sum_{\ell=1}^L \int_{e_{\ell}} \left( \frac{1}{h} \left( \frac{\tilde{u}^h}{z_{\ell} + h\eta_{\ell}} - \frac{u}{z_{\ell}} \right) \right. \\ &\left. - \frac{1}{h} \left( \frac{\tilde{U}_{\ell}^h}{z_{\ell} + h\eta_{\ell}} - \frac{U_{\ell}}{z_{\ell}} \right) \right) (w - W_{\ell}) \, ds = 0. \end{aligned} \quad (3.20)$$

A Taylor expansion yields

$$\frac{1}{z_\ell + h\eta_\ell} = \frac{1}{z_\ell} - h \frac{\eta_\ell}{z_\ell^2} + \mathcal{O}(h^2),$$

from which we deduce

$$\frac{1}{h} \left( \frac{\tilde{u}^h}{z_\ell + h\eta_\ell} - \frac{u}{z_\ell} \right) = \frac{1}{z_\ell} \frac{\tilde{u}^h - u}{h} - \frac{\eta_\ell}{z_\ell^2} \tilde{u}^h + \mathcal{O}(h).$$

Thus, the differential quotients defined by

$$u^{h,2} := \frac{\tilde{u}^h - u}{h} \text{ and } U^{h,2} := \frac{\tilde{U}^h - U}{h}$$

satisfy the variational formulation

$$B_Z((u^{h,2}, U^{h,2}), (w, W)) = \sum_{\ell=1}^L \frac{\eta_\ell}{z_\ell^2} \int_{e_\ell} (\tilde{u}^h - \tilde{U}_\ell^h)(w - W_\ell) ds + \mathcal{O}(h) \quad (3.21)$$

for all  $(w, W) \in H_\diamond$ . Furthermore, suppose  $(u^2, U^2) \in H_\diamond$  is the solution to the variational problem (3.19) for all  $(w, W) \in H_\diamond$ . Next, subtracting (3.19) from (3.21), we obtain

$$B_Z((u^{h,2} - u^2, U^{h,2} - U^2), (w, W)) = \sum_{\ell=1}^L \frac{\eta_\ell}{z_\ell^2} \int_{e_\ell} [(\tilde{u}^h - u) - (\tilde{U}_\ell^h - U_\ell)](w - W_\ell) ds + \mathcal{O}(h). \quad (3.22)$$

Now we show that  $u^{2,h}$  strongly converges to  $u^2$  as  $h \rightarrow 0$ . Take  $(w, W) = (u^{h,2} - u^2, U^{h,2} - U^2)$ . From the continuity and coercivity of the bilinear operator  $B_Z$ , and using the equivalence of norms, we get

$$\begin{aligned} \|(u^{2,h} - u^2, U^{2,h} - U^2)\|_*^2 &\lesssim |B_Z((u^{2,h} - u^2, U^{2,h} - U^2), (u^{2,h} - u^2, U^{2,h} - U^2))| \\ &\lesssim \sum_{\ell=1}^L \left| \frac{\eta_\ell}{z_\ell^2} \int_{e_\ell} [(\tilde{u}^h - u) - (\tilde{U}_\ell^h - U_\ell)] \right. \\ &\quad \left. \dots [(u^{2,h} - u^2) - (U_\ell^{2,h} - U_\ell^2)] \right| ds + \mathcal{O}(h) \\ &\lesssim \|\eta\|_{L^\infty(\Omega)} \|(\tilde{u}^h - u, \tilde{U}^h - U)\|_* \|(u^{2,h} - u^2, U^{2,h} - U^2)\|_* + \mathcal{O}(h), \end{aligned}$$

where  $\|\eta\|_\infty := \max_{1 \leq \ell \leq L} |\eta_\ell|$ . Thus, we have

$$\|(u^{h,2} - u^2, U^{h,2} - U^2)\|_* \lesssim \|\eta\|_\infty \|(\tilde{u}^h - u, \tilde{U}^h - U)\|_* + \mathcal{O}(h). \quad (3.23)$$

Using the same arguments as previously and taking  $(w, W) = (\tilde{u}^h - u, \tilde{U}^h - U)$  in (3.20), we get

$$\begin{aligned} \|(\tilde{u}^h - u, \tilde{U}^h - U)\|_*^2 &\lesssim \left| B_Z((\tilde{u}^h - u, \tilde{U}^h - U), (\tilde{u}^h - u, \tilde{U}^h - U)) \right| \\ &\lesssim h \sum_{\ell=1}^L \frac{\eta_\ell}{z_\ell^2} \int_{e_\ell} \left| (\tilde{u}^h - \tilde{U}_\ell^h)[(\tilde{u}^h - u) - (\tilde{U}_\ell^h - U_\ell)] \right| ds + \mathcal{O}(h^2) \\ &\lesssim h \|\eta\|_{L^\infty(\Omega)} \|(\tilde{u}^h, \tilde{U}^h)\|_* \|(\tilde{u}^h - u, \tilde{U}^h - U)\|_* + \mathcal{O}(h^2). \end{aligned}$$

Hence, we obtain

$$\|(\tilde{u}^h - u, \tilde{U}^h - U)\|_* \lesssim h \|\eta\|_{L^\infty(\Omega)} \|(\tilde{u}^h, \tilde{U}^h)\|_* + \mathcal{O}(h^2).$$

Since  $(\tilde{u}^h, \tilde{U}^h) \in H_\diamond$  satisfies (3.17), and  $\|(\tilde{u}^h, \tilde{U}^h)\|_*$  is bounded independently from  $h$ , we deduce

$$\|(\tilde{u}^h - u, \tilde{U}^h - U)\|_* \lesssim h \|\eta\|_{L^\infty(\Omega)} + \mathcal{O}(h^2).$$

Finally, (3.23) leads to

$$\|(\tilde{u}^{h,2} - u^2, \tilde{U}^{h,2} - U^2)\|_* \lesssim h \|\eta\|_\infty^2 + \mathcal{O}(h^2).$$

This proves the strong convergence of  $(\tilde{u}^{h,2}, \tilde{U}^{h,2})_h$  to  $(u^2, U^2)$ .

Lastly we prove that the map  $\eta \mapsto (u^2, U^2)$  is linear continuous from  $\mathbb{R}^L$  to  $H_\diamond$ . Since  $(u^2, U^2)$  is defined by (3.19) and the right-hand side of (3.19) is linear in  $\eta$ , the map is linear in  $\eta$  too. Taking  $(w, W) = (u^2, U^2)$  in (3.19), the continuity of the bilinear form gives us

$$\begin{aligned} \|(u^2, U^2)\|_*^2 &\lesssim \left| B_Z((u^2, U^2), (u^2, U^2)) \right| \\ &\lesssim \|\eta\|_{L^\infty(\Omega)} \|(u, U)\|_* \|(u^2, U^2)\|_*. \end{aligned}$$

Hence, we obtain the following estimate

$$\|(u^2, U^2)\|_* \lesssim \|\eta\|_\infty.$$

This ends the proof of the Gâteaux differentiability of the CEM forward solution with respect to the contact impedance.  $\square$

### 3.3.1 Discretization of the sensitivity equation with respect to the contact impedance

The derivative  $(u^2, U^2)$  of the potential  $(u, U)$  with respect to the contact impedance  $Z$  in the direction  $\eta$  is solution of the following boundary value

problem

$$\begin{aligned}
 \nabla \cdot (\sigma \nabla u^2) &= 0 && \text{in } \Omega \\
 u^2 + z_\ell \sigma \partial_{\bar{n}} u^2 &= -\eta_\ell \sigma \partial_{\bar{n}} u + U_\ell^2 && \text{on } e_\ell, \ell = 1, \dots, L, \\
 \int_{e_\ell} \sigma \partial_{\bar{n}} u^2 ds &= 0 && \ell = 1, \dots, L, \\
 \sigma \partial_{\bar{n}} u^2 &= 0 && \text{on } \partial\Omega \setminus \Gamma_e,
 \end{aligned} \tag{3.24}$$

where  $u$  is the solution of the unperturbed problem and satisfies  $\nabla \cdot (\sigma \nabla u) = 0$ . Meanwhile, the solution  $\tilde{u}^h$  of the perturbed problem with contact impedance  $\tilde{Z}$  also satisfies  $\nabla \cdot (\sigma \nabla u) = 0$ . Hence, the sensitivity  $u^2$  accordingly satisfies  $\nabla \cdot (\sigma \nabla u^2) = 0$ , which is the first equation of (3.24). Similarly, solutions  $\tilde{u}^h$  and  $u$  satisfy the boundary conditions  $\tilde{u}^h + (z_\ell + \eta_\ell h) \sigma \partial_{\bar{n}} \tilde{u}^h = \tilde{U}_\ell^h$  and  $u + z_\ell \sigma \partial_{\bar{n}} u = U_\ell$ , respectively, at each electrode. Subtracting the said boundary conditions and dividing by  $h$  leads to

$$\left( \frac{\tilde{u}^h - u}{h} \right) + z_\ell \sigma \partial_{\bar{n}} \left( \frac{\tilde{u}^h - u}{h} \right) + h \eta_\ell \sigma \partial_{\bar{n}} \tilde{u}^h = \tilde{U}_\ell^h - U_\ell.$$

At the limit  $h \rightarrow 0$ , we get that the sensitivity  $u^2$  satisfies the second equation of (3.24). The remaining boundary conditions are determined by the same method. Thus, the variational formulation of the problem (3.24) is given by (3.19) subject to the above boundary conditions.

We consider a mesh  $\mathcal{T}_h$  and the finite-dimensional space  $X_h$ . Thus, we have the approximation  $u_h$  of  $u$  be defined by (2.20). Furthermore, we denote the approximation of the sensitivity  $(u^2, U^2)$  by

$$u_h^2(\mathbf{x}) = \sum_{j=1}^N v_j^2 \varphi_j(\mathbf{x}) \tag{3.25}$$

with  $v_j^2$  as the approximation of the value of  $u^2$  at the  $j$ th node, and

$$U_h^2 = \sum_{k=1}^{L-1} \beta_k^2 \phi_k, \tag{3.26}$$

with  $U_h^2 = P\beta^2$  and  $\beta^2 = (\beta_k^2)^T \in \mathbb{R}^{L-1}$ . The approximation (3.25), and the choice of test-functions  $(w, W) = (\varphi_i, \mathbf{0})$  in (3.19) give for  $i = 1, \dots, N$

$$\begin{aligned}
 \sum_{j=1}^N v_j^2 \int_{\Omega} \sigma \nabla \varphi_j \cdot \nabla \varphi_i d\mathbf{x} + \sum_{\ell=1}^L \frac{1}{z_\ell} \int_{e_\ell} \left( \sum_{j=1}^N v_j^2 \varphi_j - \sum_{k=1}^{L-1} \beta_k^2 \phi_k \right) \varphi_i ds \\
 = \sum_{j=1}^N v_j \left( \sum_{\ell=1}^L \frac{\eta_\ell}{z_\ell^2} \int_{e_\ell} \varphi_i \varphi_j ds \right) - \sum_{\ell=1}^L U_h^\ell \left( \int_{e_\ell} \frac{\eta_\ell}{z_\ell^2} \varphi_i ds \right)
 \end{aligned} \tag{3.27}$$

with  $v = (v_j)_{j=1}^N$  as the approximated nodal values of  $u$  of the unperturbed

CEM (1.21) – (1.22) – (1.23) – (1.24) and  $U_h = (U_h^\ell) \in \mathbb{R}^L$  is obtained from (2.30). The boundary conditions in (3.24) lead to the following relation

$$\frac{1}{z_\ell} \int_{e_\ell} (U_\ell^2 - u^2) ds = \frac{\eta_\ell I_\ell}{z_\ell} \quad \ell = 1, 2, \dots, L. \quad (3.28)$$

We get the corresponding linear system of size  $N + L - 1$

$$\begin{bmatrix} S + M & C \\ C^T & G \end{bmatrix} \begin{bmatrix} v^2 \\ \beta^2 \end{bmatrix} = \begin{bmatrix} Qv + DU_h \\ P^T \mathcal{I} \end{bmatrix}, \quad (3.29)$$

where the matrices  $S$ ,  $M$ ,  $C$ , and  $G$  are defined by (2.24), (2.25), (2.26), and (2.29), respectively. Moreover, we have  $v^2 = (v_j^2)_{j=1}^N$ ,  $Q = (Q_{ij}) \in \mathbb{R}^{N \times N}$  with

$$Q_{ij} = \sum_{\ell=1}^L \frac{\eta_\ell}{z_\ell^2} \int_{e_\ell} \varphi_i \varphi_j ds, \quad D = (D_{i\ell}) \in \mathbb{R}^{N \times L} \text{ with } D_{ij} = -\frac{\eta_\ell}{z_\ell^2} \int_{e_\ell} \varphi_i ds, \text{ and}$$

$$\mathcal{I} = \left( \frac{\eta_\ell I_\ell}{z_\ell} \right)_k \in \mathbb{R}_\diamond^L.$$

## 3.4 Numerical sensitivity analysis

We study numerically how a slight variation of the conductivity or of the contact impedance of electrodes affect EIT measurements for different two- and three-dimensional configurations. The 3D numerical results have been obtained by Jérémy Heleine, and are part of a paper in preparation [DHMV].

### 3.4.1 Set-up

#### Two-dimensional set-up

First, we consider three two-dimensional configurations which are the Cases 1a, 2a, and 3a described in Section 2.4 (see Figure 3.1).

The number of electrodes attached around the boundary of the studied domain  $\Omega$  is  $L = 32$  (see Figure 2.7). The current pattern  $I = (I_\ell)_\ell$  is defined by (as in Section 2.4.2)

$$I_\ell = \sin\left(\frac{2\pi\ell}{L}\right), \quad \ell = 0, 1, 2, \dots, L - 1.$$

All simulations are executed with the software FreeFem++ [Hec12]. The different linear systems are solved with the default direct sparse solver in FreeFem++.

#### Three-dimensional set-up

We consider two geometries: the unit ball and a spherical head model. In the unit ball, the background conductivity is fixed to  $0.33 \text{ S} \cdot \text{m}^{-1}$ . The mesh size used for the unit ball is  $h = 0.074$ , for a total of 501 044 tetrahedrons and 87 817 nodes. The spherical head model consists in three concentric balls  $B_1$ ,  $B_2$  and  $B_3$ , of respective radii  $r_1 = 0.87$ ,  $r_2 = 0.9$  and  $r_3 = 1$  (see Figure 3.2).

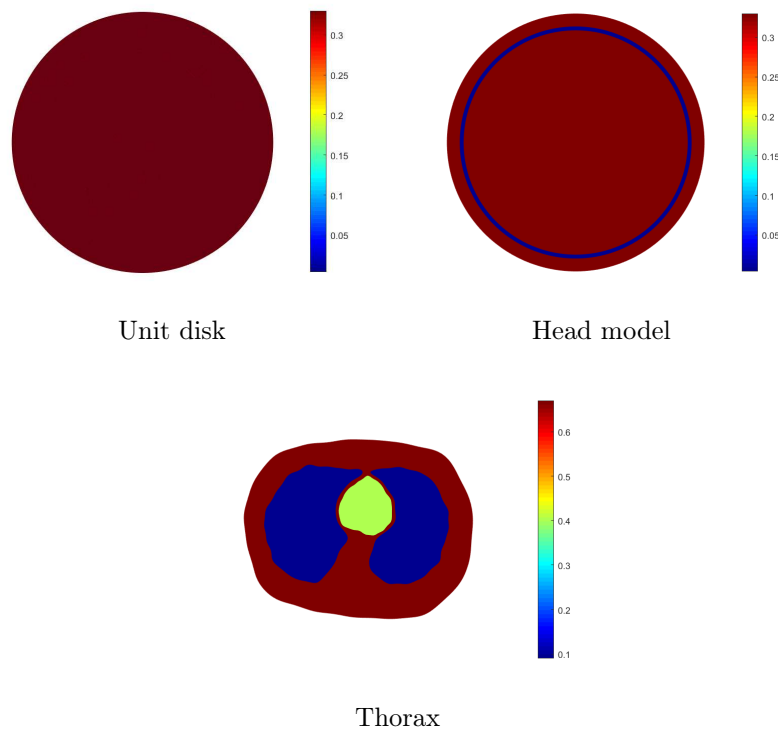


FIGURE 3.1: Illustration of the geometries considered: a unit disk, a head model and a thorax.

The regions  $\Omega_1 = B_1$ ,  $\Omega_2 = B_2 \setminus \Omega_1$  and  $\Omega_3 = B_3 \setminus \Omega_2$  represent the brain, the skull, and the scalp, respectively. The values chosen for the conductivity in these tissues are the same as the 2D ones:  $0.33 \text{ S} \cdot \text{m}^{-1}$  for the brain and the scalp layers, and  $0.004 \text{ S} \cdot \text{m}^{-1}$  for the bone layer. The mesh uses 572 497 tetrahedrons and 99 546 nodes, ending up with a mesh size of  $h = 0.074$ .

We consider standard positioning for the electrodes and use the 10-10 system (see Figure 3.2) [FvM11]. This system gives us the spherical coordinates of the centers of  $L = 71$  electrodes which are represented by small patches: the intersection of  $\partial\Omega$  with a ball of radius 0.1. The contact impedance is the same on all electrodes and fixed to 0.1. For  $\ell = 0, 1, \dots, L - 1$ , the electrode  $e_\ell$  is defined by the longitude  $\theta_\ell \in [0, 2\pi[$  and latitude  $\varphi_\ell \in [-\pi/2, \pi/2]$  of its center. The current pattern  $I_\ell$  on this electrode is set to

$$I_\ell = \sin \theta_\ell \cos \varphi_\ell.$$

### 3.4.2 Numerical sensitivity analysis with respect to the conductivity

The sensitivity  $(u^1, U^1)$  of the potential in the given direction  $\mu$  is computed as the solution of the linear system (3.14). The contact impedance is set to be constant across all electrodes on the boundary, that is,  $z_\ell = 0.1, \forall \ell = 0, \dots, L - 1$ .



FIGURE 3.2: Left: layers of the spherical head model. Middle: front view of the 10-10 system for the electrodes positioning. Right: back view of the 10-10 system.

### Numerical results in 2D

We study three domain cases of Section 2.4: Case 1a, 2a, and 3a. The same FEM mesh structure presented in Table 2.8 are used for the simulations.

**Unit disk.** We set the background conductivity equal to  $0.33 \text{ S} \cdot \text{m}^{-1}$ . We consider a perturbation in the conductivity. This perturbation is modeled by a disk  $D = D_r(\mathbf{x}_0)$  of radius  $r$  centred at  $\mathbf{x}_0$ . The direction is  $\mu = \mathbf{1}_D$ . At the top of Figure 3.3, the perturbation of radius  $r = 0.1$  is placed at two different positions, namely  $\mathbf{x}_0 = (0.4, 0)$  (I) and  $\mathbf{x}_0 = (0.7, 0)$  (II). In the bottom left of Figure 3.3, we report the absolute value of the sensitivity corresponding to the circular inhomogeneity centered at  $\mathbf{x}_0 = (0.4, 0)$  for a bigger radius  $r = 0.3$  (III).

The simulations indicate how the position of the inhomogeneity affects sensitivity. In particular, it shows that the largest values of the sensitivity are observed around the inhomogeneity. The sensitivity decreases away from the defect. The sensitivity on the boundary is localized in the side of the perturbation. Moreover, increasing the inhomogeneity's size increases the amplitude of the sensitivity significantly. Finally, in the bottom right of Figure 3.3, we present the sensitivity corresponding to two circular perturbations: one centred at  $\mathbf{x}_0 = (0.4, 0)$  of radius  $r = 0.1$  and the other centred at  $\mathbf{x}_0 = (-0.4, -0.5)$  of radius  $r = 0.2$  (IV). The sensitivity on the boundary reaches maximum values at the electrodes close to the bigger inhomogeneity.

Table 3.1 reports the sensitivity values at some chosen electrodes and we can observe that it supports the conclusions given above. The sensitivity of the voltages at the electrodes near the inclusion which are  $e_4$  and  $e_{30}$  for Simulations I and II has bigger values than the ones far from it. Furthermore, we confirm that those electrodes record bigger values of the sensitivity when the inclusion is very near the boundary (Simulations II and IV) and when the inclusion is larger in size (Simulations III and IV).

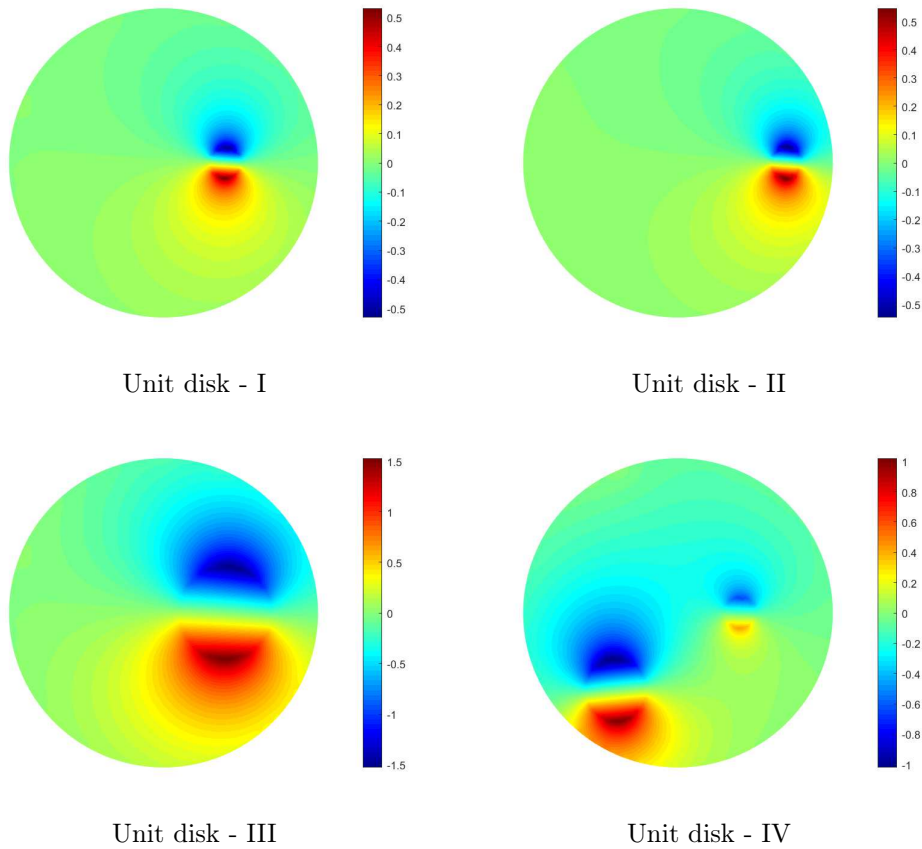
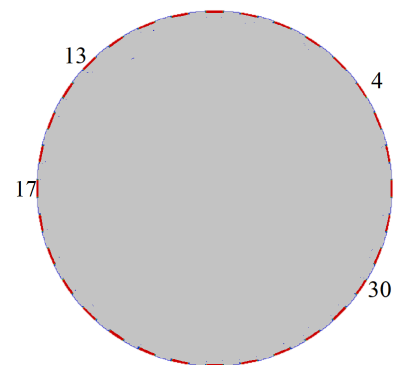


FIGURE 3.3: Unit disk. Sensitivity of the electric potential with respect to the conductivity (top left (I):  $\mathbf{x}_0 = (0.4, 0)$ ,  $r = 0.1$ , top right (II):  $\mathbf{x}_0 = (0.7, 0)$ ,  $r = 0.1$ , bottom left (III):  $\mathbf{x}_0 = (0.4, 0)$ ,  $r = 0.3$ , bottom right (IV): two disjoint perturbations, one is centered at  $\mathbf{x}_0 = (0.4, 0)$  with radius  $r = 0.1$  and the other is centered at  $\mathbf{x}_0 = (-0.4, -0.5)$  with radius  $r = 0.2$ ).

Unit disk				
Electrode	I	II	III	IV
4	-0.0444	-0.0720	-0.4054	-0.0926
13	0.0003	0.0013	0.0036	0.0354
17	-0.0004	0.0023	-0.0046	-0.1593
30	0.0409	0.0737	0.3779	0.0040

TABLE 3.1: Unit disk. Numerical sensitivity of the voltages with respect to conductivity at selected electrodes.



**Head model.** We consider the same conductivity distribution as in Case 2a in 2.4, that is, the adopted conductivity values are  $\sigma_1 = \sigma_3 = 0.33 \text{ S} \cdot \text{m}^{-1}$  for the brain and scalp, respectively, and  $\sigma_2 = 0.004 \text{ S} \cdot \text{m}^{-1}$  for the skull. We then examine the effect of a small perturbation in the conductivity of the region  $\Omega_1$  modeling the brain. Figure 3.3 compares the sensitivity of the potential with respect to a perturbation of different locations and areas. We perform the same test-cases as for the unit disk (see Figure 3.4 and Table 3.2). We observe the same behaviour of the sensitivity, with respect to the location, size, and number of perturbations. However, notice that the sensitivity values in this case are significantly smaller than that of the unit disk. This is in accordance with the behaviour of the perturbed potential for Case 2 shown in Figure 2.9 and Table 2.10 when compared with the homogeneous unit disk. Furthermore, we again note that there is a significant decrease in the sensitivity value for all the test-cases. The sensitivity values around the boundary are close to zero. This might be due to high resistivity of the skull. The bottom left image in Figure 3.4 shows the sensitivity of the potential when the conductivity of the skull is perturbed and there is no perturbation in the brain. The sensitivity values of the voltages at some electrodes for this simulation appear in Table 3.2. They are significantly larger than the ones obtain from Simulations I-IV. It confirms that EIT measurements are extremely sensitive to uncertainties in the skull conductivity.

Head model					
Electrode	I	II	III	IV	skull
4	-0.0040	-0.0063	-0.0368	-0.0102	-45.80
13	0.0001	0.0002	0.0010	0.0025	0.6728
17	-0.0001	7.7E-05	-0.0012	-0.0139	-14.24
30	0.0034	0.0062	0.0314	0.0011	26.24

TABLE 3.2: Head model. Numerical sensitivity of the voltages with respect to conductivity at selected electrodes.

**Thorax.** We consider Case 3a of Section 2.4 with the blood's conductivity equal to  $0.67 \text{ S} \cdot \text{m}^{-1}$  and the conductivities of the lungs and the heart are, respectively, fixed to  $0.09 \text{ S} \cdot \text{m}^{-1}$  and  $0.4 \text{ S} \cdot \text{m}^{-1}$  [MPH06]. Figure 3.5 shows the sensitivity of the potential with respect to a small perturbation in the blood conductivity. We compare different locations and areas for the perturbation. We again observe that perturbations near the boundary achieve relatively larger amplitudes of the sensitivity. Also, increasing the inhomogeneity's size increases the sensitivity values greatly. Table 3.3 details the sensitivity values at some chosen electrodes and we deduce the same conclusions given above. The sensitivity values are not significantly large but we can easily see the electrodes which are more sensitive to a small change in the blood conductivity.

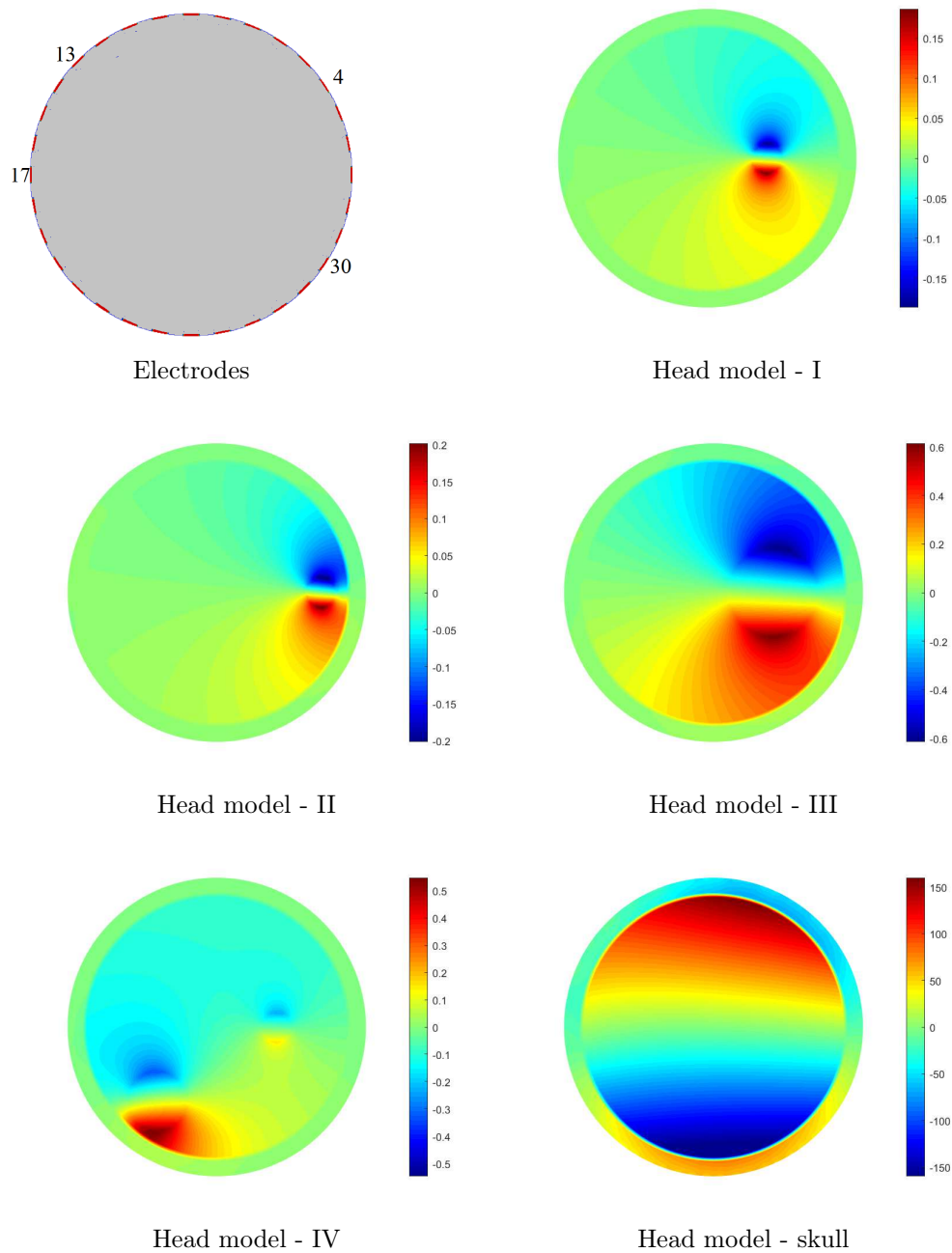


FIGURE 3.4: Head model. Sensitivity of the electric potential with respect to the conductivity (top left (I):  $\mathbf{x}_0 = (0.4, 0)$ ,  $r = 0.1$ , top right (II):  $\mathbf{x}_0 = (0.7, 0)$ ,  $r = 0.1$ , bottom left (III):  $\mathbf{x}_0 = (0.4, 0)$ ,  $r = 0.3$ , bottom right (IV): two disjoint perturbations, one is centered at  $\mathbf{x}_0 = (0.4, 0)$  with radius  $r = 0.1$  and the other is centered at  $\mathbf{x}_0 = (-0.4, -0.5)$  with radius  $r = 0.2$ ), skull: small perturbation in the skull conductivity

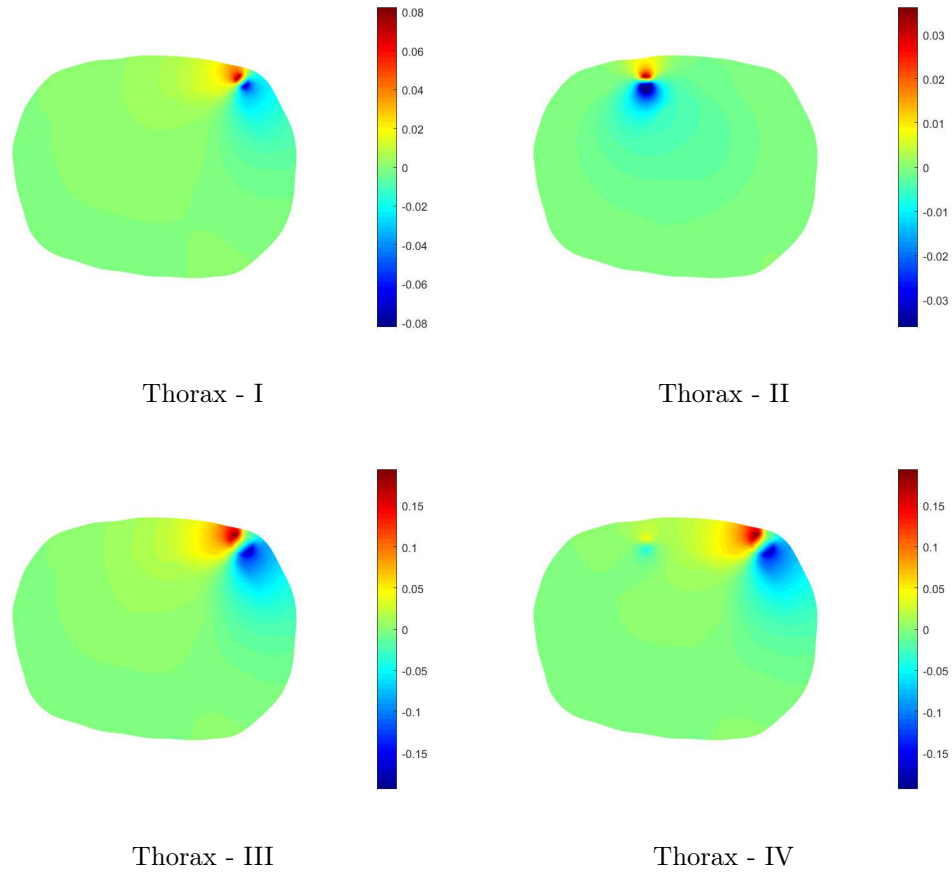


FIGURE 3.5: Thorax. Sensitivity of the electric potential with respect to the conductivity (top left (I):  $\mathbf{x}_0 = (2.62, 2.25)$ ,  $r = 0.05$ , top right (II):  $\mathbf{x}_0 = (1.6, 2.25)$ ,  $r = 0.05$ , bottom left (III):  $\mathbf{x}_0 = (2.62, 2.25)$ ,  $r = 0.1$ , bottom right (IV): two disjoint perturbations,  $\mathbf{x}_0 = (2.62, 2.25)$  with radius  $r = 0.1$ , and the other is centered at  $\mathbf{x}_0 = (1.6, 2.25)$  with radius  $r = 0.05$ ).

Thorax				
Electrode	I	II	III	IV
6	-0.0001	-0.0004	-0.0015	-0.0019
20	-0.0195	-0.0005	-0.0731	-0.0736
22	0.0343	-0.0007	0.1291	0.1283
27	0.0017	0.0059	0.0062	0.0122

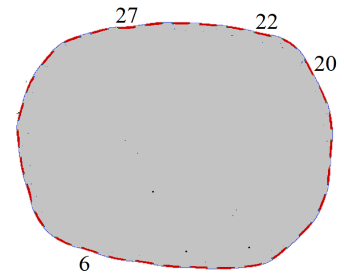


TABLE 3.3: Thorax. Numerical sensitivity of the voltages with respect to conductivity at selected electrodes.

### Numerical results in 3D

**Unit ball.** We first consider a spherical perturbation of center  $(0.45, 0, 0.45)$  and of radius 0.2. We show on the top image of Figure 3.6 the sensitivity  $u^1$  with respect to the conductivity in the direction corresponding to the indicator function of this ball. Middle and bottom images of Figure 3.6 report the sensitivity in the direction of a perturbation centered at  $(0, 0.3, 0.35)$  with radius 0.2 and 0.35, respectively. As in 2D, we observe the largest values of the sensitivity around the support of the perturbation. Increasing the volume of the inhomogeneity increases the amplitude of the sensitivity of the interior potential and of the surface voltages.

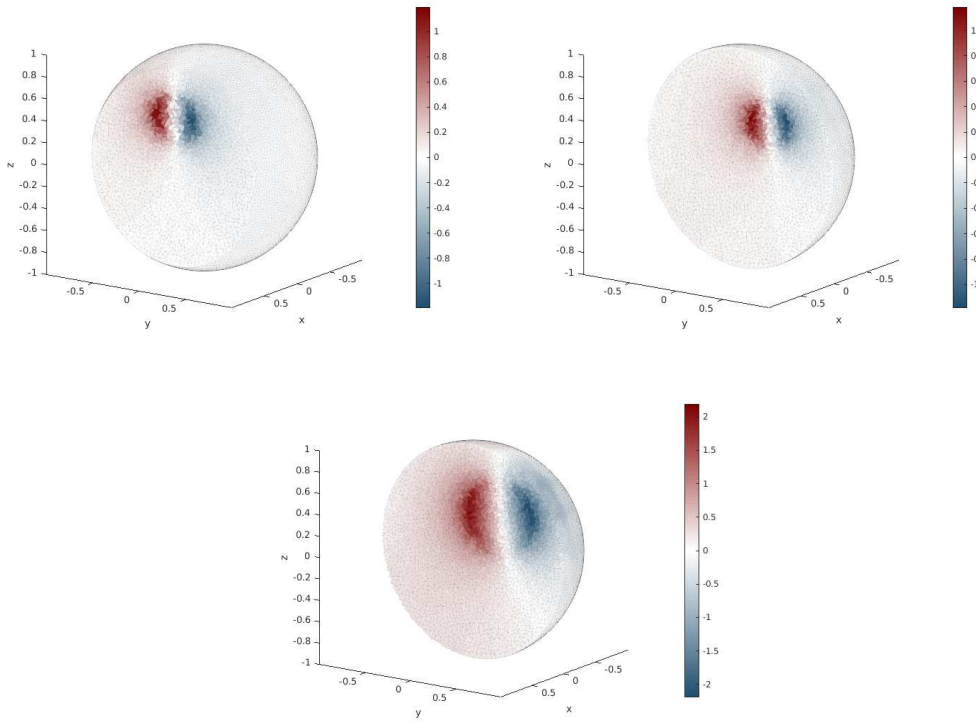


FIGURE 3.6: Unit ball. Sensitivity of the electric potential with respect to the conductivity in the direction of the indicator function of the support of an inhomogeneity. Top left: centered at  $(0.45, 0, 0.45)$  with radius 0.2. Top right: centered at  $(0, 0.3, 0.35)$  with radius 0.2. Bottom: centered at  $(0, 0.3, 0.35)$  with radius 0.35.

**Spherical head model.** We consider the same test cases as for the unit ball. These three perturbations are all contained in the brain layer. The corresponding sensitivities are shown in Figure 3.7. We observe the same behavior as with the unit ball if we look at the location of the biggest sensitivity values. However, the amplitude of these values is lower here than in the unit ball because of the presence of the skull. In Figure 3.8, we show on the left the values of the sensitivity on the boundary of the domain. On the right, we can observe the resulting

values on the electrodes. Top of the figure is the case of a spherical perturbation centered at  $(0, 0.3, 0.35)$  with radius 0.2. On the bottom, the perturbation is of same radius and centered at  $(0, -0.3, 0.35)$ . It appears that the highest absolute values of the surface measurements are located on the electrodes that are the nearest from the perturbation. The sign of these values seems to be governed by the sign of the injected current, which is the same as the sign of the  $y$ -coordinate. In fact, we observe that the positive part of the sensitivity is oriented to the part of the boundary where a negative current is injected. This behavior matches the one which can be observed on 2D simulations.

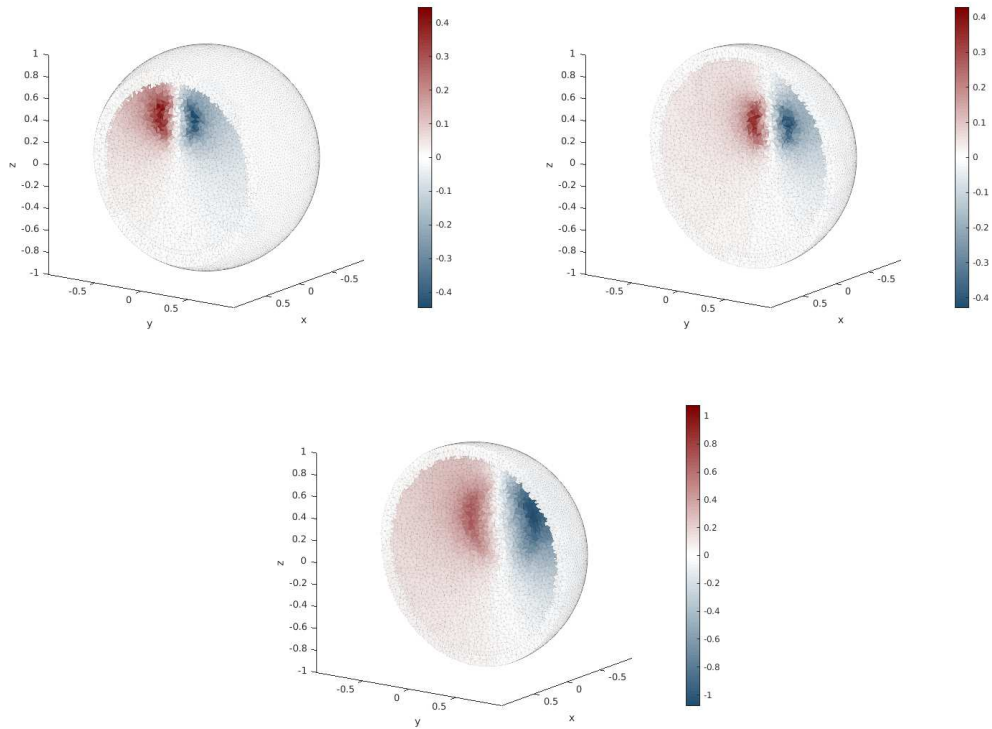


FIGURE 3.7: Spherical head model. Sensitivity of the electric potential with respect to the conductivity in the direction of the indicator function of the support of an inhomogeneity in the brain. Top left: centered at  $(0.45, 0, 0.45)$  with radius 0.2. Top right: centered at  $(0, 0.3, 0.35)$  with radius 0.2. Bottom: centered at  $(0, 0.3, 0.35)$  with radius 0.35.

The inverse problem we are interested in, consists of the reconstruction of the conductivity inside the domain from the knowledge of the electrical potential values at the electrodes, which represent the EIT measurements. Assuming that the conductivity in healthy domains is known, this problem is equivalent to looking for inhomogeneities in this background parameter. Then, a similar argument to the one involved in [DHL19] for Maxwell's equations can be invoked: the Gâteaux derivative can be used to better understand the difference between the measurements on healthy and perturbed domains and to propose an inversion algorithm for reconstructing the characteristics of dielectrical inclusions. In [KHM06; ARE19], the authors studied the sensitivity distribution of

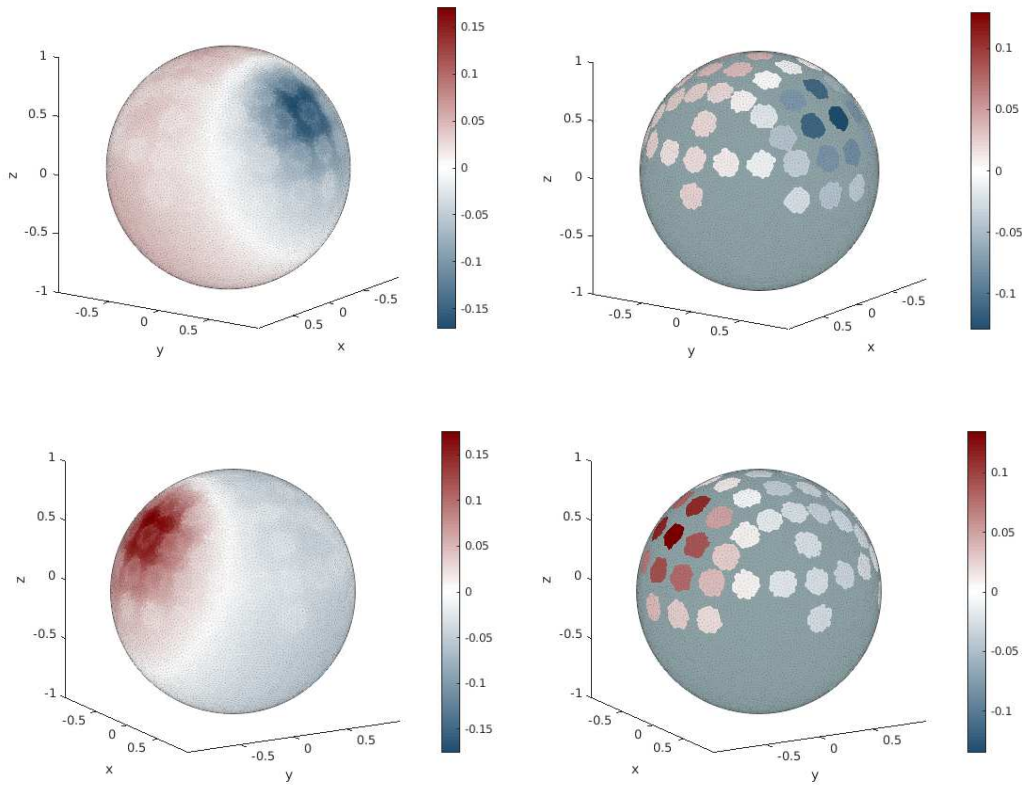


FIGURE 3.8: Spherical head model. Boundary values of the sensitivity of the electric potential with respect to the conductivity in the direction of the indicator function of the support of a spherical inhomogeneity.

an impedance measurement which describes the change in measured impedance caused by a given conductivity distribution. Kauppinen et. al [KHM06] concluded in their paper that sensitivity are found low in deeper regions of the medium, while in [ARE19], they summarized the effect of different conductivity of the tissue layers to the performance of the EIT system, that is, a high sensitivity distribution is determined in the muscle layer with high electrical conductivity. Moreover, inhomogeneous medium yield a non-uniformly and high sensitivity distribution pattern as compare to that of the homogeneous medium.

### 3.4.3 Numerical sensitivity analysis with respect to the contact impedance

We compute the sensitivity  $(u^2, U^2)$ , solution of the linear system (3.19) with direction  $\eta \in \{0, 1\}^L$ : for  $1 \leq \ell \leq L$ ,  $\eta_\ell$  is set to 1 if we consider a perturbation of the contact impedance of the  $\ell$ -th electrode, and to 0 otherwise.

#### Numerical results in 2D

**Unit disk.** We study a perturbation of the contact impedance at the 7th electrode, i.e.  $\eta_\ell = 0$  for all  $1 \leq \ell \leq L$  except for  $\eta_7 = 1$ . Figure 3.9 shows the

values of the sensitivity inside the domain  $u^2$  in the case of a perturbation on the 7th (I), 19th (II) and on both electrodes (III), while Table 3.4 reports the corresponding sensitivity values  $U^2$  of the perturbed electrodes. We first notice that the values of  $U^2$  show a peak: the highest amplitude can be observed at the perturbed electrode. This behavior has been observed in all cases where a single electrode is perturbed. Moreover, the case of two perturbed electrodes shows two peaks, each located at a perturbed electrode. It is in fact an illustration of the linearity of the sensitivity equation (3.19) with respect to the direction of derivation: the vector  $\eta$  in the case of two perturbed electrodes is the sum of the two vectors corresponding to each electrode perturbed independently. Then, the sensitivities can also be summed to obtain the sensitivity corresponding to a perturbation of both electrodes.

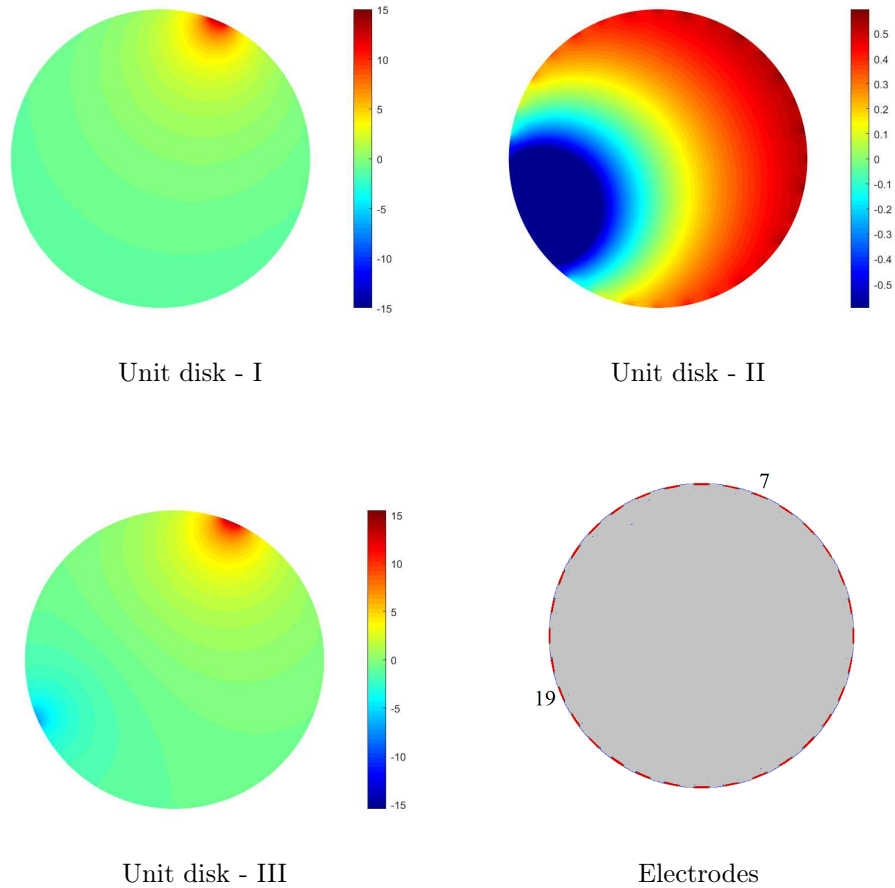


FIGURE 3.9: Unit disk. Sensitivity of the electric potential with respect to the contact impedance in the direction of a perturbation on the 7th electrode (leftmost), 19th electrode (middle) and on both electrodes (rightmost)

**Head model.** We study the same perturbations as in the unit disk. Figure 3.10 and Table 3.5 present the sensitivity inside the domain and on the perturbed electrodes, respectively. We also deduce the same conclusions as in the case of the unit disk.

Unit disk			
Electrode	I	II	III
7	22.479	0.61080	23.090
19	-1.4677	-9.3352	-10.803

TABLE 3.4: Case 1: Numerical sensitivity of the voltages with respect to contact impedance at selected electrodes.

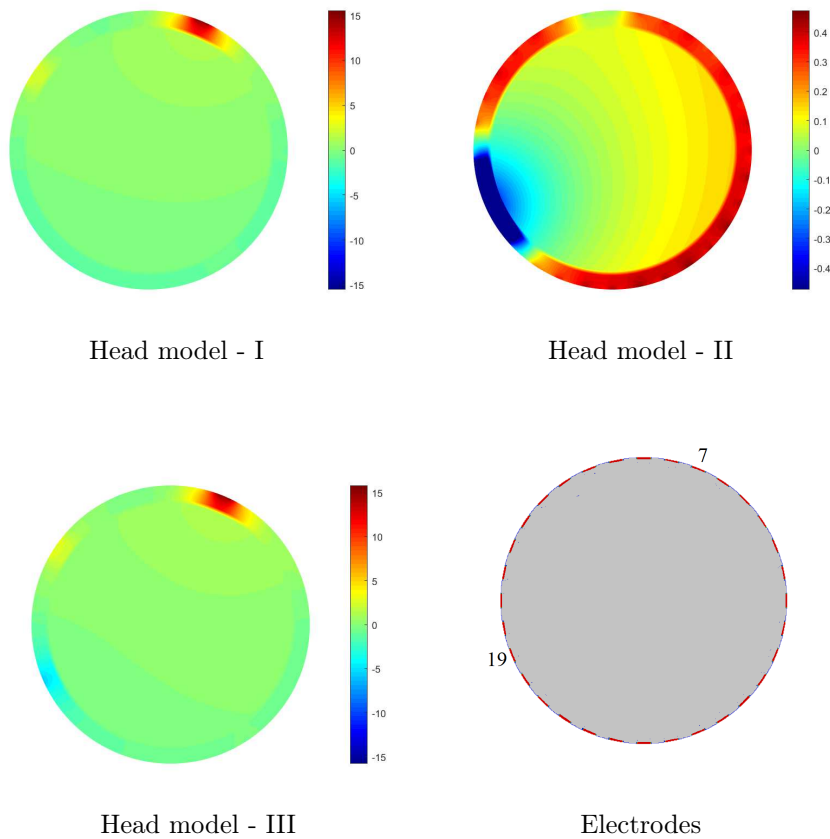


FIGURE 3.10: Head model. Sensitivity of the electric potential with respect to the contact impedance in the direction of a perturbation on the 7th electrode (leftmost), 19th electrode (middle) and on both electrodes (rightmost)

Head model			
Electrode	I	II	III
7	23.346	0.4049	23.751
19	-1.6192	-8.6592	-10.278

TABLE 3.5: Case 2: Numerical sensitivity of the voltages with respect to contact impedance at selected electrodes.

**Thorax.** We consider the same perturbations as in the unit disk. Figure 3.11 displays the values of  $u^2$ , while Table 3.6 details the numerical sensitivity values on the perturbed electrodes. Similar observations are gathered in this case.

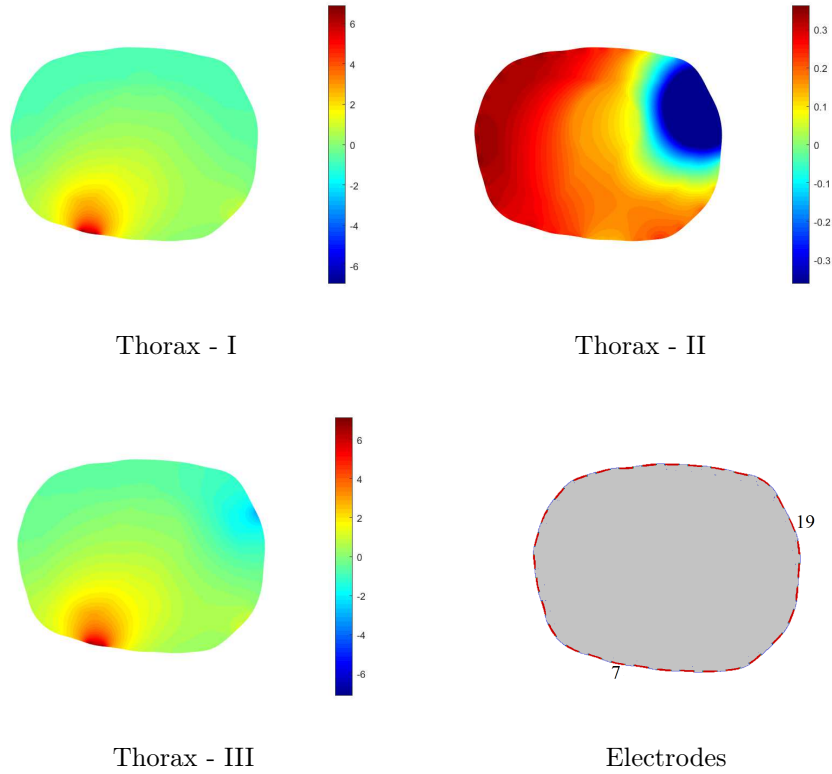


FIGURE 3.11: Thorax. Sensitivity of the electric potential with respect to the contact impedance in the direction of a perturbation on the 7th electrode (leftmost), 19th electrode (middle) and on both electrodes (rightmost)

Thorax			
Electrode	I	II	III
7	12.110	0.3018	12.412
19	-0.9920	-6.1550	-7.1470

TABLE 3.6: Case 3: Numerical sensitivity of the voltages with respect to contact impedance at selected electrodes.

### Numerical results in 3D

**Unit ball.** We first consider a perturbation on the 6th electrode, i.e.  $\eta_\ell = 0$  for all  $1 \leq \ell \leq L$  except for  $\eta_6 = 1$ . We show on the top left of Figure 3.12 the values of the sensitivity on the electrodes, i.e. the values of the vector  $U^2$ . On the top right, we report the values of this same vector in the case of

a perturbation on the 31st electrode. The bottom of this figure presents the values of the vector  $U^2$  in the case of both the 6th and the 31st electrodes are perturbed. The conclusions are confirmed. The impact of a defective electrode of the EIT measurements is localized.

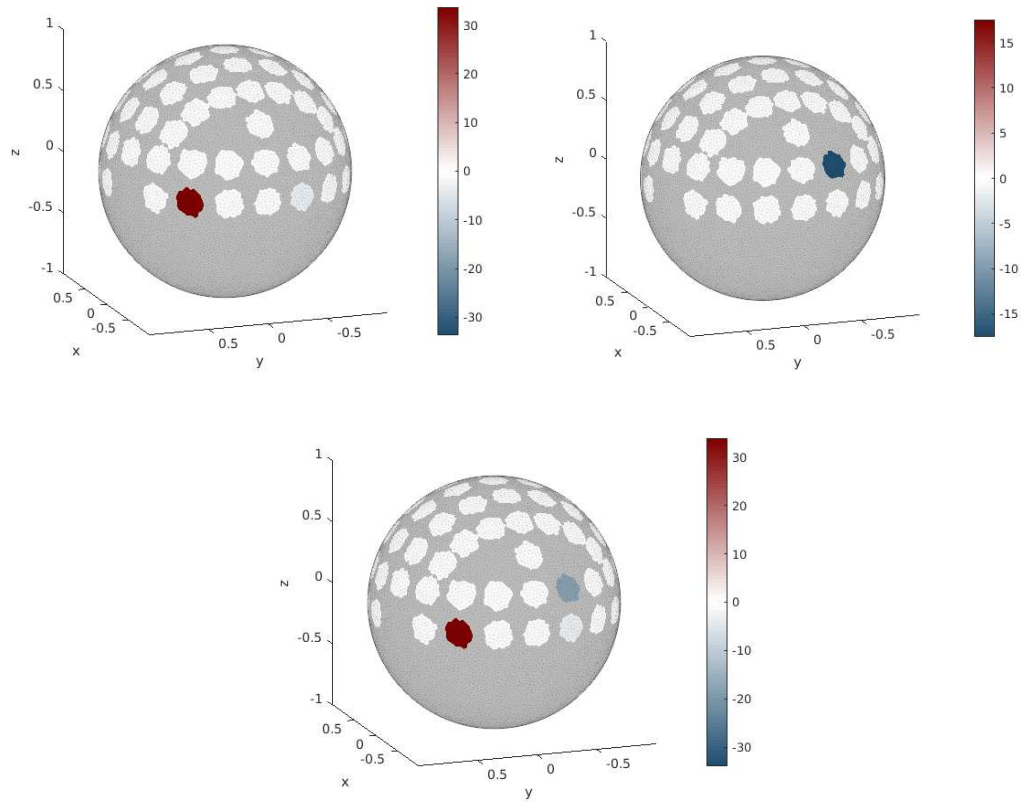


FIGURE 3.12: Unit ball. Values of the sensitivity of the electric potential with respect to the contact impedance in the direction of a perturbation on the 6th electrode (top left), on the 31st (top right) and on both electrodes (bottom).

### 3.5 Conclusion and perspectives

We introduced the Gâteaux derivative as a tool for the sensitivity analysis of the electric potential in the CEM forward problem and showed that it is Gâteaux differentiable with respect to the conductivity and to the contact impedance of the electrodes. We have also expressed its derivative as a solution to a variational problem and applied the FEM for the discretization. We have presented several numerical simulations for different 2D and 3D configurations. The electric potential and the surface voltages are more sensitive to inhomogeneities in the conductivity that are located near the boundary and to those that are larger in size. Furthermore, the potential's sensitivity with respect to contact impedance is localized on the perturbed electrode and when an additional electrode is perturbed, the total sensitivity is the sum of the corresponding sensitivities.

This study gives insights on the sensitivity of the EIT measurements with respect to a small perturbation (or uncertainty) in the conductivity, and with respect to a small defect in some electrodes. In both cases, the impact is localized. We have observed that, in the head model, an uncertainty of a tissue conductivity value could have a great impact on the measurements, and hence on the reconstruction. It would be interesting to explicit relations between the sensitivity values and the characteristics of the perturbations as in [DHL19]. Another perspective could be not to study the effect separately but to perturb both the conductivity and the contact impedance. For instance, it seems that an inhomogeneity in the conductivity which is localized near a defective electrode could be problematic for the EIT inverse problem. Other properties of the electrodes can be taken into account: position, size, shape [JAMHB15]. This chapter offers many further theoretical and numerical questions.

## Chapter 4

# Metaheuristic algorithms for solving the 2D EIT inverse problem

This chapter focuses on the numerical resolution of the inverse conductivity problem for EIT using metaheuristic algorithms. To this end, the inverse problem is formulated as a minimization problem. Several metaheuristic algorithms are introduced and presented in detail. Two-dimensional numerical simulations are performed to compare their accuracy and efficiency. This chapter is the development of an article, titled "Comparative Study of Heuristic Algorithms for Electrical Impedance Tomography", accepted for publication in *Philippine Journal of Science* [VDMBL20].

### 4.1 Formulation of the inverse problem

As an inverse conductivity problem, EIT aims to find the unknown conductivity distribution  $\sigma$  in the body  $\Omega$  given the simultaneous measurements of voltages  $U$  and current patterns  $I$  on the boundary  $\partial\Omega$ . Whereas the forward problem is well-posed, the inverse problem of EIT is nonlinear and highly ill-posed which makes EIT still an active area of research nowadays. In the mathematical literature the inverse problem of EIT is also known as Calderón's problem [Cal80]. Earlier results on EIT inverse problem is focused on the identifiability question that the conductivity distribution in the domain can be uniquely determined, given the boundary measurements. In particular, can a strictly positive conductivity in the elliptic equation (1.21) be uniquely determined in a bounded domain by the entire corresponding voltage-to-current or Dirichlet-to-Neumann (DtN) map on the boundary of the domain. In its original paper [Cal80], Calderón gave an approximation formula to a conductivity that is close to a constant conductivity, assuming the full knowledge on all possible boundary data pairs. However, the first identifiability result for the continuum model was given by Kohn and Vogelius in [KV84]. They proved the unique identifiability of  $\sigma$  and its normal derivative on the boundary using a full knowledge of the DtN map and under the assumptions that the domain is bounded,  $C^\infty$  domain, and  $\sigma \in L^\infty(\bar{\Omega})$  is a strictly positive function, which is  $C^\infty$  in a neighborhood of  $\partial\Omega$ . Astala and Päivärinta later extended the identifiability from the DtN results for  $L^\infty$  conductivity in two dimensions [AP06]. Results have also been obtained on the problem of whether one can determine the conductivity

in the interior from only partial information on the DtN map (e.g. [KSU07; IUY10; HPS12]). For more detail we refer to the review papers [Uhl09; Bor03].

Furthermore, EIT in practice injects a current pattern on the boundary and then records the resulting boundary voltage measurements. With this set-up, we define instead the current-to-voltage relation known as the Neumann-to-Dirichlet (NtD) map for the continuum model. Moreover, since voltage measurements are known to be noisy in nature, the solution can be dominated by noise unless additional conditions are imposed. As such, EIT is a particularly difficult example of attempting to recover a signal from noise [Hol00]. In line with this, one of the advantages of using NtD map is that it is smoothing and so, it is better behaved for noisy measurements. Recall from Section 2.1.1 the space (2.1)

$$\tilde{L}(\partial\Omega) = \left\{ f \in L^2(\partial\Omega) \mid \int_{\partial\Omega} f \, d\mathbf{x} = 0 \right\}. \quad (4.1)$$

We define the map  $\Lambda_\sigma : \tilde{L}(\partial\Omega) \mapsto \tilde{L}(\partial\Omega)$  given by

$$\Lambda_\sigma(f) = u|_{\partial\Omega}, \quad (4.2)$$

where  $u \in \mathcal{H} = \left\{ u \in H^1(\Omega) \text{ such that } \int_{\partial\Omega} u \, ds = 0 \right\}$  (2.2). The operator  $\Lambda_\sigma$  is called the NtD map and depends nonlinearly on  $\sigma$ . The NtD map is also self-adjoint and positive-definite [Bor03]. The EIT inverse problem is finding  $\sigma$  given the NtD map  $\Lambda_\sigma$ . However, in several applications in EIT, a full knowledge of the NtD map is impossible to obtain since one can only measure currents and voltages on part of the boundary. Hence, we find the conductivity  $\sigma$  given a partial, noisy knowledge of  $\Lambda_\sigma$  for the EIT reconstruction problem. Results on determining the conductivity in the interior from only partial information on the NtD map are discussed in [KSU07; IUY10; HPS12; Hyv04].

On the other hand, for real-life measurements using CEM, a linear relation between the applied average currents  $I_\ell$  and the electrode voltages  $U_\ell$ ,  $1 \leq \ell < L$ , is the only obtained information [Hyv04]. The data consist, essentially, of a finite-dimensional linear electrode current-to-electrode voltage operator  $R_\sigma$  given by

$$R_\sigma I = U, \quad (4.3)$$

where  $R_\sigma : \mathbb{R}^L \rightarrow \mathbb{R}^L$  [Hyv04]. The EIT inverse problem for CEM is the recovery of  $\sigma$  given the linear map  $R_\sigma$ . We can say that  $R_\sigma$  is the discrete counterpart of the continuous map  $\Lambda_\sigma$  and  $R_\sigma$  has also the some characteristics of  $\Lambda_\sigma$  such as being self-adjoint and positive [Hyv04]. Lastly, the resemblance between the two operators gets better when the area covered by the electrodes gets larger and the electrodes get smaller.

The challenging issues for EIT are to provide numerical methods for reconstructing the conductivity of a medium from a finite number of boundary measurements. There are two primary types of algorithms in EIT: *static imaging* [YWT87; VN17] and *difference imaging* [BB84; VN17]. Static imaging attempts to recover the absolute conductivity distribution of a body, whereas difference imaging aims to recover an image of the change in conductivity distribution between the acquisition times of two data. We focus on static imaging,

which is suitable for the case when the electrical properties of the body under study do not vary significantly during the time necessary for data collection [HVMAL07].

In this chapter, we assume that  $\sigma$  is piecewise constant, that is,

$$\sigma(\mathbf{x}) = \sum_{i=0}^n \sigma_i \chi_i(\mathbf{x}), \mathbf{x} \in \Omega,$$

where  $\sigma_0$  is the background conductivity,  $\chi_0(\mathbf{x})$  is the characteristic function of the background domain  $\Omega_0 = \Omega \setminus \bigcup_{i=1}^n \Omega_i$ ,  $n$  corresponds to the number of (possible) inclusions  $\Omega_i$  ( $i = 1, \dots, n$ ) in  $\Omega$ ,

$$\chi_i(\mathbf{x}) = \begin{cases} 1, & \mathbf{x} \in \Omega_i, \\ 0, & \mathbf{x} \notin \Omega_i, \end{cases}$$

and  $\sigma_i$  is the conductivity of the  $i^{\text{th}}$  inclusion  $\Omega_i$  with  $\sigma_{\min} \leq \sigma_i \leq \sigma_{\max}, \forall i = 1, \dots, n$  for some constants  $0 < \sigma_{\min}, \sigma_{\max} < +\infty$  (Definition 1.2.1).

We aim to retrieve the  $n$  inclusions of different conductivities in  $\Omega$ . More precisely, the goal is to estimate iteratively a vector  $P \in \mathbb{R}^m$  of unknown parameters and the vector  $S := (\sigma_i)_{i=1}^n$  of conductivities, for which the error between the measured voltages and that predicted by the CEM forward problem is minimized. The vector  $P$  contains geometric attributes (e.g., center, radius, side length) of the inclusions  $\Omega_i$ ,  $i = 1, \dots, n$  (of respective conductivities  $\sigma_i$ ). The objective function reads

$$C(P, S) = \|U(P, S) - U_{\text{obs}}\|_2^2, \quad (4.4)$$

where the voltages  $U(P, S) \in \mathbb{R}^L$  are computed by solving the forward problem (1.21) – (1.22) – (1.23) – (1.24) at a fixed conductivity  $\sigma$  (described by the vectors  $P$  and  $S$ ) and  $U_{\text{obs}} \in \mathbb{R}^L$  is the measured voltage at the electrodes, and  $\|\cdot\|_2$  is the Euclidean norm. In the next section, we discuss the metaheuristic algorithms we use to minimize the cost function  $C(P, S)$  in (4.4).

## 4.2 Presentation of the metaheuristic algorithms

### 4.2.1 Introduction

Metaheuristics is from the family of approximate optimization methods that follow a high-level problem-independent algorithmic framework. Indeed, the prefix “meta” is used to indicate that these algorithms are “higher level” heuristics, in contrast with problem-specific heuristics [BLS13; WC13]. Metaheuristics can be defined as a guiding strategy in the search process of optimal solution by iteratively trying to improve a candidate solution with regard to a given measure of quality [WC13]. However, unlike exact optimization there is no guarantee that optimal solutions can be reached. Moreover, the proximity of the obtained solution from the optimal is not defined [Sia16; BLS13; Luk13; HMCS19].

Algorithms that are designed to solve a wide range of optimization problems without adapting heavily to each problem are called metaheuristic algorithms. Some advantages of metaheuristic algorithms are:

1. They are suitable for global optimization.
2. They allow restrictions to the solution space and introduction of prior information without using the classical regularization techniques.
3. No evaluation of objective function derivatives is needed.
4. No assumption on function continuity needs to be made.

However, heuristic algorithms are relatively expensive in terms of computing time and this limits their applicability to the field of difference imaging at present. Nevertheless, the continuous and rapid advancement of computing technology makes the development of real-time dynamic imaging applications based on metaheuristic methods conceivable in the near future.

Almost all metaheuristic algorithms are nature-inspired, that is, these algorithms are based on some principles from physics, biology, or ethology. They also often make use of stochastic components like random variables and they have several parameters that need to be fitted to the problem at hand. There are two contradicting criteria that must be considered in the design of metaheuristic algorithms: exploration of the search space and exploitation of best solutions found. A good balance between the exploration and the exploitation is the essence of the success of metaheuristic algorithms in optimization. Exploration allows an expanded search in a widespread domain. Exploitation limits parts of the search space to estimate the solution with higher precision. Metaheuristic algorithms can also be classified into population-based search or single-solution-based search. In single-solution based algorithms, an optimal solution is obtained by tweaking one solution during the search. These kinds of algorithms are exploitation oriented. Meanwhile, population-based search transforms the whole population of solutions and it is exploration oriented. It is also the most commonly used between the two [Luk13; Sia16].

The development of heuristic algorithms has experienced significant growth over the past two decades [HMCS19]. New algorithms, including improved variants of known methods, are continuously being proposed and applied to various real world problems. This is in part due to efforts directed at encouraging the creation of more advanced methods, including those of the IEEE Congress on Evolutionary Computation, and Black-Box Optimization Competition [MLH18]. Inspirations behind the methods are wide-ranging – from evolution, the behavior of animals, to physical processes. As such, the selection process of algorithms included in this study is an attempt to balance the diverse inspirations involved in developing the methods and the recency of such methods.

As pointed out, estimation of the conductivity distribution based on boundary voltages and electric currents is an ill-conditioned inverse problem. Minimizing the voltage error may then produce unsatisfactory results. Hence, reconstruction requires some methods of improving the conditioning so that the

wild variations causing the instability are ruled out. The most common method is regularization, which involves applying further assumptions and constraints based on *a priori* information. Typically, this means that the inverse problem is augmented with a side constraint such as the minimum length solution, the minimum error with respect to *a priori* solution, or the smoothness of the solution [Hol00]. The said assumptions and regularization techniques are not used in this thesis to show one of the advantages of metaheuristic algorithms over iterative methods.

In the following sections we present a comparative analysis of six heuristic algorithms - Firefly Algorithm (FA), Novel Bat Algorithm (NBA), Genetic Algorithm with New Multi-Parent Crossover (GA-MPC), Success History-based Adaptive Differential Evolution with Linear Population Size Reduction with Semi-Parameter Adaptation Hybrid with Covariance Matrix Adaptation Evolutionary Strategy (LSHADE-SPACMA), Ensemble Sinusoidal Differential Covariance Matrix Adaptation (LSHADE-cnEpSin), and Effective Butterfly Optimizer with Covariance Matrix Adapted Retreat Phase (EBOwithCMAR) - for the EIT image reconstruction problem. The next few sections discuss the said algorithms which are all variants of nature-inspired algorithms and population based.

### 4.2.2 FA

Firefly Algorithm (FA) belongs to the family of bio-inspired optimization techniques [Yan08]. It is a metaheuristic algorithm designed by Xin-She Yang in 2007 [Yan08]. FA is designed based from the behavior of fireflies in relation to their production of short and rhythmic flashes. The flashing light is produced by a process of bioluminescence and the pattern of flashes are often unique for a particular species of firefly. There are two fundamental functions of such signaling systems that are known: to attract mating partners (communication), and to attract potential prey. The rate of flashing and its duration form a part of the signal system that brings both sexes together. In the same species, the female fireflies respond to a male's unique pattern of flashing and this can be formulated as an objective function to an optimization problem. The fireflies will then search the solution space by moving to the position of their adjacent firefly that has better cost function value.

For the formulation of the algorithm, there are the three (idealized) assumptions:

1. All fireflies are unisex, that is, one firefly will be attracted to other fireflies regardless of their sex.
2. Attractiveness is proportional to their brightness.
3. The brightness of a firefly is determined by the landscape of the objective function.

It is also known that light intensity  $I$  at a particular distance  $r$  from the light source obeys the inverse square law and that air absorbs light which makes the light intensity weaker as the distance increases. With the addition of a fixed

light absorption coefficient  $\gamma$ , the light intensity can be approximated according to the inverse square law with the following Gaussian form

$$I(r) = I_0 e^{-\gamma r^2}.$$

From the assumption that firefly's attractiveness is proportional to the light intensity seen by adjacent fireflies, we have the attractiveness  $\beta$  be given by

$$\beta = \beta_0 e^{-\gamma r^2}.$$

Moreover, the distance between two fireflies  $i$  and  $j$  at positions  $x_i$  and  $x_j$ , respectively, is determined by the Cartesian distance. A firefly  $i$  will naturally move (is attracted) to the position of a more attractive (brighter) firefly  $j$  and the movement is described by

$$x_i = x_i + \beta_0 e^{-\gamma r^2} (x_j - x_i) + \alpha \epsilon_i,$$

where the second term is due to the attraction and the third term is a randomization with parameter  $\alpha$  and  $\epsilon_i$  is a vector of random numbers generated from a uniform distribution. Note that the parameter  $\gamma$  is the variation of the attractiveness and is crucial to the speed of convergence of FA. In practice, the value of  $\gamma$  varies from 0.1 to 10. The value of  $\alpha$  may also be adapted to improve the search/exploitation capability of the algorithm.

The algorithm starts with an initial population of virtual fireflies that is randomly generated. In each time step, the light intensity of each firefly is compared pairwise. In the standard FA, light intensity is determined by the objective function. If a firefly  $j$  has a greater light intensity than firefly  $i$ , the latter will fly towards the former. While the light intensity is referred to as an absolute measure of emitted light by the firefly, the attractiveness is a relative measure of the light that should be seen in the eyes of the beholders and judged by other fireflies [FFYB13]. The light intensities of the fireflies are then updated given the new positions. The fireflies' positions (solutions) are ranked and the current best solution is updated. A pseudo-code of FA is given in Appendix A.

Some applications of FA in the literature can be found in [YH13b; FFYB13; CLPM20]. Extensive simulations shown in [FFYB13] were carried out to compare the performance of FA with Particle Swarm Optimization and GA. Results showed that FA finds the global minima more efficiently and with higher success rate.

### 4.2.3 NBA

Bat Algorithm (BA), developed by Xin-She Yang in 2010 [Yan10], was inspired by the echolocation behavior of bats. One of the bat species, known as microbats, are famous for using echolocation extensively. Microbats use echolocation which is a type of sonar to detect prey, avoid obstacles, and locate their roosting crevices in the dark. They emit a very loud sound pulse and listen for the echo that bounces back from the surrounding objects. Moreover, microbats can detect the distance and orientation of the target, the type of prey, and even the

moving speed of the prey such as small insects. Studies also show that these bats are able to discriminate targets by the variations of the Doppler effect induced by the wing-flutter rates of the target insects. The echolocation behavior of microbats can be formulated in such a way that it can be associated with an objective function of an optimization problem. The current best solution is taken to be the prey/food and then the microbats will try to get closer to it [Yan10].

Just like in FA, the following are the approximate or idealized rules used for the design of BA: [Yan10]

1. All bats use echolocation to sense distance and also ‘know’ the difference between food/prey and background barriers in some way.
2. Bats fly randomly with velocity  $v_i$  at position  $x_i$  with a fixed frequency  $f_{\min}$ , varying wavelength  $\gamma$ , and loudness  $A_0$  to search for prey. They can automatically adjust the wavelength (or frequency) of their emitted pulses and adjust the rate of pulse emission  $r \in [0, 1]$ , depending on the proximity of their target.
3. Although the loudness can vary in many ways, we assume that the loudness varies from a large (positive)  $A_0$  to a minimum constant value  $A_{\min}$ .

BA starts with an initialization of  $N$  virtual bats represented by their positions  $x_i$  and velocities  $v_i$  in a  $D$ -dimensional search space. A current global best solution is then determined and a set of new solutions are generated using the minimum and maximum frequency. Meanwhile, a local search, where a new solution is generated around the current best, is invoked if a random number is bigger enough than the rate of pulse emission  $r$ . Lastly, the objective function values are ranked and solutions, loudness, and pulse emission rate are updated. The current global best solution is updated and the algorithm will continue until the stopping criterion is reached.

Novel bat algorithm (NBA) is a metaheuristic method proposed by Xian-Bing Meng et al. [MGLZ15]. NBA is one of the variants of the basic bat algorithm (BA). Now, the change in frequency of a (sound) wave when an observer moves relative to its source is called the Doppler Effect. Compared to the sound frequency itself, the received frequency is higher during the approach, identical at the instant of passing by, and lower during the recession. In the original BA, the microbats’ self-adaptive compensation for Doppler Effect in echoes is not accounted. Accounting Doppler Effect makes the modeling of the microbats’ echolocation ability more accurate. Moreover, the original BA did not consider the fact that bats hunt in a wide range of habitats. For these reasons, we employed NBA instead of the basic BA. NBA adds two more idealized rules:

1. All bats can forage in different habitats, depending on a stochastic selection.
2. All bats can compensate for Doppler effect in echoes. They can adaptively adjust the compensation rate according to the proximity of the targets.

Similarly in BA, NBA starts with a randomly generated population of bats, each bat is subjected to a selection of habitat/s where it will forage. This habitat selection is a stochastic decision such that, if a uniform random number in  $[0, 1]$  is smaller than the selection threshold, bat  $i$  will forage in a wide range of habitats; otherwise, it would hunt in limited habitats. If a randomly generated number is bigger than bat  $i$ 's pulse emission rate, a local search is performed by making the bat fly randomly around a certain neighborhood of the current best position (solution). If bat  $i$ 's new position is closer to the food than the current best, the rate of its pulse emissions is increased while the loudness is decreased. Finally, after looping through all the bats, the bats are ranked according to their proximity to the food, which is represented by their objective function values. If the best solution does not improve after a certain time steps, the loudness and pulse emission rates of the bats are re-initialized. The pseudo-code is given in Appendix A.

In [MGLZ15], the performance of NBA was tested under twenty optimization problems and four real-world engineering designs. Simulations showed that NBA is effective, efficient, stable, and superior over some well-known algorithms such as the original BA, Particle Swarm Optimization, Flower Pollination Algorithm, and even DE. A wide range of applications of this algorithm are briefly summarized in [YH13a].

#### 4.2.4 GA-MPC

Genetic Algorithm or GA belongs to a set of algorithms called Evolutionary Algorithms (EA). EAs are population methods in which a sample of candidate solutions are considered instead of a single candidate solution. Note that we call a candidate solution, an individual and a set of candidate solutions, a population. In EA, each of the individuals affect how other candidates will improve in the quality function, that is, rejecting poor solutions and creating new ones by adjusting the good solutions to the direction of better ones. EAs are divided into two kinds: generation-based algorithms which update the entire sample once per iterations and steady-state algorithms which update the sample a few candidates at a time. GA is among the latter kind.

GA was first proposed by John Holland in 1975 [Hol75] and it is originally based on the Darwinian principle of evolution. GA as a population method iterates through fitness assessment, selection and breeding, and population re-assembly. A cycle of the said steps is called a generation. Fitness assessment is the computation of quality function value of an individual. Selection is the process of picking candidate solutions based on their fitness while breeding is the production of one or more children from a population through an iterated process of selection and tweaking. The plain tweaking of an individual (asexual breeding) is called mutation and recombination or crossover is a special tweaking (sexual breeding) involving two candidate solutions (parents) to produce two children.

The first step in GA or in any EAs is the population initialization. Here, some  $n$  individuals are created at random in which we ensure that every individual is unique. If likely initial "good" regions of the space are known, then we can

tend to generate individuals in those regions. Next is the breeding in which we begin with an empty population of children. In the fitness-based selection, the more fit members, called parents, of the population are selected. The selected members are then recombined to form members of the successor population. Recombination has two components: crossover operator and mutation operator. *Crossover* is the mixing and the matching of parts of two parents to form children. Its development was based on the premise that highly-fit individuals share certain traits in common and that there is some degree of linkage between genes (particular slot/element in vector). *Mutation* in GA is usually done using the *Gaussian convolution*. In this process, a random noise under a Gaussian distribution, with a mean  $\mu = 0$  and variance  $\sigma^2$ , is added to each number in the vector. The variance is chosen according to the degree of emphasizing small numbers over large ones. The noise should be small to finesse local peaks and large enough to escape local optimal. Furthermore, *Tournament Selection* is the primary selection technique used in GA. It picks the fittest individual of some  $t$  (most popular setting is 2) individuals picked at random, with replacement, from the population. GA is one of the most popular heuristic algorithms and has been applied to different problems in science and engineering. For the discussion of some of the applications of GA, we refer the readers to [McC05; MM17]. A typical design for a classical GA would be as follows:

1. population initialization with size  $P$ ,
2. fitness assessment and choosing the best solution,
3. for  $P/2$  times apply a tournament selection to select two parents and produce two children using linear recombination, and mutate the resulting children,
4. the new population to be considered is the pool of children,
5. repeat steps until the best solution is the ideal solution or the maximum number of iterations has been reached.

The above description is the general form of GA. One variation of GA involves directly injecting into the next population the fittest individual(s) from the previous population. This version of GA is called elitism and the chosen individuals are called elites. With elitism, the solution quality obtained by the algorithm will not decrease from one generation to the next.

In this study, GA-MPC, a variant of GA that proposes a new crossover method, and randomized operation in lieu of mutation, is considered [ESE11]. Unlike GA's original formulation, GA-MPC creates an archive pool where the best  $m$  individuals are stored, and a selection pool with size  $tc$ , chosen randomly, for successful individuals from the tournament selection. Individuals in the selection pool are used for performing multi-parent crossover.

Multi-parent crossover (MPC) uses three parents, randomly selected in the selection pool but should be unique, to produce three children: two are designed for exploitation, the other for exploration. The selected parents are then ranked based on their fitness (best  $-x_1, x_2, x_3$ — worst). A random number  $\beta$  from

Gaussian distribution with mean value  $\mu$  and variance  $\sigma^2$  is generated next. The children produced in MPC has the following form:

$$\begin{aligned} o_1 &= x_1 + \beta(x_2 - x_3) && \text{(exploitation)} \\ o_2 &= x_2 + \beta(x_3 - x_1) && \text{(exploration)} \\ o_3 &= x_3 + \beta(x_1 - x_2) && \text{(exploitation)} \end{aligned}$$

GA-MPC also proposed a randomized vector to diversify (mutate) the generated offsprings and escape any local minimum. An  $i$ th element of the offspring vector is replaced, with probability  $p$ , by the  $i$ th element of an individual selected at random from the pool of  $m$  best solutions. Individuals in the archive pool are then merged with all of the offsprings, where the worst individuals are removed from the population. The surviving population are then carried over to the next generation. The pseudo-code is given in Appendix A.

In [ESE11], GA-MPC was tested using the real-world numerical optimization problems of the IEEE CEC 2011 Real-World Numerical Optimization Special Session [DS10], and ranked first among fourteen participating algorithms [MLH18].

#### 4.2.5 EBOwithCMAR

Butterfly Optimizer (BO) is inspired from the mate-locating behavior of male butterflies [KMS15]. BO optimizes a problem by using two main mate-locating behaviors, perching and patrolling, to update the position of male butterflies (trial vectors). A perching male sits on a location and persistently contemplates the nearby objects, but a patrolling male doesn't sit on any location and explores its mate by flying in different location. Hence, the method performs a search space exploration by the patrolling behavior of the male butterflies and search space exploitation by the perching behavior. On the other hand, butterflies have compound eyes that are able to see all around the space and they use this vision in mate-locating. Also, since reflective capability of male's and female's wings are different from each other, they can easily identify each other. Moreover, wings of both butterfly are capable of generating ultra-violet rays and the attractiveness of these rays are dependent on the location of the butterflies. Hence, the attractiveness can be related to an objective function.

BO starts with two randomly generated populations, the population of male butterflies and the auxiliary butterflies. After initialization, male butterflies start searching for female butterfly for mating by perching. Auxiliary butterflies are not adult male butterflies and so, they do not seek for female butterflies. They will be used for the perching of the main (male) butterflies. If after perching the position of the main butterfly is not updated, it will switch to patrolling where it will move in memorized direction. These processes are repeated until convergence is achieved, that is, the male butterfly found its mate.

Effective Butterfly Optimizer (EBO) is a variant of BO where a crossover operator is added in the perching and patrolling processes to further diversify the population [KMS15]. EBO also starts with two sub-populations; main and auxiliary butterflies. Next is a new set of vectors (mutated vectors) is generated

from the main population and then, a binomial crossover is done between the mutated vectors and the main population to obtain a set of trial vectors. During perching, the mutated vectors is generated using crisscross modification, and toward-best modification is used for patrolling. Lastly, objective function values of the original main population is compared to their corresponding trial vectors, and the better one is taken as a member of new main population. The other vector is selected for the secondary population.

In Covariance Matrix Adapted Retreat (CMAR), new solutions are sampled in search space using the given random distribution represented by its corresponding mean and covariance matrix [Han06; KMS17]. The fitness values of these new solutions are then compared and based on these values, a subset of individuals from the sampled space are selected. A new mean and covariance matrix for the random distribution will be calculated from this subset.

Now, EBOwithCMAR is a hybrid algorithm that combines the characters of global optimizer and a local optimizer [KMS17]. It starts with a randomly generated population that is divided into three sub-populations, where the first and second populations are used for EBO, and the last one is for CMAR. Two probabilities are defined to decide which specific algorithm is to be applied at a particular iteration. In this algorithm, a fixed number of iterations called cycles are defined. At the start of a cycle until to its half, both the probabilities are equal to 1 and so, both EBO and CMAR are running in parallel. After the half of a cycle, new values of the probabilities are obtained and the update is based on the superiority of the solution determined by EBO and CMAR and the diversity of their corresponding (main) populations. Once the cycle is over, a data sharing system is implemented where the worse solution(s) in the population of the inferior algorithm is replaced by best solution(s) of the better algorithm. If EBO is the better algorithm, the population dedicated to CMAR is replaced by a random element from the main population of EBO. On the other hand, if CMAR is the better algorithm, the worst individual in the main population of EBO is replaced by the best individual from the population dedicated to CMAR. Furthermore, the Sequential Quadratic Programming (SQP) is implemented when 75% of the optimization process is done. This is to improve the exploitation potential of EBOwithCMAR. The proposed algorithm is further improved by modifying EBO using the Success History Based Adaptation to adapt the parameters for the crossover, and a linear reduction for the sizes of the two sub-populations [TF14]. Finally, the algorithm will continue until the stopping criterion is reached. The pseudo-code is given in Appendix A.

In [KMS17], EBOwithCMAR was evaluated using the set of problems presented in IEEE CEC 2017 Real-Parameter Special Session bound constrained case [AALQS16], where it ranked first out of the twelve participating algorithms [MLH18].

### 4.2.6 Differential Evolution variants

Differential Evolution or DE is a variation of evolutionary computation designed to deal with multi-dimensional real-valued spaces. There are two modifications that are introduced in DE, the first one is that the children produced in the

breeding stage must compete directly against their immediate parents for the inclusion in the population. Second is that DE is designed to be an adaptive mutation algorithm, that is, the size of mutates is based on the current variance in the population. This means that if the population is spread out, mutates make big changes and small changes if the population is condensed. DE's evolutionary processes are similar to other evolutionary algorithms; mutations, crossover, and selection operators are done at each generation to reach the global optimum. The population space is a set of individuals generated uniformly within the range of the decision variables. Using mutation and crossover operators, trial vectors are generated and compared to target vectors and the best individuals are selected for the next generation. These steps are repeated until the stopping criterion is reached.

Some advantages of DE are its ease of implementation, reliability, speed, and robustness. However, even if DE has a good global exploration ability, it is slow at exploitation of the solution. DE's performance also deteriorates as the dimensionality of the problem increases and when the problem has premature convergence or stagnation occurs. Moreover, it is widely known that the performance of DE is highly dependent on the choice of parameter settings for its control parameters. There are three control parameters that play a vital role in balancing the diversity of the population and convergence speed of DE: the scaling factor ( $F$ ), the crossover rate ( $Cr$ ), and the population size  $PS$ . The parameter  $F$  controls the evolving rate of the population which is closely related to the speed of convergence. In particular, a small value of  $F$  improves the exploitation tendency of the algorithm while a large value enhances its exploration capability. For the constant crossover  $Cr$ , it is the probability with which the genes of the actual individuals is inherited by the trial individual, that is, the number of components and which components are mutated for each individual in the current population. It practically controls the diversity of the population and is more sensitive to the nature of the problem.

Currently, there is a huge progress in the study of improvements of DE and its diverse applications [DMS16]. There are a lot of variants of DE that focuses on the adaptation of these parameters. These variations are divided into two main groups: One group focuses on the random selection of parameter values from random distributions such as normal, uniform, and Cauchy distributions or changing with the progress of generations using increasing/decreasing linear or nonlinear deterministic functions. The other group focuses on adaptive or self-adaptive adjustments of control parameters. A particular variant of DE where it uses a new mutation strategy "current/to/ $p$ best" with an optional external archive and updates the control parameters in adaptive manner using Cauchy and normal distributions, is initially proposed in JADE [ZS09].

Meanwhile, Success History-based DE (SHADE) algorithm is an improved variant of the JADE algorithm [ZS09; TF13]. SHADE uses historical memory archives  $M_{Cr}$  and  $M_F$ , both of size  $H$  and in which a set of  $Cr$  and  $F$  values that have performed well in the past generations are stored. New  $Cr$  and  $F$  values are generated by selecting a random index from the memory archives to choose the mean values  $\mu_{Cr}$  and  $\mu_F$  for their respective random distributions. Lastly, the LSHADE algorithm is an extension of the SHADE algorithm

[TF13; TF14]. LSHADE adds the linear reduction of the population size, from the maximum population size  $PS_{\max}$  to the minimum  $PS_{\min}$ , at each generation [TF14]. LSHADE employs the “current/to/ $p$ best” mutation strategy, where one of the top  $p$  best individuals is used to guide the evolutionary search, to produce mutant vectors. The resulting mutant vector is then mixed with the target vector (parent) to produce a trial vector (child). In DE, a greedy selection technique is implemented where the trial vector is compared to the target vector and the better vector survives for the next generation. Both Success History-based Adaptive Differential Evolution with Linear Population Size Reduction with Semi-Parameter Adaptation Hybrid with Covariance Matrix Adaptation Evolutionary Strategy (LSHADE-SPACMA) and Ensemble Sinusoidal Differential Covariance Matrix Adaptation (LSHADE-cnEpSin) are based on the LSHADE algorithm and in which they add additional approaches to enhance LSHADE.

### LSHADE-SPACMA

LSHADE-SPACMA proposes a new semi-parameter adaptation approach which consists of two different settings for two control parameters  $Cr$  and  $F$  [MHFJ17]. The first setting is implemented for the first half of fitness evaluations and it is done by using LSHADE adaptation for  $Cr$  only while  $F$  is randomly generated from uniform distribution. While the second setting is for the second half of fitness evaluations and the LSHADE adaptation is used for both  $Cr$  and  $F$ . The semi-adaptation approach is proposed because semi-adaptive algorithm performed relatively better than pure random algorithm or fully-adaptive algorithm [MHFJ17]. Since pure random algorithms cannot solve efficiently the problem within limited number of function evaluations while fully-adaptive algorithm provides no guarantee of escaping local solutions or avoid stagnation [MHFJ17].

Covariance Matrix Adaptation - Evolutionary Strategy (CMA-ES) is another algorithm that adapts the multi-variate normal distribution [Han06]. It generates new individuals using Gaussian distribution considering the path the population takes over generations. As an evolution-inspired algorithm, CMA-ES steps are very similar to that of DE [PSL05] and GA [Hol75]. It starts with an initial “population” of search points sampled from the initial multi-variate normal distribution; followed by selection and recombination to update the mean; step size control to update the evolution path; and covariance matrix adaptation [Han06].

Finally, LSHADE-SPACMA implements a hybridization framework between LSHADE and a modified version of CMA-ES. Each individual in the population will generate an offspring using either LSHADE or CMA-ES algorithm. The method is chosen according to class probability variable ( $FCP$ ), which are randomly selected from memory slots  $M_{FCP}$ . The memory is updated according to the performance of each algorithm at the end of each generation which will lead to more populations being assigned to the better performance algorithm. However, to maintain both algorithms,  $FCP$  values are kept in range between 0.2 and 0.8. The pseudo-code is given in Appendix A.

In [MHFJ17], LSHADE-SPACMA was evaluated using the set of problems presented in IEEE CEC 2017 Real-Parameter Special Session bound constrained

case [AALQS16], where it ranked fourth out of the twelve participating algorithms [MLH18].

### LSHADE-cnEpSin

LSHADE-cnEpSin also follow the DE-based algorithm, LSHADE, but with an additional method for adapting the parameters of DE. The additional parameter adaptation method is an ensemble sinusoidal differential covariance matrix adaptation with Euclidean neighborhood. The sinusoidal adjustment adapts the scaling factor  $F$  while the other method is for the crossover rate  $Cr$  [AAS17]. LSHADE-cnEpSin employs an ensemble of two sinusoidal waves to adapt the scaling factor  $F$  based on successful performance of previous generations. The two configurations are the *non-adaptive sinusoidal decreasing adjustment* and the *adaptive sinusoidal increasing adjustment* [AASR16; AAS17]. For the first half of generations, a mixture of the two sinusoidal configurations based on performance adaptation is used. During the said period, a learning period  $LP$  is introduced where the probabilities of choosing sinusoidal configurations are both equal to 0.5 and are chosen randomly [AAS17]. After that, the probabilities are updated at each subsequent generation according to the respective performance of the sinusoidal configurations. Now for the second half of generations, the usual formulation of SHADE [TF13] in adapting the scaling factor  $F$ , using Cauchy distributions, is used [AAS17].

LSHADE-cnEpSin, although shares the same adaptation process for the crossover rate  $Cr$  with LSHADE [TF14], adds another crossover operator using covariance matrix learning with Euclidean neighborhood with a probability  $pc$  [AAS17]. In this step, the best individual in the population is determined and the Euclidean distance between the best individual and every other individual in the population is computed. The individuals are then sorted based on their Euclidean distance and a number of individuals are chosen to form a neighborhood around the best individual. The covariance matrix is computed from this neighborhood region and after that, the target and mutant vectors are updated with respect to the Eigen coordinate system. The trial vector is created using the binomial crossover and is then transformed back to the original coordinate system. The pseudo-code is given in Appendix A.

In [AAS17], LSHADE-cnEpSin was evaluated using the set of problems presented in IEEE CEC 2017 Real-Parameter Special Session bound constrained case [AALQS16], where it ranked third out of the twelve participating algorithms [MLH18].

## 4.3 Numerical simulations

Series of numerical tests were carried out to investigate and compare the performance of the proposed algorithms in solving the inverse EIT problem. Three different cases of inclusions were considered as shown in Table 4.1 and mentioned in Section 2.4.

### 4.3.1 Presentation of the test configurations

We consider three different cases (see Table 4.1). We consider Case 1 in this chapter to be the same domain in Case 3a in Chapter 2 (p. 29) which is a CT scan of a thorax domain, but with known background conductivity  $\sigma_0 = 6.7 \text{ mS} \cdot \text{cm}^{-1}$ . For the numerical simulations of this case, the geometry is fixed, and only the conductivity values inside the inclusions,  $\sigma_l$  and  $\sigma_h$ , are unknown. Indeed, the CT results already give the location and the geometry of the organs. We are only interested in determining the conductivity values of the inclusions (i.e. lungs and heart). This method is particularly applicable for lung or heart function monitoring to check if there is a deviation of the estimated conductivity values from the normal values.

Case	Unknown Variables
1	$\sigma_l, \sigma_h$ (geometry is fixed)
2	$\sigma_e, h, k, a, b, \theta$
3	$\sigma_1, \sigma_2, h_1, k_1, h_2, k_2, a_1, b_1, a_2, b_2, \theta_1, \theta_2$

TABLE 4.1: Different cases studied for the numerical tests

For Case 2 in this chapter, we study the same geometry as in Case 1b in Chapter 2 (p. 28). In this case, six parameters are unknown, that is,  $\sigma_e$  is the conductivity of the inclusion,  $(h, k)$  is the center of the ellipse,  $a$  and  $b$  are the lengths of the major and minor axes, respectively, and  $\theta$  is the angle of rotation. In Case 3, we aim in reconstructing two disjoint elliptical inclusions and the respective conductivities inside, i.e., 12 unknown parameters;  $\sigma_1, \sigma_2, h_1, h_2, k_1, k_2, a_1, a_2, b_1, b_2, \theta_1, \theta_2$ . The conductivity  $\sigma_0$  of the background medium for both the second and third case is  $1.0 \text{ mS} \cdot \text{cm}^{-1}$ . All cases may represent the domains used in the application of EIT for brain or breast tumour detection.

We work with synthetic data. In Case 1, the data is generated with conductivity of the lungs and the heart equal to  $1.0 \text{ mS} \cdot \text{cm}^{-1}$  and  $6.3 \text{ mS} \cdot \text{cm}^{-1}$ , respectively. The conductivity of the elliptical inclusion is taken to be  $6.7 \text{ mS} \cdot \text{cm}^{-1}$  for the inversion data for Case 2. The generated data for Case 1 is from the case where we take the conductivity of the smaller ellipse to be  $6.7 \text{ mS} \cdot \text{cm}^{-1}$  and the bigger one to be  $6.1 \text{ mS} \cdot \text{cm}^{-1}$ . We take  $L = 32$  electrodes. The contact impedance is constant across the  $L$  electrodes and it is equal to  $0.03 \text{ ohm} \cdot \text{cm}^2$ . Sixteen current patterns are applied on the electrodes and the first current has the form

$$I^1 = \{I_\ell^1\}_{\ell=0}^{L-1}, \text{ with } I_\ell = \sin\left(\frac{2\pi\ell}{L}\right). \quad (4.5)$$

The remaining fifteen current patterns are obtained by ‘rotating’ the values of the first current pattern, that is, to get the second current pattern  $I^2$ , we have  $I^2(0) = I^1(L-1)$ ,  $I^2(1 : L/2) = I^1(0 : L/2 - 1)$ , and  $I^2(L/2 + 1 : L-1) = I^1(L/2 : L-2)$ . This is repeated until we obtain the fifteen additional current patterns. The synthetic voltage data  $(u, U)$  are obtained by solving the forward CEM problem (1.21) – (1.22) – (1.23) – (1.24) with the exact conductivity

distribution (2.30). A FEM mesh structure with 30 240 triangular elements, 15 409 nodes, and a mesh size  $h = 0.014$  was used for the resolution of the forward problem in Case 1, and with 25 858 triangular elements, 13 122 nodes, and  $h = 0.03$  for both Cases 2 and 3. In order to avoid an *inverse crime* (in the sense of [CK98; Wir04]), the inverse computations are done on a mesh with 17 240 triangular elements, 8 845 nodes, and  $h = 0.019$  for Case 1, and on a mesh with 17 882 triangular elements, 9 102 nodes, and  $h = 0.037$  mesh size for Cases 2 and 3, which are different from the meshes used to solve the forward problems.

To model possible experimental errors, a 1% random (additive) noise is added to the voltage data as  $U_{\text{data}} = (1 + 0.01 * \text{rand}(L))U$ , where  $\text{rand}(L)$  gives a vector of length  $L$  where each element is a uniformly distributed random number in the interval  $[-1, 1]$  (see [HL08]). In our simulations, one noise seed is composed of sixteen different noise vectors added to the corresponding sixteen current-voltage measurements.

### 4.3.2 Parameter setting for the heuristic methods

The study is based on 20 independent runs of each proposed algorithm, with the same noise seed for all the runs, and a stopping criterion based on a predefined number of function evaluations. The only stopping criterion used for all the heuristic methods is when the maximum number of function evaluations is reached. In particular for Case 1, we set the maximum number of function evaluations to 1000 and in Cases 2 and 3, we have  $1000 * D$  function evaluations with  $D$  as the number of unknown parameters.

The search space was restricted differently for each case. In Case 1, the bounds are given by  $\mathbf{x}_{\min} = [0, 0]$  and  $\mathbf{x}_{\max} = [10, 10]$ . Case 2 has bounds  $\mathbf{x}_{\min} = [5, -1, -1, 0, 0, 0]$  and  $\mathbf{x}_{\max} = [9, 1, 1, 2, 2, \pi]$ . For Case 3, we fix  $\mathbf{x}_{\min} = [5, -1, -1, 0, 0, 0, 5, -1, -1, 0, 0, 0]$  and  $\mathbf{x}_{\max} = [9, 1, 1, 4, 4, \pi, 9, 1, 1, 4, 4, \pi]$ . We implemented the numerical solver for the forward problem with FreeFem++ [Hec12] with mesh information given in Section 2.4.2. The numerical optimization algorithms were implemented in Matlab R2018a.

The different parameters used in all the algorithms are set to values in their original formulation. In particular, the default values in the main papers cited in Section 4.2 for each algorithm are chosen, unless certain configurations need to be made to address issues, such as algorithmic complexity. The lack of parameter tuning to fit the EIT problem in conducting the numerical simulations is intended to ensure that the study does not favor any algorithm, which allows for a thorough comparison of the original methods.

Parameters for FA were set as follows:  $\alpha_0 = 0.2$ ,  $\gamma = 1$ , and  $\beta = 0.2$ , where  $\alpha_0$  is the initial randomization parameter,  $\gamma$  is the light absorption coefficient, and  $\beta$  is the base attraction coefficient. The population size in each generation for FA varies for each case, Case 1 has 20 fireflies, Case 2 has 30, and Case 3 has 60. Each firefly would require the computation of the cost functional (4.4), which is expensive and accounts for the major running time of the algorithm.

In Table 4.2, the parameter settings for NBA are enumerated:  $r$ ,  $f$ , and  $A$  denote the rate, frequency, and loudness of sound pulses emitted by bats,

$r_{\min}$	0	$\alpha$	0.9
$r_{\max}$	1	$P_{\min}$	0.6
$f_{\min}$	0	$P_{\max}$	0.9
$f_{\max}$	1.5	$C_{\min}$	0.1
$A_{\min}$	1	$C_{\max}$	0.9
$A_{\max}$	2	$G$	10
$\gamma$	0.9		

TABLE 4.2: Selected values for NBA parameters

respectively.  $P$  denotes the probability of habitat selection, while  $C$  denotes the compensation rate for Doppler effect in echoes. The constants  $\gamma$  and  $\alpha$  are used to update  $r$  and  $A$ . The parameters  $r$  and  $A$  are re-initialized if the best solution does not change after  $G$  time steps. Meanwhile, the contraction-expansion coefficient  $\theta$  and the inertia weight  $w$  are adjusted according to the parameter control method described in [TLPSX11], i.e., using  $a \cdot \cos\left(\frac{\pi t}{2M}\right) + a$ , where  $t$  is the current time step, and  $a = 0.5$  for  $\theta$  while  $a = 0.4$  for  $w$ . While  $\tilde{M}$  is defined to be the maximum number of time steps in [TLPSX11], in this work, we set its value to be positive infinity.

Parameters for GA-MPC were set as follows: population size  $PS = 90$ , ‘‘crossover factor’’  $\beta \sim \mathcal{N}(0.5, 0.3)$ , crossover rate  $cr = 1$ , tournament selection size generated randomly between 2 and 3, and archive pool size  $|A| = 45$  (half of the population size) [ESE11].

LSHADE-SPACMA and LSHADE-cnEpSin share several parameter values: initial population size  $PS_{max} = 18 * D$  and minimum population size  $PS_{min} = 4$  as both algorithms implement a linear population size reduction, initial values for  $M_{Cr}$ ,  $M_F$  at 0.5, factor that controls the greediness of the mutation strategy  $p_{best} = 0.11$ , archive rate  $Arc_{rate} = 1.4$ , and memory size  $H = 5$  used in storing adapted parameters [MHFJ17; AAS17]. Parameter settings specific to LSHADE-SPACMA are as follows: initial value for  $M_{FCP} = 0.5$  used in the hybridization framework, and learning rate  $c = 0.8$  used in updating the probability for hybridization [MHFJ17]; while the parameter specific to LSHADE-cnEpSin used for the non-adaptive sinusoidal decreasing adjustment  $freq$  is set to 0.5 [AAS17].

EBOwithCMAR uses the following parameter values: for EBO, it uses the same initial population size  $PS_{1,max} = 18 * D$ , minimum population size  $PS_{1,min} = 4$  for  $PS_1$  with LSHADE-SPACMA and LSHADE-cnEpSin [MHFJ17; AAS17],  $PS_{2,max} = 46.8 * D$ ,  $PS_{2,min} = 10$ , and memory size  $H = 6$ ; while for CMAR,  $PS_3 = 4 + 3 \log(D)$ ,  $\tilde{\sigma} = 0.03$ , number of evaluations constituting a cycle  $CS = 50$ , and local search update probability  $prob_{ls} = 0.1$  [KMS17].

### 4.3.3 Numerical comparison and discussions

The comparative analysis of the heuristic methods is done by measuring the accuracy and precision of the solutions generated, together with their respective

average costs. This is because the inverse EIT problem is ill-conditioned, which means that solutions tend to be extremely sensitive to perturbations, potentially making them inaccurate or unstable. To quantitatively analyze the accuracy of recovered images, the average of the reconstruction errors for 20 runs of each algorithm was calculated and will be referred to as the “mean error”, for simplicity. For the  $i^{\text{th}}$  run, the relative reconstruction error is given by:

$$RE = \frac{\|\hat{y}_i - y_{\text{true}}\|_2}{\|y_{\text{true}}\|_2}, \quad (4.6)$$

where  $\|\cdot\|_2$  is the Euclidean norm,  $\hat{y}_i$  is a vector containing the values estimated by the algorithm at the  $i^{\text{th}}$  run, whereas  $y_{\text{true}}$  contains the true values. Based from Table 4.1,  $\hat{y}_i$  and  $y_{\text{true}}$  are vectors in  $\mathbb{R}^2$  for Case 1, in  $\mathbb{R}^6$  for Case 2, and in  $\mathbb{R}^{12}$  for Case 3.

In order to measure the repeatability (reconstruction accuracy) of each algorithm, that is, the degree to which the algorithm produced the similar results for 20 runs, the standard deviation (St. Dev.) of the reconstruction errors was also determined. Table 4.4 compares the accuracy, repeatability, and average costs of each algorithm’s reconstructions for Cases 1, 2, and 3, respectively. The mean and standard deviation of the reconstruction errors of the generated solutions in the 20 independent runs is computed using the *mean* and *std* functions in Matlab.

Algorithm	Case 1	Case 2	Case 3
FA	5.28	6.82	16.56
NBA	0.152	<b>2.28</b>	21.91
GA-MPC	<b>0.054</b>	15.11	13.07
LSHADE-SPACMA	0.060	5.84	<b>7.90</b>
LSHADE-cnEpSin	0.061	9.63	14.95
EBOwithCMAR	0.058	6.43	12.00

TABLE 4.3: Reconstruction errors in % of the final solution generated by the proposed heuristic algorithms for all cases.

In all the cases, the final solution or final reconstructed parameter values considered for each algorithm is the average solution of the 20 runs. Figures 4.1, 4.2, and 4.3 show the final solution of each algorithm for Cases 1, 2, and 3, respectively. Note that we fixed the range of the conductivities in the plots and so the difference in color of the solutions from the original image signifies how far is the approximate solution from the true solution. Table 4.3 shows the relative reconstruction error in % of the final solution of each algorithm for the three cases, while Tables 4.5, 4.7, and 4.9 display the reconstruction error in % of each unknown parameter for Case 1, 2, and 3, respectively. The results shown in black bold characters indicate the best values.

For Case 1, all the heuristic algorithms studied were very successful in the recovery of the conductivity values of the inclusions in  $\Omega$ . Table 4.5 displays

Case 1 - Thorax			
Algorithm	Mean Error	St. dev.	Average cost
FA	5.54E-02	7.77E-02	1.4E-03
NBA	7.74E-03	4.64E-03	1.4E-03
GA-MPC	2.23E-03	1.94E-03	1.4E-03
LSHADE-SPACMA	<b>6.08E-04</b>	<b>7.26E-08</b>	1.4E-03
LSHADE-cnEpSin	6.15E-04	4.32E-05	1.4E-03
EBOwithCMAR	6.10E-04	8.24E-05	1.4E-03
Case 2 - One elliptical inclusion			
Algorithm	Mean Error	St. dev.	Average cost
FA	0.2193	0.1046	0.6115
NBA	0.1742	0.0983	0.2562
GA-MPC	0.1527	0.0554	0.2422
LSHADE-SPACMA	0.1143	<b>0.0385</b>	<b>0.2407</b>
LSHADE-cnEpSin	0.1251	0.0762	0.2423
EBOwithCMAR	<b>0.0827</b>	0.0693	0.2426
Case 3 - Two elliptical inclusions			
Algorithm	Mean Error	St. dev.	Average cost
FA	0.3071	0.0717	2.8463
NBA	0.3435	0.0926	1.9620
GA-MPC	0.1790	<b>0.0530</b>	0.2558
LSHADE-SPACMA	<b>0.1546</b>	0.0674	<b>0.2165</b>
LSHADE-cnEpSin	0.2033	0.0675	0.2219
EBOwithCMAR	0.1988	0.0685	0.2917

TABLE 4.4: Comparison of accuracy, repeatability, and average cost of the solutions generated by the proposed heuristic algorithms for all cases.

the final values and the reconstruction error in % of each unknown parameter for Case 1. Except for FA, the rest of the algorithms lead to a reconstruction error around 0.1%. The conductivity of the heart is better retrieved than the lungs for the more recent heuristic algorithms, while for FA and NBA, the lungs' conductivity is approximated more accurately. LSHADE-SPACMA got the least mean and standard deviation of reconstruction error which means that

Case 1 - Thorax				
	Estimated values		Error in %	
Algorithm	$\sigma_\ell$	$\sigma_h$	$\sigma_\ell$	$\sigma_h$
True solution	1.0	6.3		
FA	1.0119	5.9631	1.19E-02	5.34E-02
NBA	1.0037	6.2910	3.69E-03	1.42E-03
GA-MPC	1.0031	6.30158	<b>3.09E-03</b>	<b>2.51E-04</b>
LSHADE-SPACMA	1.0032	6.3022	3.18E-03	3.43E-04
LSHADE-cnEpSin	1.0032	6.3023	3.18E-03	3.62E-04
EBOwithCMAR	1.0032	6.3019	3.19E-03	3.06E-04

TABLE 4.5: Final solutions and reconstruction errors in % of each parameters in the final solution generated by the proposed heuristic algorithms for Case 1.

this method is the best in terms of consistency and accuracy of the approximate solution for each run. Almost all the algorithms obtained the same average cost which implies that all methods converge to the true solution. Lastly, GAMPC is the most accurate and the three most recent algorithms, LSHADE-SPACMA, LSHADE-cnEpSin, and EBOwithCMAR got around the same relative errors for the final solution.

Case 2 - One elliptical inclusion						
Algorithm	$\sigma_1$	$h$	$k$	$a$	$b$	$\theta$
True solution	6.7	-0.4	0.5	0.4	0.7	$3\pi/8$
FA	7.0536	-0.4107	0.5103	0.4704	0.9898	1.1030
NBA	<b>6.8298</b>	<b>-0.4027</b>	0.5020	0.4294	<b>0.7151</b>	1.2596
GA-MPC	5.6615	-0.4050	0.5022	0.3810	0.7170	1.2260
LSHADE-SPACMA	7.0970	-0.4058	<b>0.4996</b>	0.4160	0.7606	<b>1.1821</b>
LSHADE-cnEpSin	6.0394	-0.4048	0.5011	0.3919	0.7260	1.2246
EBOwithCMAR	6.2613	-0.4045	0.5007	<b>0.3996</b>	0.7319	1.2277

TABLE 4.6: Final solutions generated by the proposed heuristic algorithms for Case 2.(Note that  $3\pi/8 \approx 1.18$ .)

For Case 2, all the heuristic algorithms studied well retrieved the center of the ellipse (see Tables 4.7, 4.6). The difference of performance between them lies in the estimation of both the conductivity and the geometric parameters. EBOwithCMAR performed the best while getting the least mean error and relatively small average cost. LSHADE-SPACMA got the smallest standard

Case 2 - One elliptical inclusion						
Algorithm	$\sigma_e$	$h$	$k$	$a$	$b$	$\theta$
FA	5.28	2.68	2.06	17.61	41.40	6.37
NBA	<b>1.94</b>	<b>0.68</b>	0.41	7.34	<b>2.15</b>	6.92
GA-MPC	15.50	1.26	0.43	4.76	2.43	4.07
LSHADE-SPACMA	5.92	1.46	<b>0.07</b>	4.00	8.65	<b>0.34</b>
LSHADE-cnEpSin	9.86	1.20	0.22	2.03	3.72	3.95
EBOwithCMAR	6.55	1.13	0.14	<b>0.09</b>	4.56	4.21

TABLE 4.7: Reconstruction errors in % of each parameters in the final solution generated by the proposed heuristic algorithms for Case 2.

deviation and average cost. As expected, because of the low resolution property of EIT, the estimate for the conductivity value inside the inclusion is not as accurate as the approximation of the geometry. Nevertheless, NBA provided an excellent approximation of the conductivity (error 1.94%) while FA, LSHADE-SPACMA, and EBOwithCMAR were still able to obtain good conductivity value estimates (see Table 4.7). GA-MPC yielded the least accurate conductivity estimate which justifies the relative error given in Table 4.3. This means that GA-MPC finds it hard to balance its exploration and exploitation when approximating both the geometry of the inclusion and the conductivity inside it. NBA and the three most recent algorithms (namely LSHADE-SPACMA, EBOwithCMAR and LSHADE-cnEpSin) presented impressive reconstructions (see Figure 4.2). FA is the less efficient. Lastly, NBA offered the best relative error of the final solution.

Tables 4.8 and 4.9 give the final values and the reconstruction error in % of each unknown parameter for Case 3. For Case 3, LSHADE-SPACMA showed the best performance with the least mean error and average cost while GA-MPC is the most consistent among the algorithm because it obtained the least standard deviation of the reconstruction error. The recovered images of LSHADE-SPACMA and LSHADE-cnEpSin are the closest ones to the original image. GA-MPC and EBOwithCMAR were also able to reconstruct the two inclusions. NBA only obtained a not too bad location of the bigger inclusion but failed to reconstruct the smaller ellipse. FA gave a poor reconstruction of both inclusions. For the estimation of conductivity values inside the inclusions, LSHADE-SPACMA achieved a good balance in the estimation of the conductivities, EBOwithCMAR yielded the most accurate estimate for the conductivity in the smaller inclusion, and LSHADE-SPACMA got the best conductivity estimate for the bigger inclusion. NBA is the least accurate in the estimation of the conductivity inside the bigger inclusion, while GA-MPC has the least accurate conductivity value estimate for the smaller ellipse. Moreover, GA-MPC gave more accurate approximations for both the geometry of the inclusion and its conductivity than the standard GA used in [KBK06; KMKKL02; RFSD14].

Case 3 - Two elliptical inclusions						
Algorithm	$\sigma_1$	$h_1$	$k_1$	$a_1$	$b_1$	$\theta_1$
True solution	6.1	-0.2	0.3	0.3	0.7	$3\pi/8$
FA	6.9516	-0.1863	0.3907	0.6940	0.9641	1.1961
NBA	7.6084	-0.1875	0.3585	0.3865	1.5049	1.2479
GA-MPC	7.2698	-0.2044	0.3041	0.3410	0.7933	1.1834
LSHADE-SPACMA	<b>6.8679</b>	-0.2041	<b>0.2985</b>	<b>0.3160</b>	<b>0.7423</b>	<b>1.1810</b>
LSHADE-cnEpSin	7.5342	<b>-0.2012</b>	0.2977	0.3278	0.7572	1.1813
EBOwithCMAR	7.2067	-0.2149	0.3130	0.3317	0.8161	1.1737

Algorithm	$\sigma_2$	$h_2$	$k_2$	$a_2$	$b_2$	$\theta_2$
True solution	6.7	0.45	-0.55	2.7	2.1	$5\pi/8$
FA	7.0271	-0.0174	-0.0840	0.9879	0.8254	2.1393
NBA	6.9453	0.0846	-0.0628	1.9633	1.1535	2.0135
GA-MPC	7.2293	0.4384	-0.5249	2.9269	<b>2.1106</b>	<b>1.9645</b>
LSHADE-SPACMA	6.5312	<b>0.4526</b>	-0.5435	2.7570	2.0587	1.9484
LSHADE-cnEpSin	6.3098	0.4575	<b>-0.5476</b>	<b>2.7362</b>	2.1318	1.8048
EBOwithCMAR	<b>6.7852</b>	0.3934	-0.4856	2.4609	1.7542	1.8492

TABLE 4.8: Final solutions generated by the proposed heuristic algorithms for Case 3. (Note that  $3\pi/8 \approx 1.18$  and  $5\pi/8 \approx 1.96$ .)

Improvements of DE, namely LSHADE-SPACMA and LSHADE-cnEpSin, also performed better than the DE used in [RKKLK10].

Metaheuristic algorithms can be computationally costly since they require many cost function evaluations. Because we made the stopping criterion based on the maximum number of function evaluations alone, the run time of all the algorithms are approximately equal. For this reason, we only provide the time for each domain case. For Case 1, it takes approximately 3 seconds for one function evaluation to be done and the number of function evaluations is set to 1000. Meanwhile for Case 2, we have 3.7 seconds for one function evaluation and the number of function evaluations is 6000. Lastly for Case 3, we get 4.3 seconds for one function evaluation with 12000 total number of function evaluations. To expect driving 3D computational simulations is challenging. Metaheuristic algorithms are time consuming and improvements are needed to get 3D results. We also note that to consider higher levels of noise, the use of regularization methods or more assumptions are needed in the formulation of the inverse problem, especially for Cases 2 and 3.

Lastly, to compare our results to that of deterministic method, we applied a quasi-Newton iterative method (BFGS) to Cases 1 and 2 with a random initial

Case 3 - Two elliptical inclusions						
Algorithm	$\sigma_1$	$h_1$	$k_1$	$a_1$	$b_1$	$\theta_1$
FA	13.96	6.85	30.23	37.73	131.33	56.49
NBA	24.73	6.25	19.51	28.82	114.9	5.93
GA-MPC	19.18	2.18	1.37	13.65	13.32	0.45
LSHADE-SPACMA	<b>12.59</b>	2.05	<b>0.49</b>	<b>5.32</b>	<b>6.05</b>	<b>0.25</b>
LSHADE-cnEpSin	23.51	<b>0.62</b>	0.76	9.28	8.18	0.27
EBOwithCMAR	18.14	7.45	4.32	10.57	16.59	0.37

Algorithm	$\sigma_2$	$h_2$	$k_2$	$a_2$	$b_2$	$\theta_2$
FA	4.88	103.87	84.73	52.96	69.43	8.95
NBA	3.66	81.20	88.59	27.28	45.07	2.54
GA-MPC	7.90	2.59	4.56	8.40	<b>0.51</b>	<b>0.05</b>
LSHADE-SPACMA	2.52	<b>0.57</b>	1.19	2.11	1.96	0.77
LSHADE-cnEpSin	5.82	1.66	<b>0.44</b>	<b>1.34</b>	1.52	8.08
EBOwithCMAR	<b>1.27</b>	12.57	11.70	8.86	16.47	5.82

TABLE 4.9: Reconstruction errors in % of each parameters in the final solution generated by the proposed heuristic algorithms for Case 3.

guess and no regularization term added to the cost function. We use the Matlab built-in command function *fminunc* to implement the quasi-Newton iterative algorithm. In Case 1, the reconstruction error is 6.17E-04, standard deviation is 2.21E-04 and the average cost function is 1.4E-03. This is almost the same results that we got from the six heuristic algorithms. Considering that there is no regularization term added to the cost function, BFGS performed really well in Case 1. However for Case 2, BFGS yielded a mean error of 151.6, standard deviation 361.8, and average cost function 5.97 which are huge values comparing to the results of the six heuristic algorithms. In this case when both the geometry and conductivity value are unknowns, the metaheuristic algorithms had a clear advantage over BFGS.



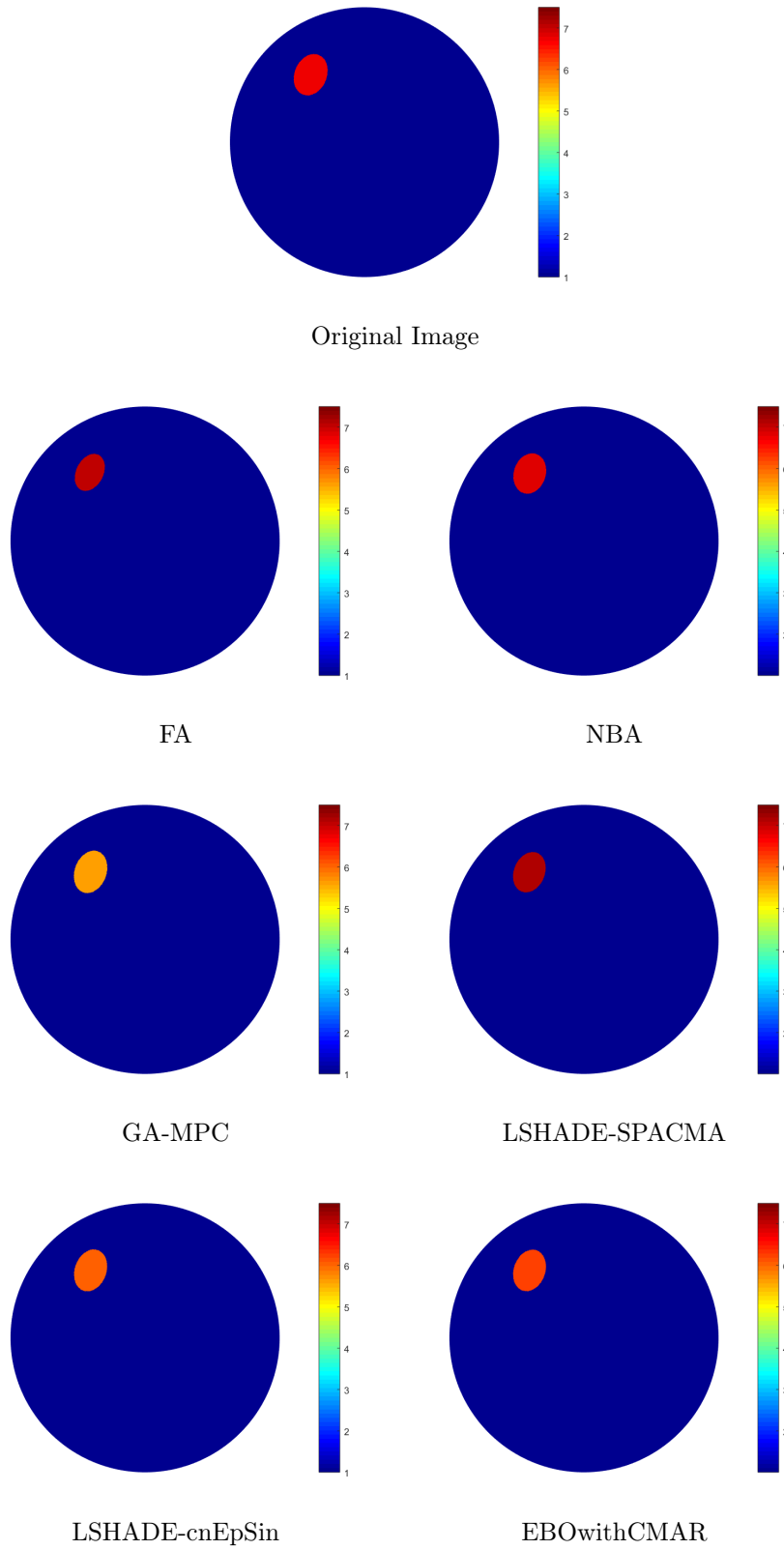


FIGURE 4.2: Image reconstructions for Case 2. The background conductivity is  $\sigma_0 = 1.0 \text{ mS} \cdot \text{cm}^{-1}$ . The conductivity inside the ellipse of the original image is  $\sigma_e = 6.7 \text{ mS} \cdot \text{cm}^{-1}$ .

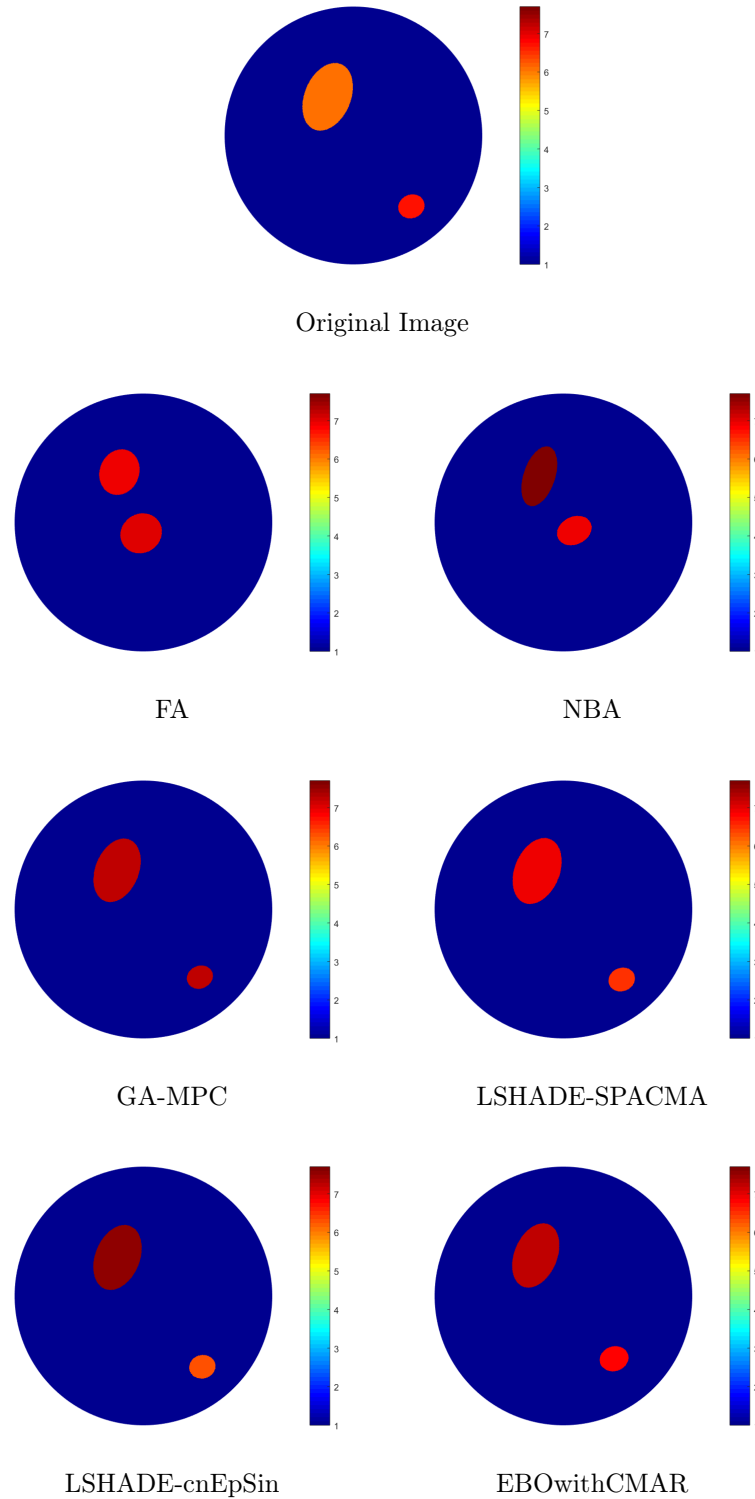


FIGURE 4.3: Image reconstructions for Case 3. The background conductivity is  $\sigma_0 = 1.0 \text{ mS} \cdot \text{cm}^{-1}$ . The conductivities are  $\sigma_1 = 6.1 \text{ mS} \cdot \text{cm}^{-1}$  (big ellipse) and  $\sigma_2 = 6.7 \text{ mS} \cdot \text{cm}^{-1}$  (small ellipse) in the original image.

## 4.4 Conclusion and perspectives

We have presented a conclusive study of the applicability of several heuristic approaches for EIT image reconstruction. Up to our knowledge, this is the first time that such a comparative study (between FA, NBA, GA-MPC, LSHADE-SPACMA, LSHADE-cnEpSin, and EBOwithCMAR) is addressed for EIT. Numerical simulations, given a fixed number of cost function evaluations and default heuristic algorithm parameters, showed that the more recent algorithms, namely LSHADE-SPACMA, LSHADE-cnEpSin, and EBOwithCMAR, obtained the best results in terms of accuracy, repeatability, and average cost. This indicates the continuous improvement in metaheuristic techniques, reinforcing their potential to solve other similar problems. FA did not fare as well as the other algorithms, especially in retrieving two disjoint inclusions (Case 3), because the maximum number of evaluations and the population size for each iteration might not be enough to have a balance between exploitation and exploration. This might be also the case for NBA and GA-MPC. Although NBA was successful in the image reconstruction of one defect (Cases 1 and 2), it failed in the configuration with two defects. Modifications and improvement in these three algorithms can be further studied to obtain more competitive results. Since FA, NBA, and GA-MPC populations for each iteration is fixed, we can recommend adjusting the population size so that there will be a balance between exploitation and exploration. Also, the maximum number of evaluations can be increased. Because of their population size linear reduction and self-adapting parameters system, the most recent algorithms LSHADE-SPACMA, LSHADE-cnEpSin, and EBOwithCMAR are more consistent and accurate. The different numerical results attest their efficiency. In the thorax domain, where only the conductivities of the inclusions are unknown, the six heuristic algorithms provided excellent results. In the other cases, the recovery of conductivity needs more improvement.

The application of the heuristic algorithms in 2D EIT inverse problem is tested in this chapter and was proven to be effective in the reconstruction, especially in the case where the only unknowns are the conductivity values of the inclusions. The said case can be seen in real-life applications, in organ functions imaging. However, due to their expensive computational time, the application of heuristic algorithms in 3D EIT inverse problem is a very challenging issue and might be complicated. Furthermore, there is still a lack of mathematical analysis behind these algorithms. The convergence and efficiency analysis of the majority of these heuristic algorithms are still unsolved and quite hard to prove.

Finally, possible future works include using a regularization term in the cost functional to deal with the ill-posedness of the problem. Fine tuning of the parameters of the algorithms to better fit the heuristic algorithms to the EIT inverse problem define also an interesting perspective. Moreover, notice that our code requires only the parameterization of the inspected domain, and we proved that it can deal with realistic geometries, as the thorax. This is promising for other applications.



## Chapter 5

# Study of the Complete Electrode Model for Electroencephalography

Electroencephalography or EEG is a non-invasive imaging technique for brain function monitoring. EEG signals are represented by the voltage potential fluctuations recorded at the electrodes on the scalp. EEG aims to localize cerebral sources generating the measured EEG signals, and hence, it is an inverse source problem whereas EIT is an inverse conductivity problem. In this chapter, we study the Complete Electrode Model for EEG. An existence and uniqueness result of this model is proved. Conclusions and perspectives are addressed.

### 5.1 Neurological basics

The human brain is a highly complex structure. It is responsible for the control of basic bodily functions and management of almost all information gathered in the body. The brain is mainly composed of tissues that are characterized by a complex network of neurons. Neurons are cells that specialize in information processing in the body. They gather information through their dendritic branches arising from their body cell and communicate that information with each other through the axon which is a unique extension of the cell body that is linked to the dendrite of another neuron cell (see Figure 5.1). The information will either inhibit or excite short electric waves in the target neuron [Ags15]. The electrical activity from a single neuron is too small to be measured in practice. However, if a large number (billions) of neighboring well-oriented neurons in the cerebral cortex beneath the skull are simultaneously active in a small region, then their electrical activity is measurable and yields an EEG signal. Thus, EEG measures non-invasively the electrical activity of the functioning brain at the surface of the scalp. In particular, the voltage potential fluctuations between different cortical regions are the measurements in EEG [ADDEL18; DL18].

In using EEG as a functional brain imaging, the important goal is to localize cerebral sources generating measured EEG signals. These sources are assumed to be the origin of physiological and pathological activities of the brain. EEG is one of the main diagnostic tests in presurgical evaluation for refractory epilepsy [DL18]. Figure 5.2 shows how EEG is applied in practice and how does an EEG signal look like in an epileptic episode. Moreover, EEG measures the electrical activity of the brain as EIT, but the main difference is that no currents are

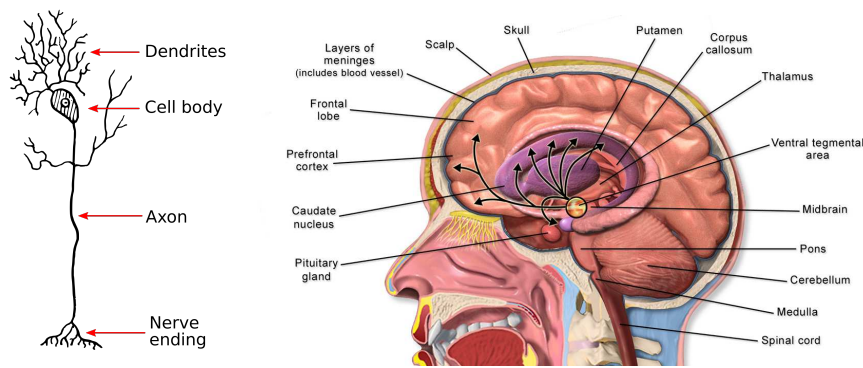


FIGURE 5.1: A neuron cell (left) and the human brain (right) (source:wikimedia)

injected. The sources are the neural ones. But, as in EIT studied in the previous chapters, EEG is also divided into two sub-problems: the forward problem and the inverse problem. The EEG forward problem also computes the electric potential at a set of electrodes on the scalp for a given source distribution in the brain. The conductivity map of the different head tissues and the head model itself are given and fixed in the problem. Using the measured/computed potentials, the aim of the EEG inverse problem is to localize the neural sources generating the said potentials. This is called an inverse source problem. Similarly in EIT again, the accuracy of the EEG source localization problem heavily relies on the accuracy of the associated forward model [DL18]. The knowledge of the conductivity map is important in the study of EEG problems. The solution to the source localization problem is highly dependent on the values taken by the scalp, skull, and brain conductivities [ADDEL18].

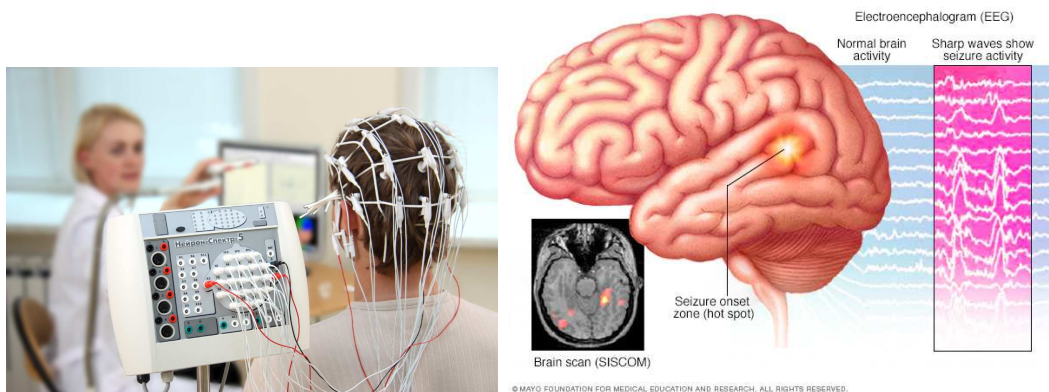


FIGURE 5.2: EEG in practice (left, source:wikimedia) and EEG epilepsy diagnosis (right, source:mayoclinic.org)

## 5.2 The mathematical modeling of EEG

In this section, we discuss the mathematical modeling of EEG. Different choices have to be done: the head model, the conductivity distribution of the head

tissues, and the characteristics of the neural sources in the brain. The governing equation describing EEG is derived.

### 5.2.1 Head models

The human head, and the different tissues within it, is the computational region of interest in the modeling of EEG. There are two types of head models that are commonly used in the literature: the classical spherical model and the realistic head model. The most straightforward spherical model is composed of three concentric spheres representing brain, skull, and scalp. Neuronal tissue is divided into two parts: the tissue that is rich in axons which is called the white matter, and the tissue that is rich in cell bodies also known as the grey matter. Other neuronal tissue in the brain that is scattered in the ventricle system have spaces that are filled with the so-called cerebrospinal fluid (CSF). CSF serves as a barrier between the brain and the skull. Multilayer spherical models distinguish between white and grey matter and take into account CSF as well as skull and scalp. As for other models, they are obtained from coregistered Magnetic Resonance Imaging (MRI) and CT-scans. The most important and difficult task is the extraction of the skull geometry, and to determine a clear separation of the boundaries of the skull and CSF [ADDEL18; DL18]. Figure 5.3 shows the head models discussed above.

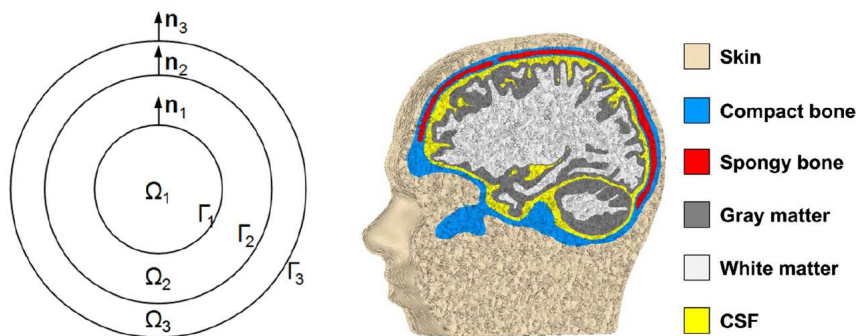


FIGURE 5.3: Three-layer spherical model and CT scan of head.[DL18]

We describe mathematically the different head models as follows. Let  $\Omega \in \mathbb{R}^3$  be a bounded, simply connected domain with regular boundary  $\Gamma_K$ . Suppose  $\Omega$  is partitioned into  $K$  open, disjoint, and nested sub-domains  $(\Omega_i)_{i=1, \dots, K}$ , that is,

$$\overline{\Omega} = \bigcup_{i=1}^K \overline{\Omega}_i,$$

where  $\Omega_i \cap \Omega_j = \emptyset \forall i \neq j$ , and  $\overline{\Omega}_i \cap \overline{\Omega}_j = \emptyset \forall j \neq i-1, i, i+1$ . We denote by  $\Gamma_i$ ,  $i = 1, \dots, K-1$ , the interface between  $\Omega_i$  and  $\Omega_{i+1}$  and we assume that  $(\Gamma_i)_i$  are closed regular surfaces. In the three-layer spherical model shown in Figure 5.3,  $\Omega_1$  is the representation of the brain,  $\Omega_2$  of the skull, and  $\Omega_3$  of the scalp. Lastly, we let  $\vec{n}_i$  be the unit normal vector on  $\Gamma_i$  oriented towards the exterior of  $\Omega_i$ .

## 5.2.2 Conductivities of head tissues

The behavior of free charges is described by the conductivity of a material. Conductivity represents the magnitude of the effect of the strength of the electrical field to the current density, that is, higher conductivity means stronger current. Meanwhile, the dielectric constant or permittivity describes the polarities occurring in a tissue, if charges are bounded in one place. With this, a precise knowledge of the electrical conductivity is an important factor in EEG modeling. But as seen in EIT, obtaining the conductivity through direct measurements is a difficult task. Also, uncertainties about the effective values of the dielectric properties of the tissues, especially in the skull, have to be taken into account [DL18]. In this chapter, we assume that the conductivity in each tissue to be homogeneous and isotropic, that is, to model the conductivity as a piecewise constant function

$$\sigma|_{\Omega_i} = \sigma_i > 0, \quad \forall i = 1, \dots, K.$$

## 5.2.3 Source models

As mentioned earlier, a large number of neurons must be simultaneously active in a small region inside the brain so that an electrical activity is measurable and yields an EEG signal. Define  $\mathbf{J}^p$  as the current density of the impressed neural (or primary) current supported within the brain  $\Omega_1$  where the neural activity is localized. In EEG modeling literature, the current sources are usually treated in the form of dipoles which are easy to construct and deal with mathematically [Ags15]. The localized primary current is modeled by pointwise current dipole defined as

$$\mathbf{J}^p(\mathbf{x}) = \mathbf{q}\delta_S(\mathbf{x}), \quad \mathbf{x} \in \Omega_1$$

where  $S$  is the position of the source,  $\mathbf{q} \in \mathbb{R}^3$  its moment, and  $\delta_S$  is the Dirac delta distribution at  $S$ .

More generally, we consider  $M$  electric dipoles as sources of the neural activity in the brain and with each dipole being characterized by its position  $S_m \in \Omega_1$  and its moment  $\mathbf{q}_m \in \mathbb{R}^3$ . Dipoles are mutually distinct, *i.e.*,  $S_m \neq S_p \quad \forall m \neq p$ , and their corresponding moments are nonzero. The current density  $\mathbf{J}^p$  is the sum of  $M$  pointwise current dipoles, that is,

$$\mathbf{J}^p = \sum_{m=1}^M \mathbf{q}_m \delta_{S_m}, \quad \mathbf{x} \in \Omega_1. \quad (5.1)$$

## 5.2.4 The Quasi-Static Maxwell's equation

As in EIT, the main equation describing the electromagnetic field in EEG measurements is derived from the quasi-static Maxwell equations for a linear, isotropic, nondispersive body. The low frequency range in both EEG and EIT measurements enables to neglect the time derivatives in the equations. The

main difference is that, in EEG, there is no injected current and that the current density  $\mathbf{J}$  splits into two terms:

$$\mathbf{J} = \sigma \nabla u + \mathbf{J}^p, \quad (5.2)$$

where  $\sigma \nabla u$  comes from Ohm's Law and  $\mathbf{J}^p$  is the primary current density (5.1), we have

$$\nabla \cdot \mathbf{J}^p = \sum_{m=1}^M \mathbf{q}_m \cdot \nabla \delta_{S_m}. \quad (5.3)$$

Recall that the divergence of  $\mathbf{J}$  is zero and so, we get the following elliptic equation for EEG

$$-\nabla \cdot (\sigma \nabla u) = \sum_{m=1}^M \mathbf{q}_m \cdot \nabla \delta_{S_m}, \quad \text{in } \Omega. \quad (5.4)$$

## 5.3 The Complete Electrode Model for EEG forward problem

The CEM for EEG forward problem is thoroughly studied in this section. The existence and uniqueness of the solution is proven using the subtraction method to deal with the singularity of the source term in (5.4).

### 5.3.1 Modeling the electrodes

In practice, voltage measurements on the boundary are recorded using a finite number of electrodes of finite length. Hence, modeling the said electrodes that are attached on the scalp is important. The standard electrode model for EEG is the point electrode model (PEM) where the electrodes are identified with a point on the scalp. The potential is calculated at these points. In PEM, it is also assumed that the current density is constant and that currents are not allowed to freely flow out of and into the head. Meanwhile in CEM, the geometry (form and size) of the electrodes is taken into account. We recall a set of patches  $e_\ell \subset \partial\Omega$ ,  $\ell = 1, \dots, L$  as the mathematical model of the contact electrodes that satisfy (1.12)  $\bar{e}_\ell \cap \bar{e}_k = \emptyset$  for  $\ell \neq k$ .

Furthermore, even though net currents flowing through the electrodes are zero in EEG, subelectrode surface currents exist due to potential variation. These shunting effects, if not accounted, can lead to lower voltage amplitudes [PLW16; DIS89]. The CEM accounts the effective contact impedance and thus, CEM models more accurately the electrode shunting effects. In particular, the voltage at the electrode is taken to be the integral average of the interior potential and a voltage drop due to contact impedance is added. Since PEM does not account the effective contact impedance, PEM can be seen as a limit case of the CEM with the effective contact impedance raised to infinity. This is because when the contact impedance increases, the shunting effect decreases [Ags15]. The CEM accounts for more accurate modeling of electrode shunting and thereby, in principle, extends the interval of applicable impedances beyond

that of the classical PEM. We focus on the study of CEM for the EEG forward problem in this chapter.

The main difference between the EEG and EIT is the absence of injected currents at the electrodes. In particular, we get for each electrode  $e_\ell$ ,

$$\int_{e_\ell} \sigma \partial_{\vec{n}} u \, ds = 0,$$

and for the part of the boundary where there are no electrodes

$$\sigma \partial_{\vec{n}} u = 0.$$

Moreover, the voltage drop due to contact impedance is given by

$$u + z_\ell \sigma \partial_{\vec{n}} u = U_\ell.$$

Let the sum of  $M$  electric dipoles be the source model of the neural activity in the brain. The characterization of each dipole is by its position  $S_m \in \Omega_1$  and its moment  $\mathbf{q}_m \in \mathbb{R}^3$ . The points  $(S_m)_m$  are assumed to be mutually distinct, *i.e.*,  $S_m \neq S_p \, \forall m \neq p$ , and their corresponding moments are nonvanishing. Recall that the elliptic equation for EEG (5.4).

Hence, we get the following boundary value problem for EEG: find  $(u, U)$  such that

$$\begin{cases} -\nabla \cdot (\sigma \nabla u) = \sum_{m=1}^M q_m \cdot \nabla \delta_{S_m}, & \text{in } \Omega, & (5.5) \\ u + z_\ell \sigma \partial_{\vec{n}} u = U_\ell, & \text{on } e_\ell, \ell = 1, 2, \dots, L, & (5.6) \\ \sigma \partial_{\vec{n}} u = 0, & \text{on } \partial\Omega \setminus \Gamma_e, & (5.7) \\ \int_{e_\ell} \sigma \partial_{\vec{n}} u \, ds = 0, & \ell = 1, 2, \dots, L. & (5.8) \end{cases}$$

The ground potential condition

$$\sum_{\ell=1}^L U_\ell = 0, \quad (5.9)$$

is also assumed in the CEM for EEG to assure the uniqueness of the solution.

The writing of the variational formulation of the above boundary value problem in  $H_\diamond$  is not possible because of the lack of regularity of the source term. We propose to apply the subtraction method in order to deal with the singularity in the source term of the problem.

### 5.3.2 Existence and uniqueness result

The source term in (5.5) presents a strong singularity at the source points  $S_m$ . In particular, it belongs to  $H^s(\mathbb{R}^3) \, \forall s < -5/2$  and due to this lack of regularity, a direct variational formulation in  $H_\diamond$  is impossible. In [PLW16; PLW12], the weak form in [SCI92] of the boundary value problem of the CEM is uniquely

solvable if the primary current density  $\mathbf{J}^p$  is assumed to be sufficiently smooth with a square integrable divergence. In this chapter, we overcome the singularity of the problem by applying an approach called the subtraction method (see [ADDEL18; DL18] and their references within). The existence and uniqueness of the solution of CEM for EEG is thoroughly discussed in this section.

### Subtraction method

To deal with the singularity in the source term, the subtraction method uses the fundamental solution of the Laplacian to explicitly determine the singular behavior of  $u$  near the source points  $S_m$ . Consequently, the remaining part of solution  $u$  is regular and a variational formulation in standard space can be written. This method has been firstly introduced for a single source model and piecewise constant conductivity, but the extension to isotropic inhomogeneous conductivities is studied in [ADDEL18; DL18].

It is assumed that the conductivity in a neighborhood of each source is constant. In particular, a family of non-intersecting open balls  $(\mathcal{V}_m)_{m=1,\dots,M}$  is fixed where  $\mathcal{V}_m \subset \subset \Omega_1$ ,  $\mathcal{V}_m \cap \mathcal{V}_p = \emptyset$  if  $m \neq p$ , and  $S_m \in \mathcal{V}_m$  and

$$\sigma_1|_{\mathcal{V}_m} \equiv c_m \in \mathbb{R}, \text{ for any } m \in \{1, \dots, M\}. \quad (5.10)$$

The subtraction method consists of splitting the potential solution  $u$  into a singular potential  $\tilde{u}$  and regular part  $w$ , that is,

$$u = \tilde{u} + w, \text{ where } \tilde{u} = \sum_{m=1}^M \tilde{u}_m. \quad (5.11)$$

The singular potential  $\tilde{u}_m$  is the solution of the Poisson's equation with a single dipolar source term at  $S_m$  in an infinite medium with conductivity  $c_m = \sigma_1(S_m)$ , i.e.

$$-c_m \Delta \tilde{u}_m = \mathbf{q}_m \cdot \nabla \delta_{S_m} \text{ in } \mathbb{R}^3. \quad (5.12)$$

It is determined by the convolution of the fundamental solution of the Laplace equation with the right-hand side  $\frac{1}{c_m} \mathbf{q}_m \cdot \nabla \delta_{S_m}$  and is given by

$$\tilde{u}_m(\mathbf{x}) = \frac{1}{4\pi c_m} \mathbf{q}_m \cdot \frac{(\mathbf{x} - S_m)}{|\mathbf{x} - S_m|^3}, \quad \forall \mathbf{x} \in \mathbb{R}^3 \setminus \{S_m\}. \quad (5.13)$$

It can be seen that  $\tilde{u}$  is smooth everywhere except at each source point  $S_m$ . Similarly, denoting  $\tilde{U}_\ell = \tilde{u}|_{e_\ell}$  and  $W_\ell = w|_{e_\ell}$ , the potential  $U_\ell$  at the electrodes is expressed by

$$U_\ell = \tilde{U}_\ell + W_\ell, \quad \ell = 1, 2, \dots, L. \quad (5.14)$$

We have to identify the problem satisfied by  $(w, W)$ . We note that  $\nabla \cdot (\sigma \nabla \tilde{u}_m)$  is well-defined and given by

$$\nabla \cdot (\sigma \nabla \tilde{u}_m) = \nabla \cdot ((\sigma - c_m) \nabla \tilde{u}_m) + c_m \Delta \tilde{u}_m. \quad (5.15)$$

Obtaining the equations that describes  $w$ , we get from (5.5) and using (5.12),

$$\begin{aligned}
-\nabla \cdot (\sigma \nabla w) &= \sum_{m=1}^M \mathbf{q}_m \cdot \nabla \delta_{S_m} + \nabla \cdot (\sigma \nabla \tilde{u}) \\
&= \sum_{m=1}^M [\mathbf{q}_m \cdot \nabla \delta_{S_m} + \nabla \cdot (\sigma \nabla \tilde{u}_m)] \\
&= \sum_{m=1}^M [\mathbf{q}_m \cdot \nabla \delta_{S_m} + \nabla \cdot ((\sigma - c_m) \nabla \tilde{u}_m) + c_m \Delta \tilde{u}_m] \\
&= \sum_{m=1}^M [\mathbf{q}_m \cdot \nabla \delta_{S_m} + \nabla \cdot ((\sigma - c_m) \nabla \tilde{u}_m) - \mathbf{q}_m \cdot \nabla \delta_{S_m}].
\end{aligned}$$

Thus, we get

$$-\nabla \cdot (\sigma \nabla w) = \sum_{m=1}^M \nabla \cdot ((\sigma - c_m) \nabla \tilde{u}_m), \text{ in } \Omega. \quad (5.16)$$

Furthermore, the boundary conditions are also defined accordingly. From (5.7), we get

$$\sigma \partial_{\vec{n}} w = -\sigma \partial_{\vec{n}} \tilde{u}, \text{ on } \partial\Omega \setminus \Gamma_e. \quad (5.17)$$

Next by using (5.8), we obtain

$$\int_{e_\ell} \sigma \partial_{\vec{n}} w \, ds = - \int_{e_\ell} \sigma \partial_{\vec{n}} \tilde{u} \, ds, \quad \ell = 1, 2, \dots, L. \quad (5.18)$$

Lastly, equation (5.6) gives for  $\ell = 1, \dots, L$

$$\tilde{u} + w + z_\ell \sigma \partial_{\vec{n}} (\tilde{u} + w) = U_\ell + W_\ell \text{ on } e_\ell, \quad (5.19)$$

and thus

$$w + z_\ell \sigma \partial_{\vec{n}} w = W_\ell - z_\ell \sigma \partial_{\vec{n}} \tilde{u}, \text{ on } e_\ell.$$

Finally, the boundary value problem for the regular part  $(w, W)$  is: find  $(w, W)$  such that

$$\left\{ \begin{array}{ll}
-\nabla \cdot (\sigma \nabla w) = \sum_{m=1}^M \nabla \cdot ((\sigma - c_m) \nabla \tilde{u}_m), & \text{in } \Omega, \\
w + z_\ell \sigma \partial_{\vec{n}} w = W_\ell - z_\ell \sigma \partial_{\vec{n}} \tilde{u}, & \text{on } e_\ell, \ell = 1, 2, \dots, L, \\
\sigma \partial_{\vec{n}} w = -\sigma \partial_{\vec{n}} \tilde{u}, & \text{on } \partial\Omega \setminus \Gamma_e, \\
\int_{e_\ell} \sigma \partial_{\vec{n}} w \, ds = - \int_{e_\ell} \sigma \partial_{\vec{n}} \tilde{u} \, ds, & \ell = 1, 2, \dots, L.
\end{array} \right. \quad (5.20)$$

From the decomposition, the existence and uniqueness of the potential  $(u, U)$  depends on the existence and uniqueness of  $(w, W)$ .

### Variational formulation

The following proposition gives a variational formulation of problem (5.20) for the auxiliary potential  $(w, W)$ .

**Proposition 5.3.1.** *The potential  $(w, W) \in H := H^1(\Omega) \oplus \mathbb{R}^L$  is a weak solution to (5.20) if and only if for any  $(v, V) \in H$ ,*

$$B((w, W), (v, V)) = f(v), \quad (5.21)$$

where the bilinear form  $B : H \times H \rightarrow \mathbb{R}$  is defined by

$$B((w, W), (v, V)) := \int_{\Omega} \sigma \nabla w \cdot \nabla v \, d\mathbf{x} + \sum_{\ell=1}^L \frac{1}{z_{\ell}} \int_{e_{\ell}} (w - W_{\ell})(v - V_{\ell}) \, ds, \quad (5.22)$$

and the linear form  $f : H \rightarrow \mathbb{R}$  is given by

$$f(v) := \sum_{m=1}^M \left[ \int_{\Omega} (c_m - \sigma) \nabla \tilde{u}_m \cdot \nabla v \, d\mathbf{x} - \int_{\partial\Omega} c_m (\partial_{\vec{n}} \tilde{u}_m) v \, ds \right]. \quad (5.23)$$

*Proof.* ( $\Rightarrow$ ) Suppose  $(w, W)$  is a weak solution to (5.20). Let  $(v, V) \in H$  be test functions. Multiplying  $v$  to (5.16) and using Green's formula, we have

$$\begin{aligned} & - \int_{\Omega} \nabla \cdot (\sigma \nabla w) v \, d\mathbf{x} = \sum_{m=1}^M \int_{\Omega} \nabla \cdot ((\sigma - c_m) \nabla \tilde{u}_m) v \, ds \\ \Leftrightarrow & \int_{\Omega} \sigma \nabla w \cdot \nabla v \, d\mathbf{x} - \int_{\partial\Omega} \sigma \partial_{\vec{n}} w v \, ds \\ & = \sum_{m=1}^M \left[ - \int_{\Omega} (\sigma - c_m) \nabla \tilde{u}_m \cdot \nabla v \, d\mathbf{x} + \int_{\partial\Omega} (\sigma - c_m) \partial_{\vec{n}} \tilde{u}_m v \, ds \right]. \end{aligned} \quad (5.24)$$

We have

$$\int_{\partial\Omega} \sigma \partial_{\vec{n}} w v \, ds = \sum_{\ell=1}^L \int_{e_{\ell}} \sigma \partial_{\vec{n}} w v \, ds + \int_{\partial\Omega \setminus \Gamma_e} \sigma \partial_{\vec{n}} w v \, ds.$$

From (5.18) and (5.19), we deduce

$$\begin{aligned} \int_{\partial\Omega} \sigma \partial_{\vec{n}} w v \, ds & = \sum_{\ell=1}^L \frac{1}{z_{\ell}} \int_{e_{\ell}} (W_{\ell} - w) v \, ds - \sum_{\ell=1}^L \int_{e_{\ell}} \sigma \partial_{\vec{n}} \tilde{u} v \, ds - \int_{\partial\Omega \setminus \Gamma_e} \sigma \partial_{\vec{n}} \tilde{u} v \, ds. \\ & = \sum_{\ell=1}^L \frac{1}{z_{\ell}} \int_{e_{\ell}} (W_{\ell} - w) v \, ds - \int_{\partial\Omega} \sigma \partial_{\vec{n}} \tilde{u} v \, ds. \end{aligned} \quad (5.25)$$

Now, substituting (5.25) in (5.24), we obtain

$$\begin{aligned} \int_{\Omega} \sigma \nabla w \cdot \nabla v \, d\mathbf{x} &+ \sum_{\ell=1}^L \frac{1}{z_{\ell}} \int_{e_{\ell}} (w - W_{\ell}) v \, ds \\ &= \sum_{m=1}^M \left[ \int_{\Omega} (c_m - \sigma) \nabla \tilde{u}_m \cdot \nabla v \, d\mathbf{x} - \int_{\partial\Omega} c_m \partial_{\bar{n}} \tilde{u}_m v \, ds \right]. \end{aligned} \quad (5.26)$$

Furthermore, the boundary conditions (5.18) and (5.17) give

$$\int_{e_{\ell}} w \, ds = \int_{e_{\ell}} (W_{\ell} - z_{\ell}(\sigma \partial_{\bar{n}} w + \sigma \partial_{\bar{n}} \tilde{u})) \, ds = \int_{e_{\ell}} W_{\ell} \, ds. \quad (5.27)$$

Let  $V = (V_{\ell})_{\ell=1}^L$  be an arbitrary vector in  $\mathbb{R}^L$ . Then from (5.27), we get

$$\int_{e_{\ell}} \frac{1}{z_{\ell}} (w - W_{\ell}) V_{\ell} \, ds = 0, \quad \ell = 1, 2, \dots, L. \quad (5.28)$$

Finally combining (5.28) and (5.26), we obtain the variational formulation (5.21)

$$\begin{aligned} \int_{\Omega} \sigma \nabla w \cdot \nabla v \, d\mathbf{x} &+ \sum_{\ell=1}^L \frac{1}{z_{\ell}} \int_{e_{\ell}} (w - W_{\ell})(v - V_{\ell}) \, ds \\ &= \sum_{m=1}^M \left[ \int_{\Omega} (c_m - \sigma) \nabla \tilde{u}_m \cdot \nabla v \, d\mathbf{x} - \int_{\partial\Omega} c_m \partial_{\bar{n}} \tilde{u}_m v \, ds \right]. \end{aligned} \quad (5.29)$$

( $\Leftarrow$ ) Suppose for all  $(v, V) \in H$ ,  $(w, W) \in H$  satisfies (5.21). To prove that  $(w, W)$  satisfies (5.20), we consider particular values for  $v$  and  $V$ .

Let  $v \in C^{\infty}(\Omega)$  with  $\text{supp } v \subset \Omega$  and  $V = 0$ . Then, the variational formulation (5.29) is

$$\int_{\Omega} \sigma \nabla w \cdot \nabla v \, d\mathbf{x} = \sum_{m=1}^M \int_{\Omega} (c_m - \sigma) \nabla \tilde{u}_m \cdot \nabla v \, d\mathbf{x},$$

which implies that  $w$  satisfies  $-\nabla \cdot (\sigma \nabla w) = \sum_{m=1}^M \nabla \cdot (\sigma - c_m) \nabla \tilde{u}_m$  in a weak sense.

By Green's formula, for arbitrary  $v \in H^1(\Omega)$ ,

$$\begin{aligned} \int_{\Omega} \sigma \nabla w \cdot \nabla v \, d\mathbf{x} &- \int_{\partial\Omega} \sigma \partial_{\bar{n}} w v \, ds \\ &= \sum_{m=1}^M \left[ - \int_{\Omega} (\sigma - c_m) \nabla \tilde{u}_m \cdot \nabla v \, d\mathbf{x} + \int_{\partial\Omega} (\sigma - c_m) \partial_{\bar{n}} \tilde{u}_m v \, ds \right]. \end{aligned} \quad (5.30)$$

Putting together the above equation and (5.21) where  $V = 0$ , we obtain

$$\int_{\partial\Omega} \sigma \partial_{\bar{n}} w v + \sum_{\ell=1}^L \frac{1}{z_\ell} \int_{e_\ell} (w - W_\ell) v \, ds = - \sum_{m=1}^M \int_{\partial\Omega} \sigma \partial_{\bar{n}} \tilde{u}_m v \, ds.$$

Note that the second term of the equation above can be expressed as

$$\sum_{\ell=1}^L \frac{1}{z_\ell} \int_{e_\ell} (w - W_\ell) v \, ds = \int_{\partial\Omega} \sum_{\ell=1}^L \frac{1}{z_\ell} (w - W_\ell) \chi_\ell v \, ds,$$

where  $\chi_\ell$  is the characteristic function of the  $\ell$ th electrode. Thus, we get

$$\int_{\partial\Omega} \left( \sigma \partial_{\bar{n}} w + \sum_{\ell=1}^L \frac{1}{z_\ell} (w - W_\ell) \chi_\ell + \sigma \partial_{\bar{n}} \tilde{u} \right) v \, ds = 0. \quad (5.31)$$

Since  $v$  is chosen arbitrarily, the auxiliary potential  $w$  satisfy

$$\sigma \partial_{\bar{n}} w + \frac{1}{z_\ell} (w - W_\ell) + \sigma \partial_{\bar{n}} \tilde{u} = 0, \text{ on } e_\ell, \ell = 1, \dots, L, \text{ and}$$

$$\sigma \partial_{\bar{n}} w = -\sigma \partial_{\bar{n}} \tilde{u}, \text{ on } \partial\Omega \setminus \Gamma_e.$$

This proves the boundary conditions (5.19) and (5.17). Lastly, substituting (5.30) and (5.31) to (5.21), we have

$$\begin{aligned} & \int_{\partial\Omega} \sigma \partial_{\bar{n}} w v \, ds + \sum_{\ell=1}^L \frac{1}{z_\ell} \int_{e_\ell} (w - W_\ell) (v - V_\ell) \, ds = - \int_{\partial\Omega} \sigma \partial_{\bar{n}} \tilde{u} v \, ds. \\ \Leftrightarrow & \int_{\partial\Omega} \left[ \sigma \partial_{\bar{n}} w + \sum_{\ell=1}^L \frac{1}{z_\ell} \int_{e_\ell} (w - W_\ell) \chi_\ell + \sigma \partial_{\bar{n}} \tilde{u} \right] v \, ds = \sum_{\ell=1}^L \frac{1}{z_\ell} \int_{e_\ell} (w - W_\ell) V_\ell \, ds. \\ \Leftrightarrow & \sum_{\ell=1}^L \frac{1}{z_\ell} \int_{e_\ell} (w - W_\ell) V_\ell \, ds = 0. \end{aligned}$$

Again, since  $V$  is chosen arbitrarily we conclude for  $\ell = 1, 2, \dots, L$

$$\int_{e_\ell} \frac{1}{z_\ell} (w - W_\ell) \, ds = 0 \Leftrightarrow \int_{e_\ell} (\sigma \partial_{\bar{n}} w + \sigma \partial_{\bar{n}} \tilde{u}) \, ds = 0,$$

and (5.18) holds.  $\square$

Now, we study the existence and uniqueness of a weak solution for the problem (5.20). First, we observe that the bilinear form  $B$  that was obtained in the variational formulation in Proposition 5.3.1 is the same as the bilinear form in CEM for EIT in Proposition 2.1.2. The main difference comes from the linear form

$$f(v) = \sum_{m=1}^M \left( \int_{\Omega} (c_m - \sigma) \nabla \tilde{u}_m \cdot \nabla v \, d\mathbf{x} - \int_{\partial\Omega} c_m \partial_{\bar{n}} \tilde{u}_m v \, ds \right).$$

The bilinear form  $B(\cdot, \cdot)$  and the linear form  $f(\cdot)$  are well defined on  $H^1(\Omega)$  if the conductivity  $\sigma$  belongs to  $L^\infty(\Omega)$  and satisfies the assumption (5.10). We have a Neumann boundary condition. If we set the test function  $v = V_\ell$ , then  $f(V_\ell) = -\int_{\partial\Omega} c_m \partial_{\vec{n}} \tilde{u}_m V_\ell ds = 0$ . Thus, the variational formulation (5.21) admits a solution only under the compatibility condition

$$\sum_{m=1}^M \int_{\partial\Omega} c_m \partial_{\vec{n}} \tilde{u}_m ds = 0.$$

This condition follows from the lemma below which is proven in [Dia17].

**Lemma 5.3.2.** *Let  $\tilde{u}$  be the solution of (5.12) given by (5.13). Then*

$$\int_{\partial\Omega} c_m \partial_{\vec{n}} \tilde{u}_m ds = 0, \quad \forall m = 1, \dots, M. \quad (5.32)$$

To obtain the uniqueness, we consider the quotient space  $\dot{H} = H/\mathbb{R}$  equipped with the norm defined in Lemma 2.1.3 (p.14) [SCI92].

**Theorem 5.3.3.** *Let the conductivity  $\sigma \in L^\infty(\Omega)$  be such that  $0 < \sigma_{\min} \leq \sigma(\mathbf{x}) < \sigma_{\max}$  for almost any  $\mathbf{x} \in \Omega$ , where  $\sigma_{\min}$  and  $\sigma_{\max}$  are two given positive constants. Assume further that  $\sigma|_{\mathcal{V}_m}$  is constant for any  $m = 1, \dots, M$  and denote by  $c_m$  the conductivity value of  $\sigma$  on  $\mathcal{V} \subset \Omega_1$ . Let the contact impedance  $Z \in \mathbb{R}^L$  fulfill the condition (1.20). Let the bilinear form  $B(\cdot, \cdot)$  and the linear form  $f(\cdot)$  be given by (5.22) and (5.23), respectively. Then the variational problem: find  $(w, W) \in \dot{H}$  such that*

$$B((w, W), (v, V)) = f(v), \quad \forall (v, V) \in \dot{H} \quad (5.33)$$

*has exactly one solution  $(w, W) \in \dot{H}$ .*

*Proof.* To prove the existence and uniqueness of solution in the quotient space  $\dot{H}$ , the Lax-Milgram lemma 2.1.1 is used. The coercivity on  $\dot{H}$  and continuity on  $\dot{H}$  of the bilinear form is proven in [SCI92] and detailed in Section 2.1.2. We again note that the same bilinear form in the variational formulation in Proposition 5.3.1 is obtained for CEM of EIT in Proposition 2.1.2. Meanwhile, the continuity of the linear form is shown in [ADDEL18]. Then the Lax-Milgram lemma yields the existence and uniqueness of the solution in  $\dot{H}$ .  $\square$

Furthermore, for the uniqueness of solution  $(w, W)$  in  $H$  we have the following corollary. The condition stated in the corollary (5.34) is from the ground potential condition (5.9) imposed on  $(u, U)$ .

**Corollary 1.** *Suppose that the hypotheses of Theorem 5.3.3 are satisfied. If the following relation holds*

$$\sum_{\ell=1}^L W_\ell = -\sum_{\ell=1}^L \tilde{U}_\ell, \quad (5.34)$$

*then the variational problem (5.21) has a unique solution in  $H$ .*

*Proof.* Existence of solution in  $H$  is assured by the norm equivalence shown in Remark 1. For the uniqueness, assume that there are two solutions  $(w, W)$  and  $(\bar{w}, \bar{W})$  satisfying (5.16) – (5.18). Let  $(v, V) = (w, W) - (\bar{w}, \bar{W})$ . Therefore, we have  $(v, V)$  satisfying the following boundary value problem

$$\begin{cases} \nabla \cdot (\sigma \nabla v) = 0, & \text{in } \Omega, & (5.35) \\ v + z_\ell \sigma \partial_{\bar{n}} v = V_\ell, & \text{on } e_\ell, \ell = 1, 2, \dots, L, & (5.36) \\ \sigma \partial_{\bar{n}} v = 0, & \text{on } \partial\Omega \setminus \Gamma_e & (5.37) \\ \int_{e_\ell} \sigma \partial_{\bar{n}} v \, ds = 0, & \ell = 1, 2, \dots, L. & (5.38) \end{cases}$$

Multiplying the same test function  $v$  to (5.35), integrating by parts, and applying the Green's Theorem, we have

$$\begin{aligned} \int_{\Omega} \sigma |\nabla v|^2 \, d\mathbf{x} &= \int_{\partial\Omega} (\sigma \partial_{\bar{n}} v) v \, ds \\ &= \sum_{\ell=1}^L \int_{e_\ell} (V_\ell - z_\ell \sigma \partial_{\bar{n}} v) \sigma \partial_{\bar{n}} v \, ds \\ &= \sum_{\ell=1}^L V_\ell \int_{e_\ell} \sigma \partial_{\bar{n}} v \, ds - \sum_{\ell=1}^L \int_{e_\ell} \frac{1}{z_\ell} |\sigma \partial_{\bar{n}} v|^2 \, ds \\ &= - \sum_{\ell=1}^L \int_{e_\ell} \frac{1}{z_\ell} |\sigma \partial_{\bar{n}} v|^2 \, ds. \end{aligned}$$

Since  $z_\ell \geq 0$ ,  $\forall \ell = 1, \dots, L$ , both sides of the equation above are zero. This implies that  $v$  is constant. Moreover, by (5.36), we have

$$v = \text{constant} = V_\ell, \quad \ell = 1, \dots, L.$$

Lastly, if we let constant  $K_1 = - \sum_{\ell=1}^L \tilde{U}_\ell$  we have

$$\sum_{\ell=1}^L W_\ell = K_1 = \sum_{\ell=1}^L \bar{W}_\ell.$$

So we get,

$$\sum_{\ell=1}^L V_\ell = 0.$$

Since all the voltages on the electrodes are equal to the same constant, the sum above forces the constant to be zero. Thus,

$$V_\ell = 0 = v, \quad \ell = 1, \dots, L.$$

This proves the uniqueness of solution in  $H$  of (5.20).  $\square$

Finally, the existence and uniqueness of the potentials  $(u, U)$  for the CEM forward problem of EEG (5.5) – (5.8) also follows.

*Remark 3.* Let say a few words about the numerical resolution of the EEG CEM (5.5)-(5.6)-(5.7)-(5.8). The discretization could be done by means of P1 finite elements. The first step will be to compute an approximation  $(w_h, W_h)$  of the potential  $(w, W)$ . To this end, an approach similar to the one proposed in Chapter 2 Subsection 2.2.3 can be applied. It would be interesting to get error estimates as for the discretization of the standard model for EEG [ADDEL18]. The approximation  $(u_h, U_h)$  of the electric potential  $(u, U)$ , solution to the EEG CEM (5.5)-(5.6)-(5.7)-(5.8), is deduced from the discrete solution  $(w_h, W_h)$  and decompositions (5.11) and (5.14).

## 5.4 Conclusion and perspectives

In this chapter, we have presented the application of the Complete Electrode Model for modeling EEG. The subtraction approach is used to deal with the singularity in the source term, and we have proved existence and uniqueness results for the continuous problem. A first perspective is to validate numerically this approach in order to compare the standard model (Point Electrode Model) and the CEM, particularly with experimental data. The aim is to study the effect of taking into account the electrodes on the accuracy of the EEG measurement simulations, and also on the numerical reconstruction of neural sources from data recorded at the electrodes. First numerical results in neonatal EEG have been provided by Pursiainen *et al.* [PLW16; PLW12] which conclude that the CEM can improve EEG forward simulation accuracy and can be considered as an integral part of the head model. Another important question is linked to the dependence of the source reconstruction on the uncertainty of tissue conductivities, and of skull particularly. A possible solution would consist in developing methods that reconstruct simultaneously sources and skull conductivity [Pap17]. The use of the CEM in these methods could be an interesting perspective.

# General conclusion

In this thesis, we worked on the study of the Complete Electrode Model (CEM) for Electrical Impedance Tomography (EIT). We have addressed both theoretical and numerical aspects of the CEM forward problem. A good understanding of the forward model is an essential preliminary step to the resolution of the corresponding EIT inverse problem. We analysed the effect of a change in conductivity on the electric potential in the domain under inspection and on the EIT measurements. Numerical results showed that the impact of imperfections in the conductivity distribution is non negligible on the values of the surface voltages, which are the data for the inverse problem. We then introduced the Gâteaux derivative as a mathematical tool for the sensitivity analysis of the electric potential with respect to a small variation in the conductivity or in the contact impedance of the electrodes. Numerical simulations in both 2D and 3D are presented and discussed. Particularly, a CT scan of a thorax and the spherical three-layer head model are considered. This study provided useful information on regions and electrodes where the electrical potential is the most sensitive to a variation of conductivity or of the contact impedance. The support of the sensitivity function depends on the characteristics (position, size, number) of the conductivity variations and is localized to an area (and thus at the electrodes) around the imperfections. Furthermore, we deduced that when the contact impedance on one electrode is perturbed, significant values of the sensitivity is found at this electrode. If the contact impedance of more electrodes are perturbed, then the total sensitivity value of one electrode is the sum of its sensitivity values when only one electrode is perturbed. For medical applications, this study confirmed that uncertain conductivity values impact the EIT forward solution.

Next, we proceeded to the inverse problem of EIT by formulating it as a minimization of a cost functional defined by the difference between the measured and the predicted boundary voltages. We applied six metaheuristic algorithms for the optimization. Two-dimensional numerical comparisons are done, with promising results especially in the thorax case where the geometries are fixed. We observed that the more recent algorithms performed better in the reconstruction, particularly in the domain where there are two unknown inclusions.

Lastly, we studied the CEM for electroencephalography (EEG). The subtraction method is used to deal with the singularity in the source term and the existence and uniqueness of the solution of the CEM forward problem is proven.

The following perspectives for future works are recommended:

- Study the behavior of the electric potential when both the conductivity inside the domain and the contact impedance at the electrodes are perturbed.

- Consider fine tuning of the parameters for the metaheuristic algorithms to accommodate the structure of the EIT inverse problem.
- Regularization of the cost functional to treat the instability of the reconstruction problem.
- Since the metaheuristic algorithms performed best when the geometries are fixed, we recommend to study a reconstruction algorithm combining metaheuristic and deterministic algorithms.
- Propose and validate a numerical approach for the CEM forward problem of EEG.

## Appendix A

# Metaheuristic algorithms pseudo-codes

### A.1 Firefly Algorithm pseudo-code.

**Input:** Objective function  $f(\mathbf{x})$ ,  $\mathbf{x} = (x_1, \dots, x_D)$  for  $D$  dimensions, number of fireflies  $N$ , MaxGen,  $\alpha$ ,  $\gamma$ ,  $\beta$ , light intensity  $I_i$  is determined by  $f(\mathbf{x}_i)$

**Output:** cost function  $f(\mathbf{x}^*)$  at optimal  $\mathbf{x}^*$

- 1: Generate initial population of fireflies  $\mathbf{x}_i$ ,  $i = 1, 2, \dots, N$ .
- 2: Initial evaluation of all  $N$  fireflies.
- 3: **while**  $FuncEvals < MaxEval$  **do**
- 4:   Increment  $k$ .
- 5:   **for**  $i = 1$  to  $N$  **do**
- 6:     **for**  $j = 1$  to  $N$  **do**
- 7:      **if**  $I_i < I_j$  **then**
- 8:        Move firefly  $i$  towards  $j$  with  $\mathbf{x}_i = \mathbf{x}_i + \beta e^{-\gamma r_{ij}} (\mathbf{x}_j - \mathbf{x}_i) + \alpha \epsilon_i$ , where  $r_{ij}$  is the Cartesian distance between two fireflies  $\mathbf{x}_i$  and  $\mathbf{x}_j$  and  $\epsilon_i$  is a vector of random numbers.
- 9:      **end if**
- 10:     Evaluate new solutions and update light intensity.
- 11:    **end for**
- 12:   **end for**
- 13:   Reduce  $\alpha$ .
- 14:   Rank the fireflies and find the current global best solution.
- 15: **end while**

### A.2 Novel Bat Algorithm pseudo-code.

**Input:** Objective function  $f(\mathbf{x})$ ,  $\mathbf{x} = (x_1, \dots, x_D)$  for  $D$  dimensions, number of bats  $N$ , maximum number of iterations  $M$ ,  $\alpha$ ,  $\gamma$ ,  $G$ ,  $w$ ,  $\theta$ ,  $C_{\min}$ ,  $C_{\max}$ ,  $P_{\min}$ ,  $P_{\max}$ ,  $A_{\min}$ ,  $A_{\max}$ ,  $r_{\min}$ ,  $r_{\max}$ ,  $f_{\min}$ ,  $f_{\max}$

**Output:** cost function  $f(\mathbf{x}^*)$  at optimal  $\mathbf{x}^*$

- 1: Generate initial population of bats  $x_{ij}^k$  and velocities  $v_{ij}^k$ ,  $i = 1, 2, \dots, N$ ,  $j = 1, 2, \dots, D$ .
- 2: Initial evaluation of all  $N$  bats.
- 3: Rank the bats with  $g_j^k$  as the best global position and its velocity is  $v_{gj}^k$ .
- 4: **while**  $FuncEvals < MaxEval$  **do**

- 5: **if**  $\text{rand}(0, 1) < P$ , where  $P \in [P_{\min}, P_{\max}]$  **then**  
 6:     Generate new solutions with

$$\mathbf{x}_{ij}^{k+1} = \begin{cases} g_j^k + \theta |\text{mean}_j^t - \mathbf{x}_{ij}^k| \ln\left(\frac{1}{\mu_{ij}}\right), & \text{if } \text{rand}_j(0, 1) < 0.5 \\ g_j^k - \theta |\text{mean}_j^t - \mathbf{x}_{ij}^k| \ln\left(\frac{1}{\mu_{ij}}\right), & \text{otherwise.} \end{cases}$$

- 7: **else**  
 8:     Generate new solutions with

$$\begin{aligned} f_{ij} &= f_{\min} + (f_{\max} - f_{\min}) \text{rand}(0, 1) \\ f_{ij} &= \left(\frac{c+v_{ij}^k}{c+v_{gj}^k}\right) f_{ij} \left(1 + C_i \frac{g_j^k - x_{ij}^k}{|g_j^k - x_{ij}^k| + \epsilon}\right) \\ v_{ij}^{k+1} &= wv_{ij}^k + (g_j^k - x_{ij}^k) f_{ij} \\ x_{ij}^{k+1} &= x_{ij}^k + v_{ij}^k, \end{aligned}$$

where  $w \in [0, 1]$  is a uniform random vector,  $\epsilon$  is the smallest constant in the computer,  $C \in [C_{\min}, C_{\max}]$ , and  $c = 340m/s$  is the speed in the air.

- 9: **end if**  
 10: **if**  $\text{rand}(0, 1) > r_i$  **then**  
 11:     Generate a local solution around the selected best solution using

$$x_{ij}^{k+1} = g_j^k (1 + \text{rand } n(0, \sigma^2)),$$

where  $\sigma^2 = |A_i^k - A_{\text{mean}}^k| + \epsilon$ , and  $\text{rand } n(0, \sigma^2)$  is a Gaussian distribution with mean 0 and standard deviation  $\sigma^2$ , and  $A_{\text{mean}}^k$  is the average loudness of all bats at time step  $t$ . Note that  $\epsilon$  is used to ensure that  $\sigma^2 > 0$ .

- 12: **end if**  
 13: Evaluate new solutions.  
 14: Update solutions, the loudness, and pulse emission rate using

$$\begin{aligned} f(\mathbf{x}) &= f(\mathbf{x}_i) \text{ if } \text{rand}(0, 1) < A_i \text{ and } f(\mathbf{x}_i) < f(\mathbf{x}) \\ A_i^{k+1} &= \alpha A_i^k \\ r_i^{k+1} &= r_i^0 (1 - e^{-\gamma k}) \end{aligned}$$

- 15: Rank the solutions and find the current best  $g^k$ .  
 16: **if**  $g^k$  does not improve in  $G$  time step **then**  
 17:     Re-initialize the loudness  $A_i$  and set temporary pulse rates  $r_i$  which is a uniform number between  $[0.85, 0.9]$ .  
 18: **end if**  
 19: Increment  $k$ .  
 20: **end while**

### A.3 GA-MPC pseudo-code.

**Input:** Objective function  $f(\mathbf{x})$ ,  $\mathbf{x} = (x_1, x_2, \dots, x_D)$  for  $D$  dimensions,  $PS$ ,  $\mathbf{x}_{\min}$ ,  $\mathbf{x}_{\max}$ ,  $\beta$ ,  $cr$ ,  $m$

**Output:** cost function  $f(\mathbf{x}^*)$  at the optimal  $\mathbf{x}^*$

1: Generate initial random population of size  $PS$  with

$$\mathbf{x}_i = \mathbf{x}_{\min,i} + u(\mathbf{x}_{\max,i} - \mathbf{x}_{\min,i}),$$

where  $u$  is a random vector with values in  $[0,1]$ .

2: **while**  $FuncEvals < MaxEval$  **do**

3: Rank all the individuals in the population by their cost function value and choose the best  $m$  individuals to form the archive pool  $\tilde{A}$ .

4: Apply a tournament selection with size  $TC$  and fill the selection pool.

5: Generate a random number  $\bar{u}$  in  $[0, 1]$ .

6: **for** each three consecutive individuals in the selection pool **do**

7: **if** one of the selected individual is the same to another **then**

8: Replace one by a randomly-selected individual in the selection pool.

9: **end if**

10: **if**  $\bar{u} < cr$  **then**

11: Rank these three individuals  $f(\mathbf{x}_i) \leq f(\mathbf{x}_{i+1}) \leq f(\mathbf{x}_{i+2})$ .

12: Calculate  $\beta = N(\tilde{\mu}, \tilde{\sigma})$ .

13: Generate three offspring from the three parents with

$$o_1 = \mathbf{x}_1 + \beta(\mathbf{x}_2 - \mathbf{x}_3)$$

$$o_2 = \mathbf{x}_2 + \beta(\mathbf{x}_3 - \mathbf{x}_1)$$

$$o_3 = \mathbf{x}_3 + \beta(\mathbf{x}_1 - \mathbf{x}_2).$$

14: **end if**

15: **for** each offspring  $o_i$  **do**

16: Generate a random number  $\bar{u}$  in  $[0, 1]$ .

17: **if**  $\bar{u} < p$  **then**

18: Mutate the offspring by  $o_i^j = \mathbf{x}_{arch}^j$ , where  $\mathbf{x}_{arch}$  is an individual from the archive pool and  $arch \in [1, m]$ .

19: **end if**

20: **end for**

21: **end for**

22: **if** there is a duplicate individual **then**

23: Replace the duplicate with

$$\mathbf{x}_i^j = \mathbf{x}_i^j + N(0.5 * \bar{u}, 0.25 * \bar{u}),$$

where  $\bar{u} \in [0, 1]$ .

24: **end if**

25: **end while**

## A.4 Simplified LSHADE-SPACMA pseudo-code.

**Input:** Objective function  $f(\mathbf{x})$ ,  $\mathbf{x} = (x_1, \dots, x_D)$  for  $D$  dimensions, memories  $M_{Cr}$ ,  $M_F$ , and  $M_{FCP}$ ,  $ArCrate$ ,  $p_{best}$ ,  $c$ ,  $H$ ,  $PS_{min}$ ,  $PS_{max}$

**Output:** cost function  $f(\mathbf{x}^*)$  at optimal  $\mathbf{x}^*$

- 1: Generate initial random population with size  $PS_{max}$ .
- 2: Set values of memories  $M_{Cr}$ ,  $M_F$ , and  $M_{FCP}$  to 0.5.
- 3: Initialize CMA parameters.
- 4: **while**  $FuncEvals < MaxEval$  **do**
- 5:   Semi-parameter adaptation (SPA) for scaling factor  $F$  and crossover rate  $Cr$ . During the first part of SPA, the adaptation is concentrated on  $Cr$  and for the second part the focus of the adaptation is on  $F$ .
- 6:   Split the population into two.
- 7:   Generate donor vectors using LSHADE or modified CMA-ES.
- 8:   Concatenate resulting vectors from LSHADE and modified CMA-ES.
- 9:   Generate trial vectors and mutate with  $p_{best}$ .
- 10:   Evaluate fitness of trial vectors.
- 11:   Implement selection strategy.
- 12:   Update population allocated to LSHADE and CMA-ES according to the relative performance of the two methods.
- 13:   Store successful parameters to memory of size  $H$ .
- 14:   Update archive with rate  $ArCrate$ .
- 15:   Update memory memory  $M_F$  during the first part of SPA and  $M_{FCP}$  with  $c$  during the second part. Update also  $M_{Cr}$ .
- 16:   Implement linear population size reduction with min pop size  $PS_{min}$ .
- 17:   Sort individuals and retain them based on the new population size.
- 18:   Update CMA-ES parameters.
- 19: **end while**

## A.5 Simplified LSHADE-cnEpSin pseudo-code.

**Input:** Objective function  $f(\mathbf{x})$ ,  $\mathbf{x} = (x_1, \dots, x_D)$  for  $D$  dimensions, memories  $M_{Cr}$ ,  $M_F$ , and  $M_{freq}$ ,  $ArCrate$ ,  $p_{best}$ ,  $freq$ ,  $H$ ,  $PS_{min}$ ,  $PS_{max}$ ,  $G_{max}$

**Output:** cost function  $f(\mathbf{x}^*)$  at optimal  $\mathbf{x}^*$

- 1: Generate initial population with size  $PS_{max}$ .
- 2: Initialize  $G_{max} = 2163$ .
- 3: Set values of memories  $M_{Cr}$ ,  $M_F$ , and  $M_{freq}$  to 0.5.
- 4: Initialize covariance matrix settings.
- 5: **while**  $FuncEvals < MaxEval$  **do**
- 6:   **if** number of generation is  $< G_{max}/2$  **then**
- 7:     Implement sinusoidal configuration to adapt  $F$  using  $freq$ .
- 8:   **else**
- 9:     Use Cauchy distribution to adapt  $F$ .
- 10:   **end if**
- 11:   Adapt  $Cr$  using normal distribution.
- 12:   **for**  $i = 1$  to population size **do**
- 13:     Generate mutant vectors with  $p_{best}$ .

- 14: Apply covariance matrix learning or binomial crossover to generate trial vectors.
- 15: Store successful  $F$  and  $Cr$ .
- 16: **end for**
- 17: Update memory  $M_{Cr}, M_F$  of size  $H$ , and archive with rate  $Arc_{rate}$ .
- 18: Implement linear population size reduction with min pop size  $PS_{\min}$ .
- 19: Sort individuals and retain them based on the new population size.
- 20: **end while**

## A.6 Simplified EBOwithCMAR pseudo-code.

**Input:** Objective function  $f(\mathbf{x})$ ,  $\mathbf{x} = (x_1, \dots, x_D)$  for  $D$  dimensions, population sizes  $PS_{1,max}$  and  $PS_{1,min}$ ,  $PS_{2,max}$  and  $PS_{2,min}$ , and  $PS_3$ ,  $prob_{ls}$ ,  $prob_1$ ,  $prob_2$ , and cycle  $CS$

**Output:** cost function  $f(\mathbf{x}^*)$  at optimal  $\mathbf{x}^*$

- 1: Generate initial main population.
- 2: Set  $prob_1$  for EBO and  $prob_2$  for CMAR to 1. Set other parameters.
- 3: Randomly assign members of the main population to three subpopulations  $X_1$ , and  $X_2$  for EBO, and  $X_3$  for CMAR. The max and min population size for  $X_1$  are  $PS_{1,max}$  and  $PS_{1,min}$ , respectively,  $PS_{2,max}$  and  $PS_{2,min}$  for  $X_2$ , and  $PS_3$  is the pop size for  $X_3$ .
- 4: **while**  $FuncEvals < MaxEval$  **do**
- 5:   **if** number of cycle is ==  $CS/2$  **then**
- 6:     Update  $prob_1$  and  $prob_2$ .
- 7:   **end if**
- 8:   **if** number of cycle is ==  $CS$  **then**
- 9:     Implement data sharing.
- 10:    Update parameters for EBO using  $H$  and CMAR with  $\tilde{\sigma}$ .
- 11:    Reset  $prob_1$ ,  $prob_2$  and number of cycles.
- 12:   **end if**
- 13:   **if**  $\text{rand}(0, 1) < prob_1$  **then**
- 14:     Apply EBO.
- 15:     Implement linear population size reduction and reallocate subpopulations.
- 16:   **end if**
- 17:   **if**  $\text{rand}(0, 1) < prob_2$  **then**
- 18:     Apply CMAR.
- 19:   **end if**
- 20:   **if**  $\text{rand}(0, 1) < prob_{ls}$  and  $FuncEvals \geq 0.75 * MaxEval$  **then**
- 21:     Apply SEQ.
- 22:     **if** best solution is improved **then**
- 23:       Set  $prob_{ls}$  to 0.1.
- 24:       Update  $X_1$  and  $X_2$ .
- 25:     **else**
- 26:       Set  $prob_{ls}$  to 0.0001.
- 27:     **end if**
- 28:   **end if**

29: Sort individuals and update allocations between subpopulations.  
30: **end while**

# Bibliography

- [ABGA95] A. Adler, Y. Berthiaume, R. Guardo, and R. Amyot. “Imaging of pulmonary edema with electrical impedance tomography”. In: *Proceedings of 17th International Conference of the Engineering in Medicine and Biology Society*. **1**. 1995, pp. 557–558.
- [Ags15] B. Agsten. “Comparing the complete and the point electrode model for combining tCS and EEG”. MA thesis. Münster, Germany: Westfälische Wilhelms-Universität Münster, 2015.
- [ATT19] H. Ammari, F. Triki, and C-H. Tsou. “Numerical determination of anomalies in multifrequency electrical impedance tomography.” In: *European Journal of Applied Mathematics* **30.3** (2019), pp. 481–504.
- [ARE19] L. Andiani, A. Rubiyanto, and Endarko. “Sensitivity analysis of thorax imaging using two-dimensional Electrical Impedance Tomography (EIT)”. In: *Journal of Physics: Conference Series* **1248** (2019), p. 012009.
- [AP06] K. Astala and L. Päivärinta. “Calderón’s inverse conductivity problem in the plane”. In: *Annals of Mathematics* **163** (2006), pp. 265–299.
- [AALQS16] N. H. Awad, M. Z. Ali, J. J. Liang, B. Y. Qu, and P. N. Suganthan. “Problem definitions and evaluation criteria for the CEC 2017 special session and competition on single objective bound constrained real-parameter numerical optimization”. In: *Technical Report*. Nanyang Technological University Singapore, 2016.
- [AAS17] N. H. Awad, M. Z. Ali, and P. N. Suganthan. “Ensemble sinusoidal differential covariance matrix adaptation with Euclidean neighborhood for solving CEC2017 benchmark problems”. In: *2017 IEEE Congress on Evolutionary Computation (CEC)*. IEEE. 2017, pp. 372–379.
- [AASR16] N. H. Awad, M. Z. Ali, P. N. Suganthan, and R. G. Reynolds. “An ensemble sinusoidal parameter adaptation incorporated with L-SHADE for solving CEC2014 benchmark problems”. In: *2016 IEEE Congress on Evolutionary Computation (CEC)*. 2016, pp. 2958–2965.

- [ADDEL18] H. Azizollahi, M. Darbas, M. M. Diallo, A. El Badia, and S. Lohrengel. “EEG in neonates: Forward modeling and sensitivity analysis with respect to variations of the conductivity”. In: *Mathematical Biosciences and Engineering* **15.4** (2018), pp. 905–932.
- [BLBTGTSD+03] A. P. Bagshaw, A. D. Liston, R. H. Bayford, A. Tizzard, A. P. Gibson, A. T. Tidswell, M. K. Sparkes, H. Dehghani, C. D. Binnie, and D. Holder. “Electrical impedance tomography of human brain function using reconstruction algorithms based on the finite element method”. In: *Neuroimage* **20** (2003), pp. 752–764.
- [BB84] D. C. Barber and B. H. Brown. “Applied potential tomography”. In: *Journal of Physics E: Scientific Instruments* **17.9** (1984), pp. 723–733.
- [BRSFSRPF+18] V. A. Barbosa, D. E. Ribeiro, W. P. dos Santos, R. C. Freitas, R. E. de Souza, R. R. Ribeiro, M. Paschoal, A. R. Feitosa, N. S. Soares, R. B. Valenca, V. L. B. A. da Silva, R. L. Ogava, and I. J. N. S. A. Dias. “Image Reconstruction of Electrical Impedance Tomography Using Fish School Search and Differential Evolution”. In: *Critical Developments and Applications of Swarm Intelligence* (2018), pp. 301–338.
- [BRSRFFSS17] V. A. Barbosa, R. R. Ribeiro, A. R. Silva, V. L. Rocha, R. C. Freitas, A. R. Feitosa, R. E. de Souza, and W. P. dos Santos. “Reconstruction of electrical impedance tomography images using chaotic ring-topology particle swarm optimization and non-blind search”. In: *International Journal of Swarm Intelligence Research* **8.2** (2017), pp. 17–33.
- [BMS80] R. Bates, G. McKinnon, and A. Seagar. “A limitation on systems for imaging electrical conductivity distributions.” In: *Biomedical Engineering* **7** (1980), pp. 418–420.
- [Bor03] L. Borcea. “Electrical Impedance Tomography”. In: *Inverse Problems* **19.4** (2003), pp. 997–998.
- [BLM02] A. Borsic, R. B. Lionheart, and N. McLeod. “Generation of anisotropic-smoothness regularization filters for EIT.” In: *IEEE Transactions on Medical Imaging* **21.6** (2002), pp. 579–587.
- [BLS13] I. Boussaïd, J. Lepagnot, and P. Siarry. “A survey on optimization metaheuristics”. In: *Information Sciences* **237** (2013), pp. 82–117.

- [BKIN07] G. Boverman, B. S. Kim, D. Isaacson, and J. C. Newell. “The Complete Electrode Model For Imaging and Electrode Contact Compensation in Electrical Impedance Tomography”. In: *2007 29th Annual International Conference of the IEEE Engineering in Medicine and Biology Society*. 2007, pp. 3462–3465.
- [Bra02] D. Braess. “Finite Elements: Theory, fast solvers and applications in solid mechanics, 2nd edn”. In: *Measurement Science and Technology* **13.9** (2002), p. 1500.
- [Bro03] B. Brown. “Electrical impedance tomography (EIT): A review”. In: *Journal of medical engineering & technology* **27** (2003), pp. 97–108.
- [CLPM20] R. C. Cajayon, J. A. Lucilo, C. P. C. Pilar-Arceo, and E. R. Mendoza. “Comparison of Two Nature-inspired Algorithms for Parameter Estimation of S-system Models”. In: *Philippine Journal of Science* **149.1** (2020), pp. 63–78.
- [Cal80] A. Calderón. “On an inverse boundary value problem”. In: *Seminar on Numerical Analysis and its Applications to Continuum Physics (Rio de Janeiro, 1980)* (1980), pp. 65–73.
- [Che90] Z.Q. Chen. “Reconstruction algorithms for electrical impedance tomography”. PhD thesis. New South Wales, Australia: University of Wollongong, 1990.
- [CING89] K.-S. Cheng, D. Isaacson, J. Newell, and D. Gisser. “Electrode Models for Electric Current Computed Tomography”. In: *IEEE Transactions on Biomedical Engineering* **36.9** (1989), pp. 918–924.
- [CKKKMMM01] V. Cherepenin, A. Karpov, A. Korjenevsky, V. Kornienko, A. Mazaletskaia, D. Mazourov, and D. Meister. “A 3D electrical impedance tomography (EIT) system for breast cancer detection”. In: *Physiological measurement* **22** (2001), pp. 9–18.
- [Cia78] P. Ciarlet. *The Finite Element Method for Elliptic Problems*. Amsterdam: North-Holland Publishing Company, 1978.
- [CK98] D. Colton and R. Kress. *Inverse acoustic and electromagnetic scattering theory*. Berlin: Springer-Verlag, 1998.
- [Cra17] M. Crabb. “Convergence study of 2D forward problem of electrical impedance tomography with high order finite elements”. In: *Inverse Problems in Science and Engineering* **25.10** (2017), pp. 1397–1422.

- [DHL19] M. Darbas, J. Heleine, and S. Lohrengel. “Sensitivity analysis for 3D Maxwell’s equations and its use in the resolution of an inverse medium problem at fixed frequency”. In: *Inverse Problems in Science and Engineering* (2019), pp. 1–38.
- [DHMV] M. Darbas, J. Heleine, R. Mendoza, and A. C. Velasco. “Sensitivity analysis of the Complete Electrode Model for electrical impedance tomography”. in preparation.
- [DL18] M. Darbas and S. Lohrengel. “Review on Mathematical Modelling of Electroencephalography (EEG)”. In: *Jahresbericht der Deutschen Mathematiker-Vereinigung* **121.1** (2018), pp. 3–39.
- [DS16] J. Dardé and S. Staboulis. “Electrode modelling: The effect of contact impedance”. In: *ESAIM: M2AN* **50.2** (2016), pp. 415–431.
- [DMS16] S. Das, S. S. Mullick, and P. N. Suganthan. “Recent advances in differential evolution – An updated survey”. In: *Swarm and Evolutionary Computation* **27** (2016), pp. 1–30.
- [DS10] S. Das and P.N. Suganthan. *Problem definitions and evaluation criteria for CEC 2011 competition on testing evolutionary algorithms on real world optimization problems*. Tech. rep. Singapore: Jadavpur University, India and Nanyang Technological University, 2010.
- [Dem11] E. Demidenko. “An analytic solution to the homogeneous EIT problem on the 2D disk and its application to estimation of electrode contact impedances”. In: *Physiological measurement* **32** (2011), pp. 1453–71.
- [DE12] D. Di Pietro and A. Ern. *Mathematical Aspects of Discontinuous Galerkin Methods*. Berlin: Springer, 2012.
- [Dia17] M. M. Diallo. “Problème inverse de sources en Electro-Encéphalo-Graphie chez le nouveau-né”. PhD thesis. Amiens, France: Université de Picardie Jules Verne, 2017.
- [DS94] D. C. Dobson and F. Santosa. “An image enhancement technique for electrical impedance tomography.” In: *Inverse Problems* **10** (1994), pp. 317–334.
- [Dol98] R. Doll. “Effects of small doses of ionising radiation”. In: *Journal of Radiological Protection* **18** (1998), pp. 163–174.
- [DIS89] F. H. Duffy, V. G. Iyer, and W. W. Surwillo. *Clinical electroencephalography and topographic brain mapping: Technology and practice*. Springer-Verlag Publishing, 1989.

- [ESE11] S. M. Elsayed, R. A. Sarker, and D. L. Essam. “GA with a new multi-parent crossover for solving IEEE-CEC2011 competition problems”. In: *2011 IEEE Congress of Evolutionary Computation (CEC)*. IEEE. 2011, pp. 1034–1040.
- [FRBSS14a] A. R. Feitosa, R. R. Ribeiro, V. A. Barbosa, R. E. de Souza, and W. P. dos Santos. “Reconstruction of electrical impedance tomography images using chaotic ring-topology particle swarm optimization and non-blind search”. In: *Proceedings of the 2014 IEEE International Conference on Systems, Man, and Cybernetics (SMC)*. 2014, pp. 2618–2623.
- [FRBSS14b] A. R. Feitosa, R. R. Ribeiro, V. A. Barbosa, R. E. de Souza, and W. P. dos Santos. “Reconstruction of electrical impedance tomography images using particle swarm optimization, genetic algorithms and non-blind search”. In: *Proceedings of the 5th ISSNIP-IEEE Biosignals and Biorobotics Conference (2014): Biosignals and Robotics for Better and Safer Living (BRC)*. 2014, pp. 1–6.
- [FvM11] M. Fernández-Corazza, N. von-Ellenrieder, and C. H. Muravchik. “Estimation of electrical conductivity of a layered spherical head model using electrical impedance tomography”. In: *Journal of Physics: Conference Series* **332** (2011), pp. 12–22.
- [FFYB13] I. Fister, I. Fister Jr., X.-S. Yang, and J. Brest. “A comprehensive review of firefly algorithms”. In: *Swarm and Evolutionary Computation* **13** (2013), pp. 34–46.
- [FHHWHDQH02] I. Frerichs, J. Hinz, P. Herrmann, G. Weisser, G. Hahn, T. Dudykevych, M. Quintel, and G. Hellige. “Detection of local lung air content by electrical impedance tomography compared with electron beam CT”. In: *Journal of applied physiology (1985)* **93** (2002), pp. 660–666.
- [HHP08] R. J. Halter, A. Hartov, and K. D. Paulsen. “A Broadband High-Frequency Electrical Impedance Tomography System for Breast Imaging”. In: *IEEE Transactions on Biomedical Engineering* **55.2** (2008), pp. 650–659.
- [Han06] N. Hansen. “The CMA evolution strategy: a comparing review”. In: *Towards a New Evolutionary Computation: Advances in the Estimation of Distribution Algorithms*. Springer Berlin Heidelberg, 2006, pp. 75–102.
- [HSBB87] N. D. Harris, A. J. Suggett, D. C. Barber, and B. H. Brown. “Applications of applied potential tomography (APT) in respiratory medicine”. In: *Clinical Physics and Physiological Measurement* **8.4A** (1987), pp. 155–165.

- [Hec12] F. Hecht. “New development in FreeFem++”. In: *Journal of Numerical Mathematics* **20.3-4** (2012), pp. 251–265. URL: <https://freefem.org/>.
- [HG78] R. P. Henderson and Webster J. G. “An impedance camera for spatially specific measurements of the thorax.” In: *IEEE Transactions on Biomedical Engineering* **25.3** (1978), pp. 250–254.
- [HVMAL07] C. N. Herrera, M. F. Vallejo, F. de Moura, J. C. Aya, and R. Lima. “Electrical Impedance Tomography Algorithm Using Simulated Annealing as a Search Method”. In: Proceedings of COBEM 2007: 19th International Congress of Mechanical Engineering. Brazil: ABCM, 2007.
- [HL08] M. Hintermüller and A. Laurain. “Electrical impedance tomography: from topology to shape”. In: *Control and Cybernetics* **37.4** (2008), pp. 913–933.
- [Hol92] D. Holder. “Electrical impedance tomography (EIT) of brain function”. In: *Brain topography* **5** (1992), pp. 87–93.
- [Hol93] D. Holder. *Clinical and physiological applications of electrical impedance tomography*. UCL Press, 1993.
- [Hol00] D. Holder. *Electrical Impedance Tomography: Methods, History and Applications*. London: IOP Publishing, 2000.
- [Hol75] J. Holland. *Adaptation in Natural and Artificial Systems*. Ann Arbor: University of Michigan Press, 1975.
- [HWWT91] P. Hua, E. J. Woo, J. G. Webster, and W. J. Tompkins. “Iterative reconstruction methods using regularization and optimal current patterns in electrical impedance tomography.” In: *IEEE Transactions on Biomedical Engineering* **10** (1991), pp. 621–628.
- [HMCS19] K. Hussain, M. N. Mohd Salleh, S. Cheng, and Y. Shi. “Metaheuristic research: a comprehensive survey”. In: *Artificial Intelligence Review* **52** (2019), pp. 2191–2233.
- [Hyv04] N. Hyvönen. “Complete Electrode Model of Electrical Impedance Tomography: Approximation Properties and Characterization of Inclusions”. In: *SIAM Journal on Applied Mathematics* **64.3** (2004), pp. 902–931.
- [HM17] N. Hyvönen and L. Mustonen. “Smoothed Complete Electrode Model”. In: *SIAM Journal on Applied Mathematics* **77.6** (2017), pp. 2250–2271.
- [HPS12] N. Hyvönen, P. Piiroinen, and O. Seiskari. “Point measurements for a Neumann-to-Dirichlet map and the Calderón problem in the plane”. In: *SIAM Journal on Mathematical Analysis* **44** (2012), pp. 3526–3536.

- [IUY10] O. Y. Imanuvilov, G. Uhlmann, and M. Yamamoto. “The Calderón problem with partial data in two dimensions”. In: *Journal of the American Mathematical Society* **23.3** (2010), pp. 655–691.
- [JAMHB15] M. Jehl, J. Avery, E. Malone, D. Holder, and T. Betcke. “Correcting electrode modelling errors in EIT on realistic 3D head models.” In: *Physiological Measurement* **36.12** (2015), pp. 2423–2442.
- [Jos98] J. Jossinet. “The impedivity of freshly excised human breast tissue”. In: *Physiological Measurement* **19.1** (1998), pp. 61–75.
- [KKS00] J. P. Kaipio, V. Kolehmainen, E. Somersalo, and M. Vauhkonen. “Statistical inversion and Monte Carlo sampling methods in electrical impedance tomography”. In: *Inverse Problems* **16.5** (2000), pp. 1487–1522.
- [KSV96] P. G. Kaup, F. Santosa, and M. Vogelius. “Method for imaging corrosion damage in thin plates from electrostatic data”. In: *Inverse Problems* **12.3** (1996), pp. 279–293.
- [KHM06] P. Kauppinen, J. Hyttinen, and J. Malmivuo. “Sensitivity distribution visualizations of impedance tomography measurement strategies”. In: *International Journal of Bioelectromagnetism* **8** (2006), pp. VII/1–VII/9.
- [KSU07] C. Kenig, J. Sjostraa, and G. Uhlmann. “The Calderón problem with partial data”. In: *Annals of Mathematics* **165** (2007), pp. 567–591.
- [KBK06] H.-C. Kim, C.-J. Boo, and M.-J. Kang. “Image Reconstruction Using Genetic Algorithm in Electrical Impedance Tomography”. In: *Neural Information Processing*. **4234**. Springer, 2006.
- [KBL05] H.-C. Kim, C.-J. Boo, and Y.-J. Lee. “Image Reconstruction Using Simulated Annealing Algorithm in EIT”. In: *International Journal of Control, Automation, and Systems* **3** (2005), pp. 211–216.
- [KMKKL02] H.-C. Kim, D.-C. Moon, M.-C. Kim, S. Kim, and Y.-S. Lee. “Improvement in EIT image reconstruction using genetic algorithm”. In: *Proceedings of the American Control Conference*. **5**. 2002, pp. 3858–3863.
- [KV84] R. Kohn and M. Vogelius. “Determining conductivity by boundary measurements”. In: *Communications on Pure and Applied Mathematics* **37** (1984), pp. 113–123.
- [KMS15] A. Kumar, R. K. Misra, and D. Singh. “Butterfly optimizer”. In: *2015 IEEE Workshop on Computational Intelligence: Theories, Applications and Future Directions (WCI)*. 2015, pp. 1–6.

- [KMS17] A. Kumar, R. K. Misra, and D. Singh. “Improving the local search capability of Effective Butterfly Optimizer using Covariance Matrix Adapted Retreat Phase”. In: *2017 IEEE Congress on Evolutionary Computation (CEC)*. 2017, pp. 1835–1842.
- [LR06] A. Lechleiter and A. Rieder. “Newton regularizations for impedance tomography: a numerical study.” In: *Inverse Problems* **22.6** (2006), pp. 1967–1987.
- [LYMJH18] X. Li, F. Yang, J. Ming, A. Jadoon, and S. Han. “Imaging the Corrosion in Grounding Grid Branch with Inner-Source Electrical Impedance Tomography”. In: *Energies* **11** (2018), p. 1739.
- [LRHXWGY03] Y. Li, L. Rao, R. He, G. Xu, Q. Wu, M. Ge, and Weili Yan. “Image Reconstruction of EIT Using Differential Evolution Algorithm”. In: *Proceedings of the 25th Annual International Conference of the IEEE EMBS*. 2003, pp. 1011–1014.
- [Luk13] S. Luke. *Essentials of Metaheuristics*. Second. Available for free at <http://cs.gmu.edu/~sean/book/metaheuristics/>. Lulu, 2013.
- [Mar05] D. Maringer. *Portfolio management with heuristic optimization*. Springer, 2005.
- [MCLAT12] T. C. Martins, E. D. L. B. de Camargo, R. G. Lima, M. B. P. Amato, and M. S. G. Tsuzuki. “Image Reconstruction Using Interval Simulated Annealing in Electrical Impedance Tomography”. In: *IEEE Transactions on Biomedical Engineering* **59.7** (2012), pp. 1861–1870.
- [McC05] J. McCall. “Genetic algorithms for modelling and optimisation”. In: *Journal of Computational and Applied Mathematics* **184** (2005), pp. 205–222.
- [ML12] R. Mendoza and J. E. Lope. “Reconstructing Images in Electrical Impedance Tomography using Hybrid Genetic Algorithms”. In: *Science Diliman* **24.2** (2012), pp. 50–66.
- [MGLZ15] X.-B. Meng, X.Z. Gao, Y. Liu, and H. Zhang. “A novel bat algorithm with habitat selection and Doppler effect in echoes for optimization”. In: *Expert Systems with Applications* **42** (2015), pp. 6350–6364.
- [MPH06] D. Miklavcic, N. Pavselj, and F. Hart. “Electric Properties of Tissues”. In: vol. 6. 2006.
- [MHFJ17] A. W. Mohamed, A. A. Hadi, A. M. Fattouh, and K. M. Jambi. “LSHADE with semi-parameter adaptation hybrid with CMA-ES for solving CEC 2017 benchmark problems”. In: *2017 IEEE Congress on Evolutionary Computation (CEC)*. IEEE. 2017, pp. 145–152.

- [MLH18] D. Molina, A. LaTorre, and F. Herrera. “An Insight into Bio-inspired and Evolutionary Algorithms for Global Optimization: Review, Analysis, and Lessons Learnt over a Decade of Competitions”. In: *Cognitive Computation* **10** (2018), pp. 517–544.
- [Mor11] J. Morio. “Global and local sensitivity analysis methods for a physical system”. In: *European Journal of Physics* **32** (2011), pp. 1577–1583.
- [MSI02] J. L. Mueller, S. Siltanen, and D. Isaacson. “A direct reconstruction algorithm for electrical impedance tomography.” In: *IEEE transactions on medical imaging* **21** (2002), pp. 555–559.
- [MY85] T. Murai and Kagawam Y. “Electrical impedance computed tomography based on a finite element model.” In: *IEEE Transactions on Biomedical Engineering* **32** (1985), pp. 177–184.
- [MM17] M. Mutingi and C. Mbohwa. *Grouping Genetic Algorithms: Advances and Applications*. Switzerland: Springer, 2017.
- [NIM02] J. Newell, D. Isaacson, and J. Mueller. “Electrical Impedance Tomography”. In: *IEEE Trans. Med. Imaging* **21** (2002), pp. 553–554.
- [OBP00] R. Olmi, M. Bini, and S. Priori. “A genetic algorithm approach to image reconstruction in electrical impedance tomography”. In: *IEEE Transactions on Evolutionary Computation* **4** (2000), pp. 83–88.
- [Pap17] C. Papageorgakis. “Modèles de conductivité patient-spécifiques: caractérisation de l’os du crâne.” PhD thesis. Nice, France: INRIA Sophia, Université Côte d’Azur, 2017.
- [Par84] R. Parker. “The inverse problem of resistivity sounding”. In: *Geophysics* **142** (1984), pp. 2143–2158.
- [PSL05] K. Price, R. Storn, and J. Lampinen. *Differential Evolution: A Practical Approach to Global Optimization*. Berlin: Springer, 2005.
- [PLW16] S. Pursiainen, S. Lew, and C. Wolters. “Forward and Inverse Effects of the Complete Electrode Model in Neonatal EEG”. In: *Journal of Neurophysiology* **117** (2016), pp. 876–884.
- [PLW12] S. Pursiainen, F. Lucka, and C. Wolters. “Complete electrode model in EEG: relationship and differences to the point electrode model [published correction appears in Phys Med Biol. 2013 Jan 7;58(1):185]”. In: *Phys Med Biol.* **57.4** (2012), pp. 999–1017.

- [RD96] A. Ramirez and W. Daily. “Detection of leaks in underground storage tanks using electrical resistance methods: 1996 results (UCRL-ID-125918)”. In: (Oct. 1996).
- [RDLOC93] A. Ramirez, W. Daily, D. LaBrecque, E. Owen, and D. Chesnut. “Monitoring an Underground Steam Injection Process Using Electrical Resistance Tomography”. In: *Water Resources Research* **29.1** (1993), pp. 73–87.
- [RKKLKK10] A. Rashid, A. K. Khambampati, B. S. Kim, D. Liu, S. Kim, and K. Y. Kim. “A Differential Evolution Based Approach to Estimate the Shape and Size of Complex Shaped Anomalies Using EIT Measurements”. In: *Grid and Distributed Computing, Control and Automation*. **121**. Berlin: Springer, 2010.
- [Rey97] J. Reynolds. *An introduction to applied and environmental geophysics*. 1997.
- [RFSD14] R. Ribeiro, A. Feitosa, R. Souza, and W. Dos Santos. “Reconstruction of electrical impedance tomography images using genetic algorithms and non-blind search”. In: *ISSNIP Biosignals and Biorobotics Conference, BRC*. 2014, pp. 153–156.
- [RPP10] D. Romano, S. Pisa, and E. Piuze. “Implementation of the Newton-Raphson and admittance methods for EIT.” In: *International Journal of Bioelectromagnetism* **12.1** (2010), pp. 12–20.
- [SV91] F. Santosa and M. Vogelius. “A computational algorithm to determine cracks from electrostatic boundary measurements”. In: *International Journal of Engineering Science* **29.8** (1991), pp. 917–937.
- [Sia16] P. Siarry. *Metaheuristics*. Springer International Publishing, 2016.
- [SCI92] E. Somersalo, M. Cheney, and D. Isaacson. “Existence and uniqueness for electrode models for electric current computed tomography”. In: *SIAM Journal on Applied Mathematics* **52.4** (1992), pp. 1023–1040.
- [TF13] R. Tanabe and A. Fukunaga. “Success-history based parameter adaptation for differential evolution”. In: *2013 IEEE Congress on Evolutionary Computation*. IEEE. 2013, pp. 71–78.
- [TF14] R. Tanabe and A. Fukunaga. “Improving the search performance of SHADE using linear population size reduction”. In: *2014 IEEE Congress on Evolutionary Computation (CEC)*. IEEE. 2014, pp. 1658–1665.

- [TMT12] R. S. Tavares, T. C. Martins, and M. S. G. Tsuzuki. “Electrical Impedance Tomography Reconstruction Through Simulated Annealing using a New Outside-in Heuristic and GPU Parallelization”. In: *Journal of Physics: Conference Series*. **407**. 2012, pp. 1–15.
- [TIL15] E. Teschner, M. Imhoff, and S. Leonhardt. *Electrical Impedance Tomography: The realisation of regional ventilation monitoring, 2nd edition*. Dräger Medical GmbH, 2015.
- [TLPSX11] N. Tian, C. Lai, K. Pericleous, J. Sun, and W. Xu. “Contraction-Expansion Coefficient Learning in Quantum-Behaved Particle Swarm Optimization”. In: *2011 10th International Symposium on Distributed Computing and Applications to Business, Engineering and Science*. IEEE. 2011, pp. 303–308.
- [TWFRA19] D. Tingay, A. Waldmann, I. Frerichs, S. Ranganathan, and A. Adler. “Electrical Impedance Tomography Can Identify Ventilation and Perfusion Defects: A Neonatal Case”. In: *American Journal of Respiratory and Critical Care Medicine* **199** (2019), pp. 384–386.
- [Uhl09] G. Uhlmann. “Electrical impedance tomography and Calderón’s problem”. In: *Inverse Problems* **25** (2009), p. 123011.
- [VVSX99] P. J. Vauhkonen, M. Vauhkonen, T. Savolainen, and J. P. Kaipio. “Three-dimensional electrical impedance tomography based on the complete electrode model”. In: *IEEE Transactions on Biomedical Engineering* **46.9** (1999), pp. 1150–1160.
- [VDMBL20] A. C. Velasco, M. Darbas, R. Mendoza, M. Bacon, and J. C. de Leon. “Comparative Study of Heuristic Algorithms for Electrical Impedance Tomography”. In: *Philippine Journal of Science* **149.3-a** (2020).
- [VN17] C. Venkatratnam and F. Nagi. “Spatial resolution in electrical impedance tomography: A topical review”. In: *Journal of Electrical Bioimpedance* **8** (2017), pp. 66–78.
- [WC13] F.-S. Wang and L.-H. Chen. “Heuristic Optimization”. In: *Encyclopedia of Systems Biology*. New York, NY: Springer New York, 2013.
- [WC99] M. Wang and J. J. Cilliers. “Detecting non-uniform foam density using electrical resistance tomography”. In: *Chemical Engineering Science* **54.5** (1999), pp. 707–712.
- [Wir04] A. Wirgin. “The inverse Crime”. In: *Math Phys* (2004).
- [Yan14] C.L. Yang. “Electrical impedance tomography: algorithms and applications”. PhD thesis. Bath, United Kingdom: University of Bath, 2014.
- [Yan08] X.-S. Yang. *Nature-Inspired Metaheuristic Algorithms*. Luniver Press, 2008.

- [Yan10] X.-S. Yang. “A New Metaheuristic Bat-Inspired Algorithm”. In: *Nature Inspired Cooperative Strategies for Optimization (NISCO 2010)*. Vol. 284. Springer, 2010, pp. 65–74.
- [YH13a] X.-S. Yang and X. He. “Bat algorithm: literature review and applications”. In: *International Journal of Bio-Inspired Computation* **5.3** (2013).
- [YH13b] X.-S. Yang and X. He. “Firefly Algorithm: Recent Advances and Applications”. In: *International Journal of Swarm Intelligence* **1.1** (2013), pp. 36–50.
- [YWT87] T. J. Yorkey, J. G. Webster, and W. J. Tompkins. “Comparing Reconstruction Algorithms for Electrical Impedance Tomography”. In: *IEEE Transactions on Biomedical Engineering* **BME-34.11** (1987), pp. 843–852.
- [ZS09] J. Zhang and A. C. Sanderson. “JADE: Adaptive Differential Evolution With Optional External Archive”. In: *IEEE Transactions on Evolutionary Computation* **13.5** (2009), pp. 945–958.
- [ZFHZWW09] T. Zhu, R. Feng, J.-Q. Hao, J.-G. Zhou, H.-L. Wang, and S.-Q. Wang. “The Application of Electrical Resistivity Tomography to Detecting a Buried Fault: A Case Study”. In: *Journal of Environmental and Engineering Geophysics* **14** (2009), pp. 145–151.



# Méthodes numériques pour la résolution des problèmes direct et inverse en tomographie par impédance électrique

**Résumé.** Dans cette thèse, nous étudions la tomographie par impédance électrique (EIT) du point de vue théorique et numérique. Mathématiquement, cela consiste à résoudre un problème direct et un problème inverse. Le problème direct permet de calculer les valeurs du potentiel électrique aux électrodes. Ces valeurs représentent les données pour le problème inverse : la reconstruction de la distribution de conductivité dans le domaine. Le modèle d'électrode complet (CEM) modélise avec précision les phénomènes d'interface électrode/tissu. Nous étudions en détail ce modèle et sa résolution numérique par éléments finis. De plus, afin de comprendre l'influence de la conductivité et de l'impédance de contact des électrodes sur le potentiel électrique, nous menons une analyse de sensibilité rigoureuse du problème direct. Le problème inverse est, quant à lui, formulé comme un problème de minimisation d'une fonctionnelle-coût représentant la différence entre les tensions mesurées et prédites aux électrodes. L'applicabilité de différents algorithmes métaheuristiques en tant que stratégie d'optimisation pour le problème de reconstruction est proposée. Des simulations numériques sont effectuées pour comparer leur efficacité. Enfin, nous nous intéressons à la modélisation des électrodes pour l'électroencéphalographie (EEG). Pour traiter la singularité du terme source, l'approche de soustraction est proposée. Nous démontrons un résultat d'existence et d'unicité.

**Mots-clés :** tomographie par impédance électrique, modèle d'électrode complète, problème inverse, algorithmes heuristiques, analyse de sensibilité, électroencéphalographie

## Numerical methods for the resolution of the forward and the inverse problems for Electrical Impedance Tomography

**Abstract.** In this thesis, we study from a theoretical and a numerical point of view the Electrical Impedance Tomography (EIT). Mathematically, it consists of solving two problems: a forward one and an inverse one. The forward problem gives the boundary voltages at the electrodes which are the data needed for the inverse problem - the reconstruction of the conductivity distribution in the domain. The Complete Electrode Model (CEM) accurately models the electrodes and their shunting effects in real-life applications. We focus our research on the CEM forward model for EIT and we study its analytical and numerical solution for different configurations. Furthermore, in order to understand the influence of both the conductivity and the contact impedance of the electrodes on the electric potential, we propose a rigorous sensitivity analysis of the CEM forward problem. Next, the inverse problem is formulated as the minimization of a cost function representing the difference between the measured and predicted voltages. The applicability of metaheuristic algorithms as optimization strategies for the reconstruction problem is addressed. Numerical simulations are done to compare their efficiency. Finally, we are interested in modeling the electrodes for Electroencephalography (EEG) using CEM. In order to deal with the singularity in the source term, the subtraction approach is applied. The existence and uniqueness of the solution for the CEM forward problem of EEG is proven.

**Keywords:** electrical impedance tomography, complete electrode model, inverse problem, heuristic algorithms, sensitivity analysis, electroencephalography